



UNIVERSITY OF ROME "ROMA TRE"

Department of Mathematics and Physics

Measurement of $\gamma\gamma \rightarrow \pi^0\pi^0$ production
in the region of the $\sigma(500)$ meson
with the KLOE detector

Candidate:
Ivan Prado Longhi

Supervisors:
Prof. Filippo Ceradini
Dr. Antonio Passeri
Dr. Federico Nguyen

January 2014

Contents

1	Scalar mesons	7
1.1	Scalar mesons in the quark model	9
1.1.1	$q\bar{q}$ and qqq states	11
1.1.2	Scalar mesons as $qq\bar{q}\bar{q}$ states	12
2	$\gamma\gamma$ interactions at e^+e^- colliders	15
2.1	Kinematics	16
2.1.1	$\gamma\gamma$ luminosity function	18
2.1.2	Cross section for resonance production	19
2.2	Experimental aspects	21
2.2.1	Experiments	22
2.2.2	KLOE contribution	23
3	The KLOE experiment at DAΦNE	25
3.1	DAΦNE	25
3.2	KLOE Detector	28
3.2.1	The Drift Chamber	31
3.2.2	The Electromagnetic Calorimeter	32
3.3	Reconstruction Algorithms	34
3.3.1	Cluster Reconstruction	34
4	Data acquisition	36
4.1	The Trigger system	36
4.2	Background Rejection Filter	37
4.3	$\gamma\gamma$ filter	39
5	The process $e^+e^- \rightarrow e^+e^-\pi^0\pi^0$ and backgrounds	40
5.1	$e^+e^- \rightarrow e^+e^-\sigma \rightarrow e^+e^-\pi^0\pi^0$	40
5.1.1	Angular distribution of the final state e^\pm	41

5.2	$e^+e^- \rightarrow K_S K_L$	46
5.2.1	MC Energy Calibration	46
5.2.2	Cross Section at $\sqrt{s} = 1$ GeV	50
5.2.3	Studies on late clusters	53
5.3	$e^+e^- \rightarrow \eta\gamma$	57
5.3.1	Dedicated analysis for $e^+e^- \rightarrow \eta\gamma$	57
5.4	$e^+e^- \rightarrow \omega\pi^0, \omega \rightarrow \pi^0\gamma$	59
5.5	Minor processes	61
5.5.1	$e^+e^- \rightarrow \phi \rightarrow f_0\gamma, f_{a_0}\gamma$	61
5.5.2	$e^+e^- \rightarrow \gamma\gamma$	61
6	Analysis	62
6.1	Cluster counting and recover splitting	62
6.1.1	Cluster counting	63
6.2	Preselections	64
6.3	Two π^0 signature, $m_{4\gamma}$ reconstruction	67
6.3.1	Resolution function	67
6.4	Cut-based analysis	78
6.4.1	Track veto	78
6.4.2	Cut on $\chi_{\pi\pi}^2$	80
6.4.3	4 γ only	82
6.4.4	Rejection of events with late clusters	82
6.4.5	Cut on photons energy spread	83
6.4.6	Cuts efficiency on signal as function of $m_{4\gamma}$	85
6.4.7	Summary of cut-based analysis	87
6.5	Multivariate Analysis	92
6.5.1	Identification of the machine background	93
6.5.2	Training	98
6.5.3	Application	104
6.5.4	Cut on the MVA response	106
6.5.5	Selection for background	111
7	Extraction of $\gamma\gamma \rightarrow \pi^0\pi^0$ cross section	113
7.1	Selections efficiency on signal	114
7.2	Systematic errors	117
7.2.1	Cut on TMVA Likelihood Response	118
7.2.2	$m_{4\gamma}$ reconstruction, cut on $\chi_{\pi\pi}^2$	121
7.2.3	Cut on E_{RMS}	124

7.2.4	Summary on systematics	126
7.3	$\gamma\gamma \rightarrow \pi^0\pi^0$ cross section	128
Bibliography		131

A Burlone, uno di loro

Introduction

From both a theoretical and an experimental point of view, the process $\gamma\gamma \rightarrow \pi\pi$ represents an interesting and challenging topic. Interesting theoretical aspects resides for example in the dynamic of the process, in which low-energy QCD plays a determinant role, thus representing a good example to test effective theories such as chiral lagrangians, linear (or non-linear) sigma models, and others. Furthermore, the reaction can take place via the production of a resonant scalar meson as an intermediate state: this possibility makes the study of this process particularly intriguing, as a picture of scalar mesons sector is still far to be complete. In particular, exploring the near threshold energies one could expect contribution of the lightest scalar meson, the $\sigma(500)$, sometimes referred to as $f_0(500)$, which is one of the most debated particle in hadronic spectroscopy and for which striking experimental evidences are not available yet. Investigating scalars by $\gamma\gamma$ interactions is in any case very interesting, as extracting the coupling of the meson to photons could provide precious information about internal structure of these objects, which is still an open question even for those states whose existence is not debated.

Experimentally, realizing photon-photon scattering is quite hard with real photons, even if efforts are being made in this direction (see, for example, [1]); the Higgs discovery has also encouraged study on the feasibility for a “ $\gamma\gamma$ Higgs factory” [2]. Nevertheless $\gamma\gamma$ interactions have been studied since early 1970’s at e^+e^- colliders using *virtual photons* radiated by electron and positron beams and went on up to our days. The observed process is $e^+e^- \rightarrow e^+e^-\gamma^*\gamma^* \rightarrow e^+e^-X$, where electron and positron in the final state are typically scattered by small angles and the virtual photons are nearly real. Measurement of the $\gamma^*\gamma^* \rightarrow X$ process in this experimental situation is made difficult by kinematics and dynamics, and requires detectors with high efficiency performances in the forward direction. Moreover, on a theoretical ground, connection between the $\gamma^*\gamma^* \rightarrow X$ subprocess and the overall process involves the emission of radiation by both the electron and the positron, which is typically described by a “ $\gamma\gamma$ flux” function whose parameterization has been object of discussion for a long time.

In this thesis an analysis searching a signal for the process $e^+e^- \rightarrow e^+e^-\pi^0\pi^0$ is presented; this analysis has been performed on data collected by the KLOE detector at the DAΦNE ϕ -factory near Rome. The analyzed data sample has been collected at $\sqrt{s} = 1$ GeV, where backgrounds due to radiative ϕ decays are strongly suppressed; as the radiative return to the ρ mass, with $\rho \rightarrow \pi^+\pi^-$, is an abundant process at these energies, the $\pi^0\pi^0$ final state has been chosen instead of $\pi^+\pi^-$. A preliminary analysis on KLOE data had shown a clear excess of events, with respect to annihilation processes, in the low $\pi^0\pi^0$ invariant mass spectrum, just above production threshold. The goal of the present analysis is to provide a spectrum as clean as possible from which one could extract the $\gamma\gamma \rightarrow \pi^0\pi^0$ cross section in this low invariant mass region, where the contribution from $\sigma(500)$ resonant production is expected.

Chapters 1 and 2 are devoted to the theoretical framework of the scalar mesons sector and of the $\gamma\gamma$ interactions. In Chapters 3 and 4 the experimental apparatus and the data acquisition conditions are described. Chapter 5 focuses on the signal and background processes involved in the analysis, providing description of both physical aspects and employed Monte Carlo simulations. In Chapter 6 the analysis strategy is described, clearly divided into two steps: a cut-based and a multivariate approaches have been used. Finally, in Chapter 7 the spectrum obtained by applying the analysis and subtracting the residual background is studied, systematic uncertainties are discussed and a first attempt to extract the $\gamma\gamma \rightarrow \pi^0\pi^0$ cross section is done.

Chapter 1

Scalar mesons

Scalar mesons sector is an obscure and intriguing chapter in hadron spectroscopy. Experimentally, scalar resonances investigation is difficult because some of these resonances have large decay widths which cause a strong overlap with background processes. Moreover, several decay channels often open up within a short mass interval (e.g. at the $K\bar{K}$ and $\eta\eta$ thresholds) making the resonance signal hard to identify. If on one side some scalar resonances, such as the $f_0(980)$, have been observed so clearly that their parameters (mass, total and partial widths) have been determined with quite good accuracy, in some cases the experimental situation is so puzzling that the existence itself of the particle has been or still is in doubt: this is the case of the $f_0(500)$, known in literature also as $\sigma(500)$.

From a theoretical point of view, many topics make the scalar mesons interesting and challenging. First of all, their internal structure is still an open question. In contrast to the pseudoscalar, vector and tensor mesons, for scalars one expects non- $q\bar{q}$ objects, such as glueballs and multiquark states in the mass range below 2 GeV. Moreover, advanced theory tools are needed in order to extract resonance parameters from data, as simple parameterizations fail: analyses can be found in literature which have employed fundamental properties of the amplitudes such as unitarity, analyticity, Lorentz invariance, chiral and flavor symmetry. Furthermore, as scalars have vacuum quantum numbers, they could play a role in spontaneous symmetry breaking mechanisms of some global symmetry, for example the chiral $SU_L(n_f) \times SU_R(n_f)$ symmetry. Implementation of such a mechanism is challenging, and among effective theories describing it the Linear Sigma Model (LSM) introduces a scalar field which breaks the symmetry by getting a non zero vacuum expectation value.

Scalar mesons are produced, for example, in πN scattering on polarized/unpolarized targets, $p\bar{p}$ annihilation, central hadronic production, J/Ψ , B^- , D^- and

K -meson decays, ϕ radiative decays and $\gamma\gamma$ interaction.

Scalars have been observed for the first time in the late 1960's. Studying $\pi^-p \rightarrow \pi^-\pi^+n$ process a suppression of the elastic scattering amplitude as a function of the two π invariant mass was observed near the $K\bar{K}$ threshold, while in the same region the anelastic process to $K\bar{K}$ final state showed a marked peak [3]. This feature was interpreted as the superposition of two resonances: one large ($\Gamma \approx 300$ MeV), identified with the scalar meson $\kappa(700)$, and one narrow ($\Gamma \approx 50$ MeV), named $f_0(980)$, strongly coupled with the $K\bar{K}$ channel. More recent evidences for the $\kappa(700)$ have been obtained in hadronic decays of the D meson near to the $K\pi$ threshold (E791, FOCUS, CLEO, BaBar experiments); BES II also found a structure which can be recognized as the κ in the $J/\Psi \rightarrow \bar{K}^{*0}(892)K^+\pi^-$ decay, with κ recoiling against the $K^*(892)$.

The $a_0(980)$ was first observed in the reaction $K^-p \rightarrow \Sigma^+(1385)\pi^-\eta, \Sigma^+K^-K^0$; cross section as a function of the $\pi\eta$ system invariant mass shows a resonant behavior $\pi\eta$ below the $K\bar{K}$ threshold, suggesting a strong coupling to this channel for the $a_0(980)$, too.

In two experiments the production of the $\sigma(500)$ scalar meson has been observed through Dalitz plot analysis: E791 [4] ($\pi^+\pi^-$ Dalitz plot in $D^+ \rightarrow \pi^+\sigma \rightarrow \pi^+\pi^+\pi^-$), BES [5] ($\omega\pi^-$ vs. $\omega\pi^+$ Dalitz plot in $J/\Psi \rightarrow \omega\pi^+\pi^-$); CLEO experiment measured the invariant mass in the $D^0 \rightarrow K_S\sigma \rightarrow K_S\pi^+\pi^-$ decay [6].

1.1 Scalar mesons in the quark model

The model based on $SU_f(3)$ flavor symmetry will be considered here, as we are not interested in dealing with charmed and/or bottomed hadrons. In this model hadrons are organized in the $SU(3)$ irreducible representations, where $SU(3)$ is the group of unitary 3×3 matrices with $\det U = 1$; these matrices can be expressed as

$$U = e^{i\mathbf{H}} = e^{i\sum_k \alpha_k \lambda_k}, \quad (1.1)$$

where \mathbf{H} is a hermitian matrix. In Eq. (1.1) \mathbf{H} is expanded in the basis of hermitian 3×3 matrices with null tracks (in order to have $\det U = 1$); λ_k , matrices, $k = 1, \dots, 8$ which form this basis are the *generators* of the $SU(3)$ group, and are typically chosen of the form

$$\begin{aligned} \lambda_8 &= \frac{1}{\sqrt{3}} \begin{pmatrix} 1 & 0 & 0 \\ 0 & 1 & 0 \\ 0 & 0 & -2 \end{pmatrix}, \\ \lambda_3 &= \begin{pmatrix} 1 & 0 & 0 \\ 0 & -1 & 0 \\ 0 & 0 & 0 \end{pmatrix}, \\ \lambda_1 &= \begin{pmatrix} 0 & 1 & 0 \\ 1 & 0 & 0 \\ 0 & 0 & 0 \end{pmatrix}, & \lambda_2 &= \begin{pmatrix} 0 & -i & 0 \\ i & 0 & 0 \\ 0 & 0 & 0 \end{pmatrix} \\ \lambda_4 &= \begin{pmatrix} 0 & 0 & 1 \\ 0 & 0 & 0 \\ 1 & 0 & 0 \end{pmatrix}, & \lambda_5 &= \begin{pmatrix} 0 & 0 & -i \\ 0 & 0 & 0 \\ i & 0 & 0 \end{pmatrix} \\ \lambda_6 &= \begin{pmatrix} 0 & 0 & 0 \\ 0 & 0 & 1 \\ 0 & 1 & 0 \end{pmatrix}, & \lambda_7 &= \begin{pmatrix} 0 & 0 & 0 \\ 0 & 0 & -i \\ 0 & i & 0 \end{pmatrix}. \end{aligned} \quad (1.2)$$

The 8 matrices (1.2) are said *Gell-Mann matrices*. It can be shown by direct calculation that

$$[\lambda_k, \lambda_l] = 2if_{klm}\lambda_m, \quad (1.3)$$

where f_{klm} are the structure constants of the group, antisymmetric under indexes exchange. The non vanishing structure constants are

$$f_{123} = 1; \quad f_{147} = f_{165} = f_{246} = f_{257} = f_{345} = f_{376} = \frac{1}{2};$$

$$f_{458} = f_{678} = \frac{\sqrt{3}}{2}; \quad (1.4)$$

all other are obtained by indexes permutation. Commutation relations (1.3) completely define $SU(3)$ algebra, referred to as $su(3)$ in group theory notation. As they are diagonal, Gell-Mann matrices λ_3 and λ_8 commute. The maximum number of commuting generators define the *rank* of the group: for $SU(n)$ the rank is given by $n - 1$, equal to the number of parameters which are essential to specify the diagonal elements of a $n \times n$ hermitian matrix with null track. Simultaneously diagonalizable generators are important as in applications they are associated to the observables whose eigenvalues are useful to define the states of the physical system in exam. In the case of the 3-flavor quark model, λ_3 is the isospin third component (I_3) eigenvalues matrix (up to a $\frac{1}{2}$ factor); λ_8 is the hyper-charge (Y) eigenvalues matrix (up to a $\frac{1}{\sqrt{3}}$ factor).

The fundamental representation is the smallest non trivial representation; in $SU(3)$ is provided by 3×3 unitary matrices with $\det = 1$ themselves; notation for this representation is simply $\mathbf{3}$. These matrices acts on three basis vectors which are identified with the three quarks *up* (u), *down* (d) and *strange* (s)

$$u = \begin{pmatrix} 1 \\ 0 \\ 0 \end{pmatrix}, \quad d = \begin{pmatrix} 0 \\ 1 \\ 0 \end{pmatrix}, \quad s = \begin{pmatrix} 0 \\ 0 \\ 1 \end{pmatrix}, \quad (1.5)$$

which are spin $\frac{1}{2}$ fermions; they constitute the fundamental $SU(3)$ *triplet*. The conjugate matrices

$$U^* = e^{-i\mathbf{H}^T} = e^{i\sum_k \alpha_k (-\lambda_k^T)} \quad (1.6)$$

provide another dimension 3 group representation, named *conjugate representation* and noted by $\bar{\mathbf{3}}$. From (1.6) it is straightforward that in the conjugate representation diagonal generators are $-\lambda_3^T$ e $-\lambda_8^T$, with *opposite sign* eigenvalues with respect to those of λ_3 e λ_8 : basis vectors for $\bar{\mathbf{3}}$ are naturally identified with the antiquarks \bar{u} , \bar{d} e \bar{s} . Aligning notation with particle physics literature, operators \mathbf{I}_3 (third isospin

component) and \mathbf{Y} (hypercharge) are defined as

$$\mathbf{I}_3 = \frac{\lambda_3}{2}, \quad \mathbf{Y} = \frac{\lambda_8}{\sqrt{3}}; \quad (1.7)$$

let's define the **electric charge** operator \mathbf{Q} , too, related to isospin and to hypercharge through the Gell-Mann e Nishijima law:

$$\mathbf{Q} = \frac{\mathbf{Y}}{2} + \mathbf{I}_3. \quad (1.8)$$

Action of these operators on basis vector in the $\mathbf{3}$ and in the $\bar{\mathbf{3}}$ returns the quantum numbers for quark and antiquark, listed in Tab 1.1.

Quark	I_3	Y	Q	Antiquark	I_3	Y	Q
u	$\frac{1}{2}$	$\frac{1}{3}$	$\frac{2}{3}$	\bar{u}	$-\frac{1}{2}$	$-\frac{1}{3}$	$-\frac{2}{3}$
d	$-\frac{1}{2}$	$\frac{1}{3}$	$-\frac{1}{3}$	\bar{d}	$\frac{1}{2}$	$-\frac{1}{3}$	$\frac{1}{3}$
s	0	$-\frac{2}{3}$	$-\frac{1}{3}$	\bar{s}	0	$\frac{2}{3}$	$\frac{1}{3}$

Table 1.1: Quantum numbers of the 3 lightest quarks and antiquarks.

Performing the *external product* (noted by \otimes) of $\mathbf{3}$ and $\bar{\mathbf{3}}$ representations one can obtain higher dimensions representations, which are in general reducible; by reduction one obtains all irreducible representations of the group.

1.1.1 $q\bar{q}$ and qqq states

Assigning a *baryonic number* $B = \frac{1}{3}$ to quarks and $B = -\frac{1}{3}$ to antiquarks it is possible to build up states $q\bar{q}$ with $B = 0$ and integer spin (mesons), or states with three quarks with $B = 1$ and half-integer spin (baryons). As predicted by Dirac theory, quarks and antiquarks exhibit opposite parity; a $q\bar{q}$ pair in a angular momentum L state thus has parity P defined by

$$P = (-1)^{L+1}. \quad (1.9)$$

States with $L = 0$ describe pseudoscalars mesons $J^P = 0^-$ (if quark and antiquark spins are not in the same direction) or vector mesons $J^P = 1^-$ (if spins are in the same directions); states with $L = 1$ and $J = 2$ are tensor mesons 2^+ . States with $L = 1$ e $J = 0$ are possible, too, and could describe scalar mesons 0^+ ; light scalar mesons spectroscopy however induces to reject this hypotesis (see §1.1.2). $SU(3)$

irreducible representations one can obtain building the external product $\mathbf{3} \otimes \bar{\mathbf{3}}$ are the octet $\mathbf{8}$ and the singlet $\mathbf{1}$

$$\mathbf{3} \otimes \bar{\mathbf{3}} = \mathbf{8} \oplus \mathbf{1}; \quad (1.10)$$

pseudoscalars and vectors are organized in such multiplets.

For baryons one has to consider the irreducible representations obtained from the

$$\mathbf{3} \otimes \mathbf{3} \otimes \mathbf{3} = \mathbf{10} \oplus \mathbf{8} \oplus \mathbf{8} \oplus \mathbf{1}, \quad (1.11)$$

in which baryons $J^P = \frac{1}{2}^+$ (octet) e $J^P = \frac{3}{2}^+$ (decuplet) are located.

1.1.2 Scalar mesons as $qq\bar{q}\bar{q}$ states

Diquark-antidiquark states, named *tetraquark*, ($qq\bar{q}\bar{q}$), are possible candidate to describe the structure of light scalar mesons; tetraquark states in S wave reproduce in fact scalar quantum numbers.

Let's consider preliminary the single qq ($\bar{q}\bar{q}$) pair. Two identical fermions state, which one can factorize into a spin, flavor and color state, has to be globally anti-symmetric under particles exchange; if one asks the state to have spin zero, that is a antisymmetric spin singlet, the qq ($\bar{q}\bar{q}$) must be symmetric under $SU_f(3) \times SU_c(3)$ ¹

For both flavor (f=flavor) and color (c=color) the external product $\mathbf{3} \otimes \mathbf{3}$ of representations for the two quarks can be reduced as follows:

$$\mathbf{3}_{f,c} \otimes \mathbf{3}_{f,c} = \mathbf{6}_{f,c} \oplus \bar{\mathbf{3}}_{f,c}, \quad (1.12)$$

with $\mathbf{6}$ symmetric, $\bar{\mathbf{3}}$ antisymmetric. In the same way, for the antiquark pair:

$$\bar{\mathbf{3}}_{f,c} \otimes \bar{\mathbf{3}}_{f,c} = \bar{\mathbf{6}}_{f,c} \oplus \mathbf{3}_{f,c}, \quad (1.13)$$

($\bar{\mathbf{6}}$ symmetric, $\mathbf{3}$ antisymmetric). Writing as $(\mathbf{n}_f, \mathbf{n}_c)$ the diquark (antidiquark) states with respect to $SU_f(3) \times SU_c(3)$, one has that desired symmetric states are

$$qq = (\mathbf{6}_f, \mathbf{6}_c), \quad \bar{q}\bar{q} = (\bar{\mathbf{6}}_f, \bar{\mathbf{6}}_c), \quad (1.14)$$

or

$$qq = (\bar{\mathbf{3}}_f, \bar{\mathbf{3}}_c), \quad \bar{q}\bar{q} = (\mathbf{3}_f, \mathbf{3}_c). \quad (1.15)$$

Now we are left with the task of considering the external product $qq \otimes \bar{q}\bar{q}$, which gives

$$qq \otimes \bar{q}\bar{q} = (\bar{\mathbf{3}}_f \otimes \mathbf{3}_f, \bar{\mathbf{3}}_c \otimes \mathbf{3}_c) \quad (1.16)$$

¹Symbol \times means internal direct product (Kronecker product), which factorize internal symmetries of a physical state.

and

$$qq \otimes \bar{q}\bar{q} = (\mathbf{6}_f \otimes \bar{\mathbf{6}}_f, \mathbf{6}_c \otimes \bar{\mathbf{6}}_c); \quad (1.17)$$

considered products reduce as follows:

$$\mathbf{3} \otimes \bar{\mathbf{3}} = \mathbf{8} \oplus \mathbf{1}, \quad (1.18)$$

$$\mathbf{6} \otimes \bar{\mathbf{6}} = \mathbf{27} \oplus \mathbf{8} \oplus \mathbf{1}. \quad (1.19)$$

Physical states have to be color singlets; one therefore gets from (1.18) the multiplets

$$qq\bar{q}\bar{q} = (\mathbf{8}_f, \mathbf{1}_c), \quad (\mathbf{1}_f, \mathbf{1}_c) \quad (1.20)$$

and from (1.19)

$$qq\bar{q}\bar{q} = (\mathbf{27}_f, \mathbf{1}_c), \quad (\mathbf{8}_f, \mathbf{1}_c), \quad (\mathbf{1}_f, \mathbf{1}_c). \quad (1.21)$$

Mass spectra for scalar and pseudoscalar mesons are shown in Fig. 1.1; one can observe the inversion of the mass ordering in the two cases. Inversion of scalar meson

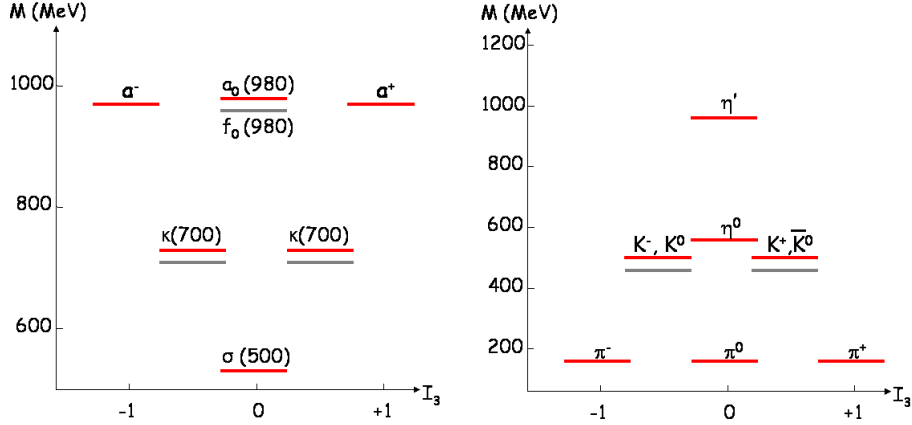


Figure 1.1: Mass spectra for scalar mesons (left) and pseudoscalar mesons (right).

mass ordering with respect to pseudoscalar mesons can be explained in the framework of tetraquark model: mass ordering is determined by strange quark content in the hadron, and this is maximum in a_0 e f_0 (2 s quarks), intermediate in κ (1 s quark) and minimum in σ (no s quark) (see Tab. 1.2)

Composition according to Tab. 1.2 also provides explanation for the strong coupling of the a_0 e f_0 mesons with the $K\bar{K}$ channel and of the σ with the $\pi\pi$ channel.

	I	I_3	S	Y	Composition
a_0^+	1	+1	0	0	$[su][\bar{s}d]$
a_0^0	1	0	0	0	$\frac{1}{\sqrt{2}}([su][\bar{s}u] - [sd][\bar{s}d])$
a_0^-	1	-1	0	0	$[sd][\bar{s}u]$
f_0	0	0	0	0	$\frac{1}{\sqrt{2}}([su][\bar{s}u] + [sd][\bar{s}d])$
σ	0	0	0	0	$[ud][\bar{u}d]$
κ^+	1/2	+1/2	+1	+1	$[ud][\bar{s}d]$
κ^0	1/2	-1/2	+1	+1	$[ud][\bar{s}u]$
$\bar{\kappa}^0$	1/2	+1/2	-1	-1	$[us][\bar{d}u]$
κ^-	1/2	-1/2	-1	-1	$[ds][\bar{d}u]$

Table 1.2: Scalar meson quantum numbers and their composition in the diquark-antidiquark model.

Chapter 2

$\gamma\gamma$ interactions at e^+e^- colliders

Light-light scattering seems at first glance forbidden in the framework of classical electrodynamics: the electromagnetic field A_μ is the only gauge field of an abelian $U(1)$ theory, and cannot therefore interact with itself; the only allowed interaction terms are those with the fermion current, $\bar{\psi}(x)\gamma^\mu\psi(x)A_\mu(x)$.

When quantizing the theory, photon can be seen either as the quantum of the electromagnetic field or as an elementary particle. In this scenario, a photon of energy E_γ can fluctuate into states of charged particles (fermion-antifermion pair with mass m_{pair}), the lifetime of the intermediate state being given by $\Delta t \simeq \hbar/m_{pair}$; photon-photon interactions become possible between these intermediate states. That means that photons, usually regarded as probes to investigate charged targets, can themselves be considered as targets as well.

Experimentally, it is quite hard to collide high energy photon beams. This problem can be avoided using virtual instead of real photons, that is photons radiated by charged particle beams in storage rings; here we will focus on $\gamma^*\gamma^*$ at e^+e^- colliders, where virtual photons are predominantly radiated at small angles, $\theta \simeq 1/\gamma$, $\gamma = \sqrt{1 - \beta_e^2}$, therefore being “quasi real”.

A typical $e^+e^- \rightarrow e^+e^-X$ process is sketched in Fig. 2.1; it is the fourth order in $\alpha = \frac{1}{137}$ and for this reason its cross section could seem to be very small. However, when $q_1^2, q_2^2 \rightarrow 0$ the amplitude for such a process is not suppressed by photon propagators; moreover, integration over virtual photons quadri-momenta gives a $\propto \ln^2 s$ term, where \sqrt{s} is the energy in the e^+e^- c.m.s., which enhances this amplitude for increasing energy, making it dominant with respect to annihilation processes which decrease as $1/s$. Photon-photon interactions produce states with spin-parity $J^{PC} = 0^{\pm+}$ and $2^{\pm+}$ and are therefore useful processes to study scalar and tensor mesons.

2.1 Kinematics

Consider a typical $e^+e^- \rightarrow e^+e^-X$ process where X is the state produced by the interaction of two virtual photons γ_1^* , γ_2^* radiated by the electron in the positron field and vice-versa. Let be E the beams energy (assuming a symmetric beams configuration) and q_1 , q_2 the photons quadri-momenta. The invariant mass for the state X is

$$w^2 = (q_1 + q_2)^2; \quad (2.1)$$

q_1 , q_2 can be expressed in terms of the electron and positron energies and momenta,

$$q_i^2 = (p'_i - p_i)^2 = -E'_i E_i (1 - \cos \theta_i), \quad i = 1, 2, \quad (2.2)$$

where θ_i is the angle of the scattered electron (positron) with respect to the beam axis. Note that the limit of quasi real photons, $q_i^2 \rightarrow 0$, corresponds to the configuration $\theta_i \rightarrow 0$, with electron and positron scattered by small angles.

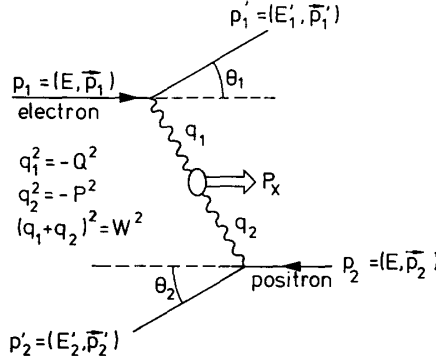


Figure 2.1: Kinematic of the two photon process (Fig. from [7]).

The transition matrix element for the $e^+e^- \rightarrow e^+e^-X$ process can be factorized into the product of three matrix elements, one for the electron, one for the positron

(simple QED amplitudes) and the last one for the $\gamma_1\gamma_2 \rightarrow X$ reaction [8],

$$T = \frac{e^4}{q_1^2 q_2^2} [\bar{u}(q_1)\gamma^{\mu_1}u(q_1)][\bar{v}(q_2)\gamma^{\mu_2}v(q_2)]A_{\mu_1\mu_2}^X, \quad (2.3)$$

where e is the electric charge, u and \bar{u} the electron free Dirac spinors, v and \bar{v} the positron free Dirac spinors; γ^{μ_1, μ_2} are Dirac matrices. The tensor $A_{\mu_1\mu_2}^X$ is related to the $\gamma_1\gamma_2 \rightarrow X$ transition matrix element

$$\langle X|T|\gamma_1\gamma_2\rangle = \epsilon_1^{\mu_1}\epsilon_2^{\mu_2}A_{\mu_1\mu_2}^X. \quad (2.4)$$

Working out the double differential cross section $d^2\sigma/dq_1^2 dq_2^2$ by squaring and integrating over all final states Eq.(2.3) is quite long and tedious [8]. In case both photons are nearly real, $q_1^2, q_2^2 \rightarrow 0$, one can express the differential cross section for the overall $e^+e^- \rightarrow e^+e^-X$ process in terms of the $\gamma\gamma$ cross section for transverse, quasi real photons,

$$d\sigma_{e^+e^- \rightarrow e^+e^-X} = \int_{\Omega_1, \Omega_2} L_{TT}\sigma_{TT} \frac{d\mathbf{p}'_1}{E'_2} \frac{d\mathbf{p}'_2}{E'_1}, \quad (2.5)$$

where L_{TT} contains terms depending only on measurable quantities p_i and q_i and the integration is performed over the angles of the outgoing leptons, up to a maximum value for the polar angle, $\theta = \theta_{max}$. Applying the Weizsäcker-Williams approximation (or *equivalent photon approximation*) to both $e^+ \rightarrow e^+\gamma$ and $e^- \rightarrow e^-\gamma$ subprocesses one can define the *photon distribution functions*

$$f_i(x_i) = \frac{\alpha}{\pi x_i} \left[(1 + (1 - x_i)^2) \ln \left(\frac{E(1 - x_i)}{m_e x_i} \theta_{i,max} \right) - 1 + x_i \right], \quad i = 1, 2, \quad (2.6)$$

where $x_i = q_i/P_i$ are the fractions of electron (positron) energy and momentum carried off by the radiated photons. Function (2.6) expresses the probability to find a photon of momentum fraction x_i in the electron (positron) field. A singularity is present in case of collinearity, when $\theta_{i,max} = 0$; in that sense, setting $\theta_{i,max} \neq 0$ is a sort of cut-off procedure to prevent divergent behaviors when performing integration. Defining the variable

$$z = x_1 x_2 = \frac{q_1 \cdot q_2}{P_1 \cdot P_2} = \frac{w^2}{4E^2} \quad (2.7)$$

the cross section can be written as

$$\sigma_{e^+e^- \rightarrow e^+e^-X} = \int dz \int_0^1 dx_1 \int_0^1 dx_2 \sigma_{\gamma\gamma \rightarrow X}(z) f_1(x_1) f_2(x_2) \delta(x_1 x_2 - z). \quad (2.8)$$

Introducing $r = \frac{x_1}{x_2}$ and changing variables one obtains

$$\sigma_{e^+e^- \rightarrow e^+e^-X} = \int dz \int dr \frac{\partial(x_1, x_2)}{\partial(z, r)} f_1 f_2 \sigma_{\gamma\gamma \rightarrow X}(z) = \int dz L_{\gamma\gamma}(z) \sigma_{\gamma\gamma \rightarrow X}(z), \quad (2.9)$$

where the so-called luminosity function $L_{\gamma\gamma}(z)$ is defined as

$$L_{\gamma\gamma}(z) = \int dr f_1(x_1) f_2(x_2) \frac{\partial(x_1, x_2)}{\partial(z, r)}. \quad (2.10)$$

The first expression for $L_{\gamma\gamma}(z)$ has been given by Low [9],

$$L_{\gamma\gamma}(z) = \left(\frac{2\alpha}{\pi} \ln \frac{E}{m_e} \right)^2 \frac{1}{2z} f(z), \quad (2.11)$$

with

$$f(z) = \frac{1}{2}(2+z)^2 \ln \frac{1}{z} + (1-z)(3+z). \quad (2.12)$$

The $\ln^2 E$ term in (2.11) represents the double collinear singularity: a logarithmic dependence is introduced for both integrations on θ_1, θ_2 when integrating near $\theta_{1,2} \simeq 0$.

2.1.1 $\gamma\gamma$ luminosity function

Depending on the degree of approximation when evaluating the cross section (2.5) and especially when performing integration over the phase space one can obtain different explicit functional forms for the luminosity function. Low's function (2.11) is obtained just cutting off the integral on both θ_1, θ_2 at a value $\theta \simeq (m_e/\sqrt{s})$ and keeping only the leading logarithmic term for each bremsstrahlung process. More involved formulas are available:

- Brodsky, Kinoshita and Terazawa released a luminosity function obtained applying the Weizsäcker-Williams approximation, performing integration on the whole solid angle and keeping next-to-leading orders [10]. The expression gets the form

$$L_{\gamma\gamma}(z) = 2 \left(\frac{\alpha}{\pi} \right)^2 \frac{1}{z} \left[\left(\ln \frac{E}{m_e} - \frac{1}{2} \right)^2 f(z) + \left(\ln \frac{E}{m_e} - \frac{1}{2} \right) g(z) + h(z) \right], \quad (2.13)$$

where $z = w^2/4E^2$ as before, $f(z)$ is the same as in Low's work and $g(z)$, $h(z)$ are expressions which arise from integration on the whole phase space. Studying the expression for the cross section before integration on $\theta_{1,2}$, an estimate of the fraction of the cross section as a function of the maximum scattering angle for electron and positron is given. The statement is that roughly $\frac{1}{2}$ of the cross section comes from the angles $\theta_{1,2} < (m_e/E)^{1/2}$, and roughly $\frac{3}{4}$ comes from $\theta_{1,2} < (m_e/E)^{1/4}$.

- In Budnev *et al.* paper [11] a similar functional form is presented, where a tri-logarithmic term is added, while the bi-log term is slightly modified. Showing explicit w^2 dependence the flux function reads

$$L_{\gamma\gamma}(w^2) = \left(\frac{\alpha}{\pi}\right)^2 \frac{1}{w^2} \left[\left(\ln \frac{sq_{max}^2}{w^2 m_e^2} \right)^2 f\left(\frac{s}{w^2}\right) - \frac{1}{3} \left(\ln \frac{s}{w^2} \right)^3 \right]. \quad (2.14)$$

In (2.14) the introduction of an explicit dependence on the maximum value of the squared mass of scattering photons q_{max}^2 is due to the introduction of a *dynamical* cut-off beside the kinematical cut-off related to each $e^\pm \rightarrow e^\pm \gamma$ process separately. In other words, a naive extension of the equivalent photon approximation from one photon to two photons is regarded not appropriate, even if numerical difference between (2.14) and BKT is small when $q_{max}^2 \simeq w^2$ and $\ln(s/w^2) \ll \ln(s/m_e^2)$. q_{max}^2 value is determined by experimental limitation (bounds on outgoing leptons polar angle); for hadronic production, $\gamma\gamma \rightarrow h$, q_{max}^2 is set at a typical scale $\simeq m_\rho^2$ in the case electron and positron are allowed to scatter anywhere, being m_ρ the mass of the ρ meson.

A completely different approach to determine the $\gamma\gamma$ flux function is followed in Bonneau, Gourdin and Martin work [8]. As in Budnev *et al.*, the authors here do not agree with the extension of the Weizsäcker-Williams method from one photon to two photons, and derive another expression for the 2-photons spectrum from a complete covariant matrix element calculation.

A comparison between the available functional forms for $L_{\gamma\gamma}$ is shown in Fig. 2.2.

2.1.2 Cross section for resonance production

We want now to consider the specific process $e^+e^- \rightarrow e^+e^-R$ where R is a resonant state with mass M , width Γ_0 and spin J . The $\gamma\gamma$ cross section as a function of the

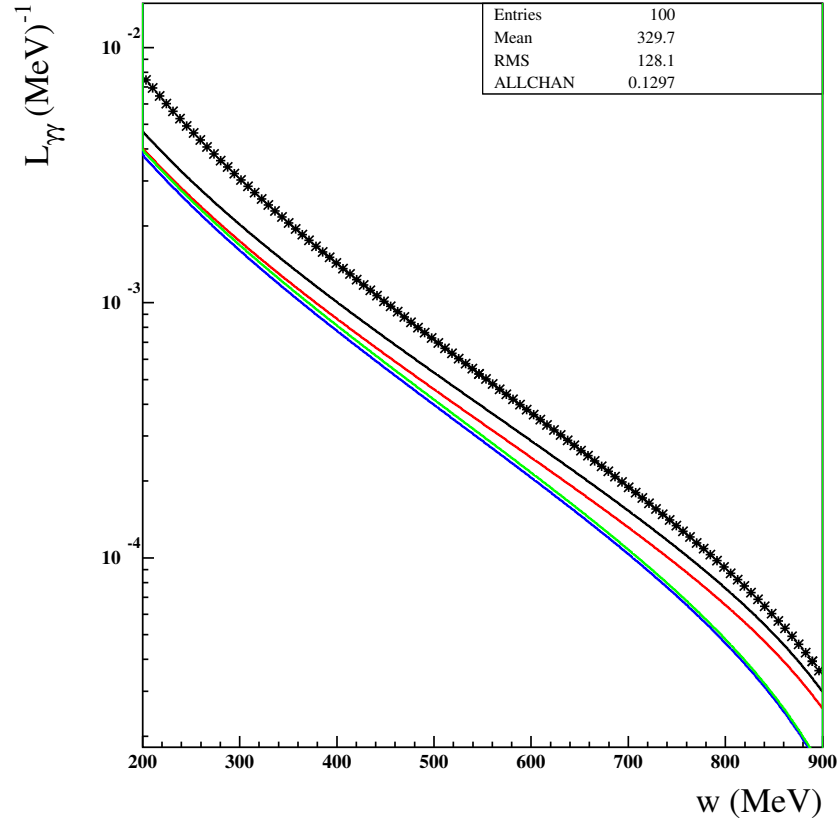


Figure 2.2: $\gamma\gamma$ flux as function of the two-photons invariant mass w^2 according to Low (black), leading-log Brodsky-Kinoshita-Terazawa (red), full BKT (blue), and Bonneau, Gourdin and Martin (green); the black pointed curve is the Budnev *et al.* version with $q_{max}^2 = m_\rho^2$.

energy in the $\gamma\gamma$ c.m.s can be described by a Breit-Wigner function

$$\sigma_{\gamma\gamma} = 8\pi(2J + 1) \left(\frac{M}{w}\right)^2 \frac{\Gamma_{\gamma\gamma}\Gamma_{tot}(w)}{(w^2 - M^2)^2 + M^2\Gamma_{tot}^2(w)}, \quad (2.15)$$

where $\Gamma_{\gamma\gamma}$ is the resonance decay width into two photons. The expression for the energy-dependent width $\Gamma_{tot}(w)$ is

$$\Gamma_{tot}(w) = \Gamma_0 \frac{M}{w} \left(\frac{p^*}{p_0^*}\right)^{2J+1} \frac{D_J(p_0^*r)}{D_J(p^*r)}, \quad (2.16)$$

where D_J are decay form factors [12], derived from a model of scattering on a constant potential with radius r [13]; p_0^* is the momentum of a decay particle in the resonance rest frame at the nominal resonance mass M , while p^* is the corresponding momentum at the invariant mass w . For a spin zero resonance, $D_0 = 1$ and considering the simple case of R decaying into two equal spinless particles with mass m one gets

$$\Gamma_{tot}(w) = \Gamma_0 \sqrt{\frac{1 - 4m^2/w^2}{1 - 4m^2/M^2}}. \quad (2.17)$$

The complete expression for the process is therefore

$$\sigma_{e^+e^- \rightarrow e^+e^-R} = 16M^2\pi \int \frac{dw}{w} \frac{\Gamma_{\gamma\gamma}\Gamma_{tot}(w)}{(w^2 - M^2)^2 + M^2\Gamma_{tot}^2(w)} L_{\gamma\gamma}(w); \quad (2.18)$$

just as a reminder, $L_{\gamma\gamma}$ has dimensions E^{-2} (see, for example, (2.11)), which makes Eq.(2.18) dimensionally correct.

2.2 Experimental aspects

The measurement of hadronic cross sections for $\gamma\gamma$ processes by identifying the final state in a 4π detector is challenging. Due to the kinematics (Lorentz boost when $x_1 \neq x_2$) and to the dynamics of hadron production (e.g. diffractive scattering) the final states are predominantly produced at small angles with respect to the beam axis. Moreover, it is somehow necessary to confine one or both outgoing leptons in a little cone around the beam axis, in order to identify the event as a photon-photon process and disentangle it from annihilation processes; electron and/or positron detection in this context has been named “tagging”. Both leptons tagging (or single lepton tagging) and the need for detection of final state particles at small polar angles

makes the employment of detectors with good particle detection efficiency in forward direction absolutely mandatory.

In the following, different tagging scenarios are described.

1. Double tagging at 0° (e.g., utilizing the accelerator structure as magnetic spectrometer): in this scenario both photons are nearly real and one can measure $\sigma_{\gamma\gamma} = \sigma_{TT}(q_1^2 = 0, q_2^2 = 0, w)$. There is no need to detect the state produced in $\gamma\gamma$ scattering in order to measure its invariant mass, as it can be determined from the outgoing lepton energies; but it is necessary to identify at least one of the final state particles (e, π, μ) if one wants to extract the hadronic cross section ($\sigma_{\gamma\gamma} = \sigma_{had} + \sigma_{QED}$).
2. Antitagging (or “tagging by absence”): an alternative way of confining outgoing leptons at small polar angles is requiring that neither electron or positron has been seen anywhere in the detector outside a narrow cone around the beam pipe; in order this strategy to work properly, the leptons detection has to be complete in a wide angular acceptance, say $20 < \theta < \pi - 20$ mrad. In this configuration the invariant mass $w_{\gamma\gamma}$ can no longer be determined from the scattered electron and positron momenta, and a good hadron detector is needed to reconstruct the final state particles. Absence of tagging leptons also makes the identification of $\gamma\gamma$ events unclear, and experimenters have to exploit strategies to separate the desired events from the annihilation channel.
3. Single tagging: only one of the outgoing leptons is tagged at 0° , with no tagging on the other side. This configuration gives access to both transverse-transverse photons cross section (σ_{TT}) and longitudinal-transverse photons cross section (σ_{LT}), which enter in the deep inelastic electron scattering off an (almost) real photon target.
4. Double tagging at finite angles: this configuration would allow to explore all photons virtualities, giving access to σ_{TT} , σ_{LT} and interference terms, τ_{TT} and τ_{LT} [7].

2.2.1 Experiments

In this last paragraph we present a brief review of experiments at e^+e^- colliders where $\gamma\gamma$ processes have been looked.

- with JADE detector at PETRA storage ring the reactions $e^+e^- \rightarrow e^+e^-\pi^0\pi^0$ and $e^+e^- \rightarrow e^+e^-\pi^0\eta$ have been studied with colliding beams of average energy

of 18 GeV. The partial width $\Gamma_{\gamma\gamma}$ has been measured for the $a_0(980)$ scalar meson and for the $f_2(1270)$ and $a_2(1320)$ tensor mesons; the cross section for the $\gamma\gamma \rightarrow \pi^0\pi^0$ has been extracted in the mass range $2.0 \div 3.5$ GeV [14]. A count spectrum in the $m_{\pi\pi} < w < 1$ GeV region has also been provided.

- The Crystal Ball experiment has analysed data collected at DESY with the e^+e^- collider DORIS II, using colliding beams of $\simeq 5.3$ GeV. This has been the first experiment to measure $\gamma\gamma \rightarrow \pi^0\pi^0$ cross section in the mass interval from production threshold ($\simeq 270$ MeV) up to 2 GeV. In the low invariant mass range, $m_{\pi\pi} < w < 0.6$ GeV, a flat cross section at almost 10 nb has been measured, interpreted as a continuum, non resonant production. At higher mass values, Crystal Ball observed the production of the $f_0(980)$ scalar meson and of the $f_2(1270)$ tensor meson; for both the partial width $\Gamma_{\gamma\gamma}$ have been quoted [15].
- The Belle collaboration has analysed the data collected at the asymmetric collider KEKB, measuring the $\gamma\gamma \rightarrow \pi^0\pi^0$ cross section in the $0.8 < w < 4.0$ GeV mass interval, obtaining results compatible with those from Crystal Ball [16].

Belle and Crystal Ball data for $\gamma\gamma \rightarrow \pi^0\pi^0$ cross section are shown in Fig.2.3.

2.2.2 KLOE contribution

The KLOE experiment will be described in details in the following chapter. In order to underline the contribution KLOE could give in studying the $\gamma\gamma \rightarrow \pi^0\pi^0$ reaction, providing competitive results with respect to existing measures, a comparison among the only two experiments which have explored the invariant mass region just above threshold (JADE and Crystal Ball) and KLOE is shown in Tab. 2.1 for crucial experimental features (energy resolution for $100 \div 700$ MeV photons, integrated luminosity \mathcal{L} , average beam energy).

Experiment	σ_E/E	\mathcal{L} (pb $^{-1}$)	Average beam energy (GeV)
JADE	$25 \div 10\%$	149	18
Crystal Ball	$0.027/(E(\text{GeV}))^{1/4}$	97	5.3
KLOE	$0.06/\sqrt{E(\text{GeV})}$	242.5	1

Table 2.1: Comparison among KLOE, JADE and Crystal Ball experiments.

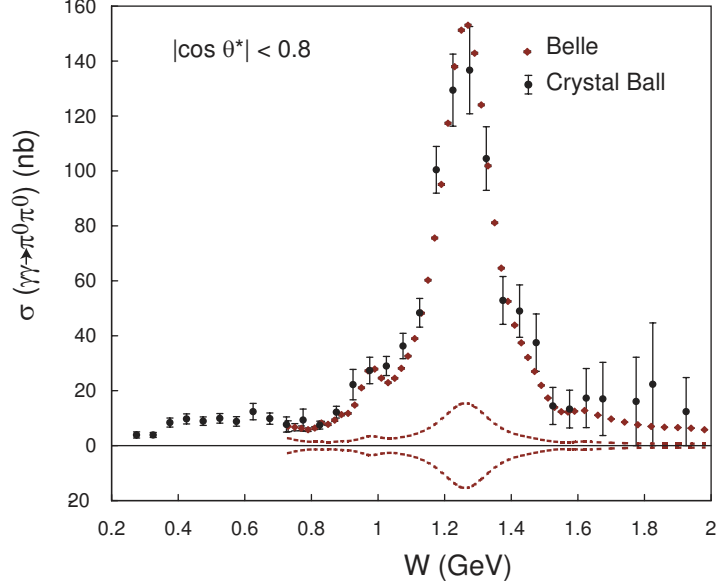


Figure 2.3: Cross section for the $\gamma\gamma \rightarrow \pi^0\pi^0$ process measured by Crystal Ball and Belle experiments.

From Tab. 2.1 one can see that KLOE wins the comparison with JADE as regards calorimeter energy resolution, while loses when compared to Crystal Ball. Data sample collected by KLOE is greatly more abundant than those collected both by JADE and Crystal Ball. Moreover, as both JADE and Crystal Ball work at high \sqrt{s} values they are affected by detection problems connected to forward boost much more than KLOE. The analysis performed on KLOE data, presented in this thesis, thus proposes a competitive result thanks to statistics and to particular favorable conditions to investigate the $\gamma\gamma \rightarrow \pi^0\pi^0$ process just above the production threshold.

Chapter 3

The KLOE experiment at DAΦNE

In 1989 the INFN (Italian Institute for Nuclear Physics) decided the realization of a high-luminosity e^+e^- collider to run at the ϕ resonance energy ($m_\phi = 1019.456 \pm 0.020$ MeV). That ϕ -factory has been built in the environment of Frascati National Laboratories, nearby Rome, and was placed in the building which had housed ADONE, the 3 GeV e^+e^- collider working from 1969 to 1993.

3.1 DAΦNE

DAΦNE is the acronym for Double Annular For Nice Experiment. It consists in two distinct storage rings, one for the electrons and one for the positrons, which cross in two interaction regions; keeping electron and positron beams separated allows to strongly reduce background sources due to interactions among bunches and greatly increases luminosity.

DAΦNE complex also comprehends a linear accelerator (LINAC) and a intermediate accumulation ring for both electrons and positrons. The LINAC is employed to accelerate electrons up to the final $\simeq 510$ MeV energy; LINAC also accelerate electrons up to $\simeq 250$ MeV in an intermediate station where positrons are produced, to be themselves accelerated up to 510 MeV. Electrons and positrons are then transferred in the intermediate accumulation ring to be injected as bunches in the main rings. As beams intensity rapidly decreases, the described operation is repeated several times each hour. Interactions occur one by one among one electrons and one positrons bunch in the rings crossing region.

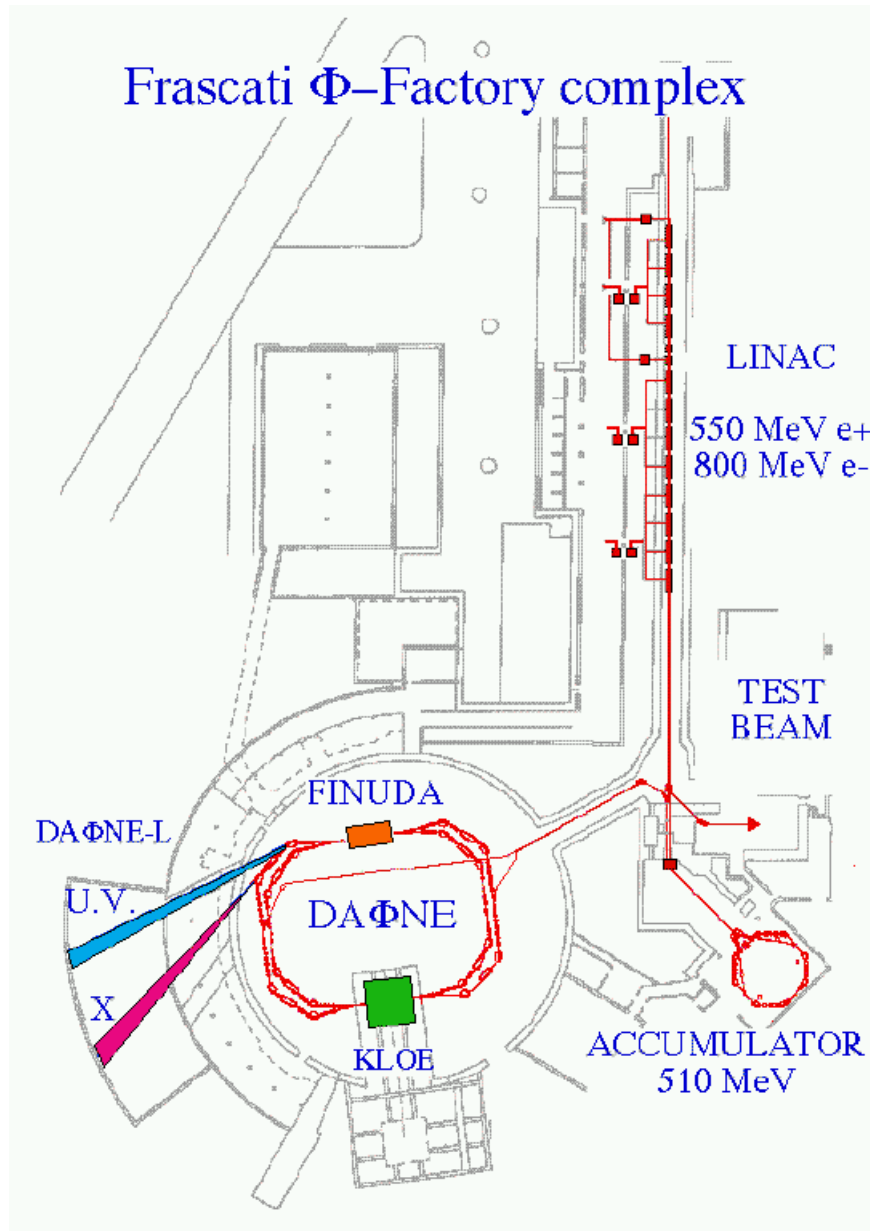


Figure 3.1: Complex of DAΦNE accelerators.

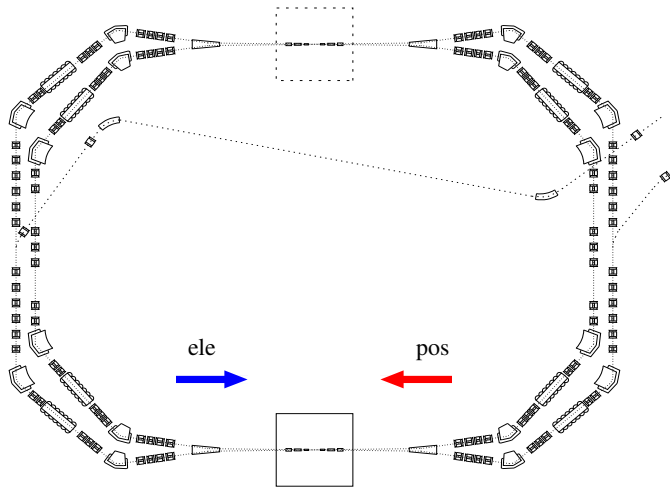


Figure 3.2: The double e^+e^- collision ring.

Electrons and positrons circulate in the ring grouped in n bunches with N particles each. The parameter which characterizes the collider is its luminosity \mathcal{L} , defined as the proportionality coefficient which relates the event rate w and the cross section σ , $w = \mathcal{L}\sigma$. Luminosity is proportional to n , N and to the beams revolution frequency ν :

$$\mathcal{L} = n \frac{\nu N^2}{4\pi\sigma_x\sigma_y} = n\mathcal{L}_0, \quad (3.1)$$

where σ_x , σ_y are the width r.m.s. of the beams in the transverse plane¹ where $\mathcal{L}_0 = \nu N^2/4\pi\sigma_x\sigma_y$ is the luminosity of each bunch. Luminosity could be limited by the electromagnetic interaction among the beams, which can be minimized by strongly focusing the beams around the interaction point using doublets or triplets of quadrupoles.

Electron and positron beams cross in the interaction point with a crossing angle of $\pi - 0.025$ rads on the zx plane; as a result the center-of-mass system does not exactly coincide with the lab frame, but is boosted towards the center of the rings with a momentum $\simeq 13$ MeV corresponding to $\beta_\phi \simeq 0.015$, $\gamma_\phi \sim 1.0001$ at a center-of-mass energy $\sqrt{s} = m_\phi$. In order to minimize crossing angle effects on beams dynamics and to make it as most similar as possible to that one would have with a crossing angle $= \pi$ the shape of bunches nearby the interaction point is made extremely flat (30 mm in the \hat{z} direction, 2 mm in the \hat{x} direction and 0.02 in the \hat{y} direction).

¹By convention the plane of the rings is the zx plane; the z axis coincides with the tangent to the ring at the interaction point.

3.2 KLOE Detector

KLOE Collaboration (K LOng Experiment) proposed the realization of a detector and the development of a scientific program to perform precision experiment on K meson physics in 1991. The KLOE detector was built and has been tested starting from summer 1998, to be then placed in the sud DAΦNE interaction region in early 1999. In the following seven years KLOE has collected a huge high quality data set which has been analyzed allowing a deep insight in K mesons physics. KLOE contributions deal with

1. new precision measurements of K mesons parameter and of their decays;
2. determination of the V_{us} element in the CKM matrix, tests on leptonic unitarity and universality, search for new physics;
3. light meson properties and spectroscopy;
4. quantum interferometry experiments;
5. tests on CP and CPT violation.

KLOE complexity and dimensions are comparable to those of general purposes contemporary detectors, such as those at LEP collider at CERN (Aleph, Delphi, Opal), even if working at much lower energies. It is worth stressing that the KLOE goal is to perform high precision physics and it is this purpose that determine the detector structure, its complexity, its dimension. To be more precise, KLOE big dimensions are due to the need to detect a sufficient fraction of K_L decays (when produced in $\phi \rightarrow K_S K_L$ with ϕ at rest the K_L mean free path is $\lambda_L = \gamma\beta c\tau = 340$ cm).

KLOE features are Le caratteristiche che KLOE deve soddisfare sono:

- high geometric acceptance;
- high an uniform efficiency on the entire K_L decay volume;
- high charged particles tracking efficiency;
- high photon detection efficiency.

The detector (Fig. 3.3) is a cylindrical apparatus located around one of the DAΦNE interaction points, with axis coincident with \hat{z} axis; dimensions are $\simeq 6 \times 6 \times 7$ m³. From the interaction points (IP) outwards, the principal detector components are

- a vacuum tube around the interaction point;
- two focusing quadrupoles, surrounded by small angles calorimeters (QCAL);
- a large drift chamber (DC) (see §3.2.1);
- an electromagnetic calorimeter (see §3.2.2);
- a superconducting solenoid which creates a 0.52 T axial magnetic field.

The vacuum tube surrounds the \hat{z} for all the detector length, and is spherically shaped with a $r = 10$ radius around the interaction point; this sphere, designed to contain almost all K_S decays ($r > 15\lambda_S$), has been constructed in a beryllium-aluminium mixture with a 0.5 mm thickness to minimize K_S regeneration and energy loss by ionization.

The two focusing quadrupoles are located around \hat{z} axis at 46 cm from the interaction point. The small angles calorimeters (QCAL) surround the focusing quadrupoles and consist in a sampling structure made of 1.9 mm absorbers layers (lead) alternating with 1 mm scintillating material, for a total thickness of $5.5 X_0$, where X_0 is the radiation length. Small angles calorimeters purpose is to detect photons which could otherwise be absorbed by quadrupoles; this task is mandatory when one wants to identify and reject photons from $K_L \rightarrow 3\pi^0$ decay when searching for $K_L \rightarrow 2\pi^0$ CP -violating events.

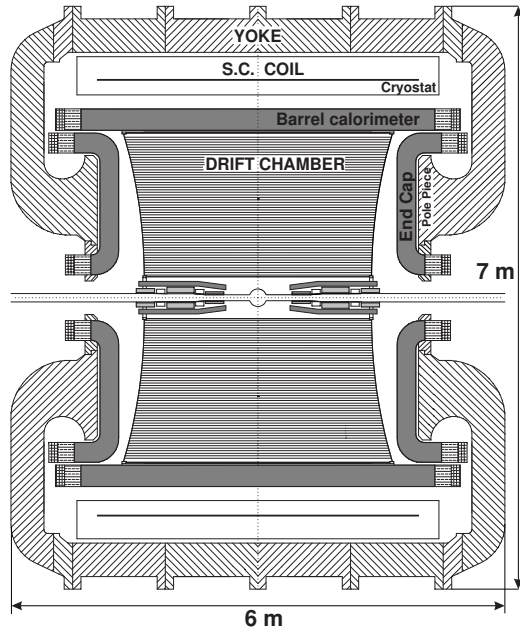


Figure 3.3: The KLOE detector.

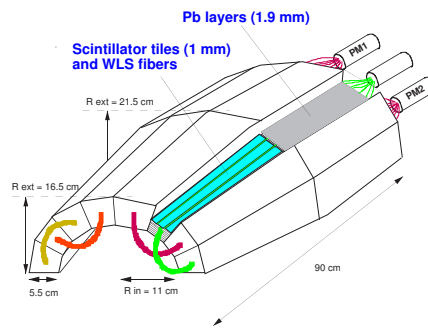


Figure 3.4: A small angle calorimeter (QCAL).

3.2.1 The Drift Chamber

The $25 < R < 200$ cm region houses a large drift chamber whose task is to perform tridimensional tracking of charged particles and to determine the K_L decay vertex with a ~ 1 mm accuracy on all the volume. It consists in a $R = 2$ radius cylinder with a 3.4 m length (along the \hat{z} axis), filled with gas. $\simeq 52000$ wires go through the volume, some at tension (+2000 volt, anodic wires), other at mass. When a charged particle enters the drift chamber, electrons produced by ionization along its trajectory in the gas are attracted by the anodic wires and, by a avalanche mechanism, a signal appears at the end of the wire. Complex front-end electronics allows detection of even weak signals and measurement of charges and drift times.

The total integrated charge collected provides information on the energy released by the particles. Moreover, particles which cross the same medium with same momentum p but different mass have different β and release different amounts of energy by ionization, $dE/dx \propto 1/\beta^2$; this mechanism is used as a particle identification method.

For such a detector challenge is due to the fact that the effective path for a particle is modified by multiple scattering, with a scattering angle $\propto 1/\sqrt{X_0}$, where X_0 is the radiation length, in its turn proportional to $1/Z^2$ (in gV/cm²) and to the mean density. Material chosen in order to have best performances are

- fcarbon fibers for the mechanical structure;
- a 90% helium, 10% isobutane admixture for the gas.

This choice also provides a high transparency and minimize the K_L regeneration processes.

The need for tridimensional tracking led to the choice of approximately squared, single anodic wire cells, organized in coaxial stereoscopic cylinders: wires are slightly sloping with respect to the detector axis in order to determine the longitudinal coordinate. The total cells number is 12582, arranged in 58 layers; cells in the 12 innermost layers have $\simeq 2$ cm side, those in the remaining 46 external layers $\simeq 3$ cm. Signals which propagate through anodic wires (“hits”) are amplified and discriminated, before being sent to TDC converters with a time resolution of $\simeq 1$ ns.

3.2.2 The Electromagnetic Calorimeter

Neutral K_L , K_S and K^\pm decay products are photons, generated both directly or through neutral pions decays. Energetic photons interact with matter producing electron-positron pairs which, in their turn, radiate photons. A photon, passing through a dense, high Z material, starts an iterative conversion-radiation process until all its energy is converted in an electromagnetic shower of e^+e^- and photons. Measuring shower energy it is possible to reconstruct the primitive photon energy; this task is performed by the electromagnetic calorimeter, which determines the space-time coordinates of the photon, too.

KLOE electromagnetic calorimeter (EMC) was designed to satisfy several strict requests:

- good energy resolution,

$$\frac{\sigma_E}{E} \simeq \frac{0.06}{\sqrt{E(\text{GeV})}}; \quad (3.2)$$

- excellent time resolution in order to reconstruct neutral K_L decay vertexes,

$$\sigma_T \simeq \frac{57 \text{ ps}}{\sqrt{E(\text{GeV})}} \oplus 100 \text{ ps}; \quad (3.3)$$

- high reaction speed, as one wants to use the EMC signal as primary trigger (see §4.1).

In this case a sampling calorimeter has been chosen, with alternating inert lead layers which enhance the showering process and scintillating materials layers. To be more precise, 0.5 mm lead sheets have been used with semicylindrical grooves (0.5 mm radius) in which scintillating fibers are housed; fibers are thus located between lead layers without suffering compression. Fibers are located at the vertexes of equilateral triangles of side 1.35 mm. Around 200 layers are piled up, glued and pressed to form a compact material, in which the volume ratio fibers:lead:epoxy is 48:42:10, with an average density of 5 g/cm³ and a radiation length $X_0 = 1.5$ cm. This material is then modeled in around 23 cm thick modules ($\simeq 15X_0$). 24 trapezoidal section modules are organized along the detector axis to cover all the azimuthal angle, closing the lateral surface of the drift chamber: this central section of the calorimeter is named *barrel*. Other 32 squared or rectangular section modules form the two *endcaps* which surround the superconducting magnet poles and hermetically close the calorimeter, covering 98% of the solid angle.

Light produced by scintillation in the fibers is collected and read on both sides of each module using plexiglass light guides optically coupled to photomultipliers. Photomultipliers signals are then divided and sent to the ADCs for energy measurements and for the trigger system, and to the TDCs for time measurements. Segmentation introduced by the front-end read out makes the calorimeter divided into 2440 squared cells of side $\simeq 4.4$ cm.

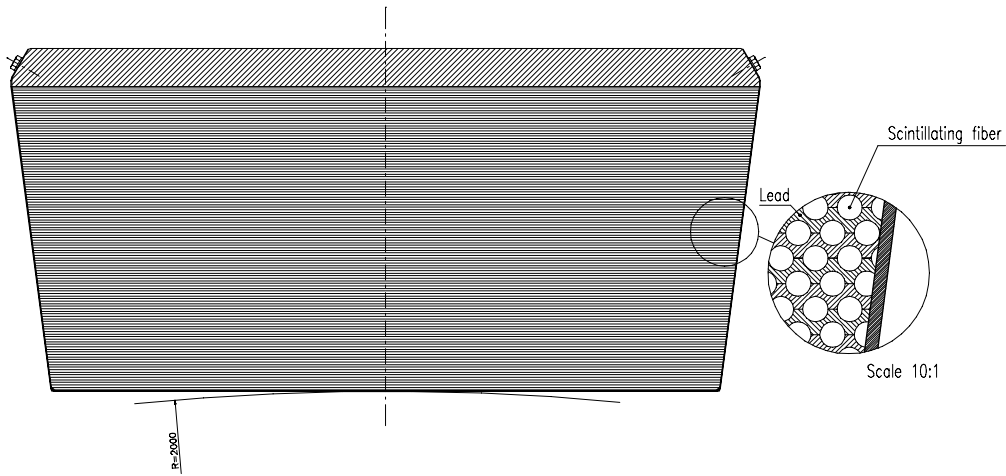


Figure 3.5: Transversal section of a calorimeter module.

3.3 Reconstruction Algorithms

In this section we briefly describe the procedures to get information about particles positions, times (respect to the bunch crossing) and energies, starting from signals registered in the calorimeter and in the drift chambers.

3.3.1 Cluster Reconstruction

Indicating by A and B the ends of each calorimeter cell, the particle arrival time t and its coordinate s along the fiber (assuming the origin at the middle of the fiber) are obtained from the TDC counts $T^{A,B}$:

$$t(\text{ns}) = \frac{t^A + t^B}{2} - \frac{t_0^A + t_0^B}{2} - \frac{L}{2v}, \quad (3.4)$$

$$s(\text{cm}) = \frac{v}{2} (t^A - t^B - t_0^A + t_0^B), \quad (3.5)$$

with

$$t^{A,B} = c^{A,B} \times T^{A,B},$$

where $c^{A,B}$ (ns/TDC counts) are TDC calibration constants, $t_0^{A,B}$ are offset times and L , v are the cell length and the light speed in the fibers, respectively.

Signal energy E is obtained on each side of the i -th cell from the signal of amplitude S (in ADC counts) registered by the correspondent photomultiplier:

$$E_i^{A,B}(\text{MeV}) = k_E \frac{S_i^{A,B} - S_{0,i}^{A,B}}{S_{M,i}}, \quad (3.6)$$

where $S_{0,i}$ is the offset amplitude and $S_{M,i}$ is the response for a particle which pass through the center of the calorimeter at minimum of ionization; k_E is the energy scale factor (in MeV) obtained using showers of known energy particles. Cell energy E_i is assumed to be equal to the average of the energies at each end, weighted for a correction factor $A_i^{A,B}(s)$ which takes in account the light degradation while passing along the fiber as a function of the impact coordinate s ,

$$E_i(\text{MeV}) = \frac{(E_i^A A_i^A + E_i^B A_i^B)}{2}. \quad (3.7)$$

Costants $S_{M,i}$ and $A_i^{A,B}(s)$ are determined using a dedicated trigger before the starting of each acquisition period. Offset times and light speed in the fibers are continuously estimated using high energy cosmic rays selected thanks to information provided by the drift chamber.

Reconstructed position and energy-time correction as function of the s impact coordinate are evaluated for each cell with a hit. Cluster reconstruction algorithm then looks for a group of $R\varphi$ (for barrel) or xz (for endcaps) contiguous cells grouping them in pre-cluster, being φ the azimuthal angle. Pre-cluster longitudinal coordinate and arrival time is then used to perform the *merging* or the *splitting* of the cells, obtaining the final cluster. Cluster energy is the sum of the component cell energies; position (x_{cl}, y_{cl}, z_{cl}) and time (t_{cl}) are evaluated as energy-weighted averages of components cell coordinates.

Cells are included in cluster formation only if have both ends times and energy signal available; otherwise, they are classified as *incomplete* cells. A incomplete cell can be included in a cluster after cluster formation if the comparison between its coordinates xy (xz on the endcaps) are compatible with those of the cluster centroid.

Fragments production (splitting) from electromagnetic shower is investigated by data-Monte Carlo comparison for $e^+e^- \rightarrow \gamma\gamma$ process, applying cuts on most energetic clusters. One can study the minimum distance between the centroid of the most energetic cluster (“gold” photon) and other clusters centroids,

$$\Delta R = \sqrt{\left(x_{cl}^{gold} - x_{cl}^i\right)^2 + \left(y_{cl}^{gold} - y_{cl}^i\right)^2 + \left(z_{cl}^{gold} - z_{cl}^i\right)^2}; \quad (3.8)$$

Monte Carlo distributions in this variable are in good agreement with data only for high ΔR values, while at small values agreement is poor, due to an erroneous fragment simulation.

Procedure employed in the analysis to heal cluster splitting is described in §6.1.

Chapter 4

Data acquisition

Data used for the analysis have been collected by the KLOE detector at DAΦNE e^+e^- collider running at $\sqrt{s} = 1$ GeV in the period 17.12.2005 - 16.3.2006; the collected sample corresponds to an integrated luminosity $\mathcal{L} = 242.5 \text{ pb}^{-1}$. Average data acquisition conditions are listed in Tab. 4.1.

Parameter	average value
\sqrt{s}	1000.1 MeV
transverse momentum e^+e^-	12.7 MeV ($-\hat{x}$)
Luminosity	$7 \cdot 10^{31} \text{ cm}^{-2} \text{ s}^{-1}$
acquisition rate	1.7 kHz
current e^-	1.1 A
current e^+	0.7 A

Table 4.1: Average values for data acquisition parameters.

Collected data have been filtered by the background rejection filter and then processed according to criteria optimized in order to study $\gamma\gamma$ interactions (§4.3).

4.1 The Trigger system

Events frequency at DAΦNE at its maximum luminosity is of 2.5 kHz for ϕ events, 50 kHz for Bhabha events, 2.5 kHz for cosmic events and $\simeq 100$ kHz for machine background events. The trigger system must therefore reduce background events as much as possible, in order not to overload the data acquisition system and minimize dead times. At the same time, a high efficiency has to be guaranteed for ϕ events

and a fraction of Bhabha and cosmic events, necessary for calibration procedures, has to be stored.

The trigger system is based on the energy deposits in the calorimeter and on information provided by the drift chamber. It is composed of two levels: a first level produce a fast signal which activates the Front-End Electronics (FEE). After the first trigger signal has arrived, further information from the drift chamber are acquired in order to decide whether confirm or not the first level trigger and activate the Data Acquisition system (DAQ). First level trigger accepts events which satisfy at least one of the following conditions:

- two clusters in the calorimeter with energy greater than a threshold (LET, Low Energy Threshold) with the possible configurations barrel-barrel, barrel-endcap and endcap-endcap (but in the last case the two clusters have not to be on the same endcap). Energy thresholds are 50 MeV for the barrel and 150 for the endcaps;
- at list 1 hit in 15 drift cells within 250 ns.

Calorimeter TDC converters then measure the time with respect to the bunch crossing. This method allows to keep time resolution of the order of some ps. Second level trigger selects events according to the following criteria:

- in the calorimeter, at least one fired sector in the barrel or three sectors fired in the endcaps;
- in the drift chamber, at least one hit in the 850 ns following the first level trigger signal.

4.2 Background Rejection Filter

This filter is mostly based on calorimetric information; it employs three distinct strategies to individuate and reject three different kinds of events: cosmic rays, Bhabha-like events, machine background.

Cosmic rays. The event is recognized and rejected as a cosmic ray if at least one of the following condition is verified:

- the time interval between the innermost and the outermost cells of the first time-ordered cluster is negative, $\Delta T = T_{out} - T_{in} < 0$: this condition defines a particle incoming from outside the detector;

- the time distance Δt and the space distance ΔR between first two time-ordered clusters are such that $\Delta t > a\Delta R + b$, with $a = 0.034$ ns/cm, $b = -1.15$ ns.

Bhabha and Bhabha-like events. Bhabha-like events are defined a Bhabha which interact in the small angles calorimeters. Criteria to reject such events are the following:

- number of clusters in the event must be ≤ 7 ;
- the *event axis* \hat{a} , defined by the most energetic cluster centroid, has to form a angle $\theta_a < 35^\circ$ with respect to the z axis;
- the energy-weighted squared average of the clusters distances from the \hat{a} axis has to satisfy the relation

$$\bar{d} = \sqrt{\frac{\sum_i d_i^2 E_i}{\sum E_i}} < 90 \text{ cm}, \quad (4.1)$$

where d_i and E_i are the i -th cluster distance from \hat{a} and i -th cluster energy, respectively.

Machine background. Physical processes which contribute to this background are:

1. multiple Coulomb scattering from residual gas;
2. bremsstrahlung in the residual gas in the vacuum chamber and on the beam pipe walls;
3. Touschek effect, that is Coulomb scattering among particles belonging to the same bunch.

Information from calorimeter as not enough to reject these events; number of *hits* in the drift chamber are then used, too, being a hit the signal presence on one of the wires. A preliminary selection to identify machine background events requires

- $N_{hits} < 200$;
- number of clusters in the calorimeter $2 \leq N_{clu} \leq 6$, with total energy $E_{tot} < 1.7$ GeV.

Events are then rejected applying cuts on polar angles of the two most energetic clusters and on the ratio of hits number in the 12 innermost layer of the DC on the total hits number.

4.3 $\gamma\gamma$ filter

Unlike ϕ production processes, where final state particles release huge energy amounts in the calorimeter, in $\gamma\gamma$ interactions available energy is mostly taken off by final state electron and positron which typically escape detection; the energy release in the calorimeter is thus rather small. The $\gamma\gamma$ filter [17], has been designed to dedicate studies of the reactions:

- $e^+e^- \rightarrow e^+e^-\sigma$;
- $e^+e^- \rightarrow e^+e^-\pi^0$;
- $e^+e^- \rightarrow e^+e^-\eta$.

$\gamma\gamma$ filter requests are

1. at least two prompt clusters in the calorimeter, not associated to tracks (photons);
2. both photons with $E_{\gamma_1}, E_{\gamma_2} > 15$ MeV and polar angle $20^\circ < \theta_{\gamma_1, \gamma_2} < 160^\circ$;
3. at least one photon with $E > 50$ MeV;
4. ratio $R = (E_{\gamma_1} + E_{\gamma_2})/E_{tot}$ has to be $R > 0.3$;
5. $100 \text{ MeV} < E_{tot} < 900 \text{ MeV}$, in order to reject low energy background events and high rate Bhabha events $e^+e^- \rightarrow \gamma\gamma$.

Chapter 5

The process $e^+e^- \rightarrow e^+e^-\pi^0\pi^0$ and backgrounds

In this chapter the signal process $e^+e^- \rightarrow e^+e^-\pi^0\pi^0$ and background processes are described. As experiment is performed in the no-tag mode, annihilation reactions with two pions (that is 4 photons) in the final state are sources of backgrounds; contamination arise from higher photons multiplicities processes, too, due to possible photon loss or erroneous cluster counting. The following reactions have been taken in account as background processes:

- $e^+e^- \rightarrow K_S K_L, K_S \rightarrow \pi^0\pi^0$;
- $e^+e^- \rightarrow \eta\gamma, \eta \rightarrow \pi^0\pi^0\pi^0$;
- $e^+e^- \rightarrow \omega\pi^0, \omega \rightarrow \pi^0\gamma$;
- $e^+e^- \rightarrow f_0\gamma, a_0\gamma$;
- the $e^+e^- \rightarrow \gamma\gamma$ process is taken in account too, as the cross section is very large and multiplicity can rise from 2 to 4 due to cluster splitting.

Monte Carlo generator for $e^+e^- \rightarrow e^+e^-\pi^0\pi^0$ process is described in §5.1; for main background processes simulation features are studied, first data-MC comparison are made and corrections are applied.

5.1 $e^+e^- \rightarrow e^+e^-\sigma \rightarrow e^+e^-\pi^0\pi^0$

Generator for signal events is described in [18]. Production of a scalar meson (σ) as a resonant intermediate state is assumed in this simulation: the σ meson is regarded

as a $[qq][\bar{q}\bar{q}]$ state and its resonant production is described using a Breit-Wigner function, see Eq.(2.15). Three different productions have been made, using for σ meson mass and width the values quoted by the experiments *E791*, *CLEO* and *BES*, listed in Tab.5.1. No double equivalent photon approximation is applied in the process evaluation. The complete matrix element is evaluated from the amplitude

$$\mathcal{M} = \langle e^+e^-\pi^0\pi^0 | \mathcal{O} | e^+e^- \rangle, \quad (5.1)$$

where \mathcal{O} is an operator which connects the σ meson to the two photons and to the neutral pions. In Fig.5.1 the t-channel and the s-channel Feynman diagrams contributing to \mathcal{M} are shown. The $\sigma\gamma\gamma$ vertex is described assuming Vector Meson Dominance (VMD): $\gamma\gamma \rightarrow \sigma$ transition is mediated by two ρ vector mesons. Interpreting σ as a $[qq][\bar{q}\bar{q}]$ state, the $\sigma \rightarrow \rho\rho$ transition can be described as sketched in Fig. 5.2: a quark and a antiquark tunnel the diquark and antidiquark potential barrier respectively, and bound to form a $q\bar{q}$ meson.

Experiment	Mass (MeV)	Width (MeV)
E791[4]	$478_{-23}^{+24} \pm 17$	$324_{-40}^{+42} \pm 21$
CLEO[6]	513 ± 32	335 ± 67
$M - i\Gamma/2$		
BES[5]	(541 ± 39)	$-i(252 \pm 42)$

Table 5.1: σ meson mass and width quoted by *E791*, *CLEO* e *BES* and used in the MC simulation. [4, 6] values are obtained fitting data with a Breit-Wigner function, while [5] quotes the pole $M - i\Gamma/2$ obtained in a partial waves analysis.

5.1.1 Angular distribution of the final state e^\pm

Angular distribution of the outgoing leptons and its connection with the issue of the luminosity function has been studied considering subsets of the generated events defined by the request

$$\vartheta_{pos} < \theta_{max}, \quad \vartheta_{ele} > (\pi - \theta_{max}); \quad (5.2)$$

in Eq. 5.2 a request on generated (not reconstructed) variables is understood.

In Tab.5.2 number of generated events and number of events in the subsets defined by the condition (5.2) for different values of θ_{max} are listed for the three Monte Carlo simulations in exam. As will be shown in §7.1, convolution of the $\gamma\gamma \rightarrow \pi^0\pi^0$ cross section by the luminosity function and resolution effects almost completely wipe out

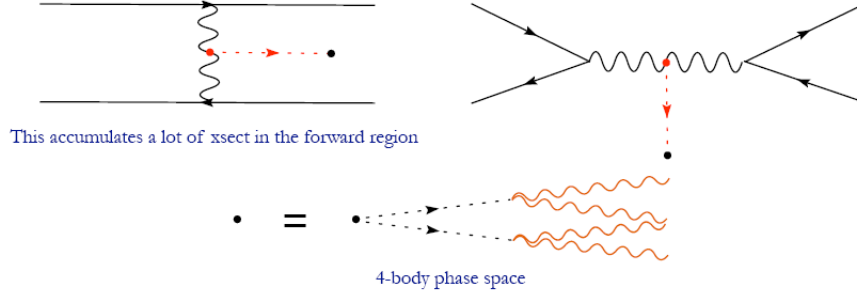


Figure 5.1: α^2 Feynman diagrams which contributes to amplitude (5.1).

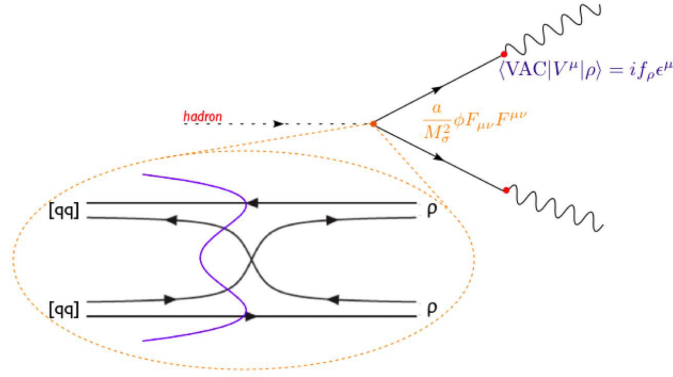


Figure 5.2: $\sigma\gamma\gamma$ vertex assuming Vector Meson Dominance: the $[qq][\bar{q}\bar{q}]$ state decays in two ρ vector mesons, which then convert into two photons.

Experiment	E791	CLEO	BES
generated	39044	39001	48776
$\theta_{max} = 20^\circ$	25742 (0.659)	25875 (0.663)	34372 (0.705)
$\theta_{max} = 18^\circ$	24747 (0.634)	24907 (0.639)	33234 (0.681)
$\theta_{max} = 15^\circ$	23000 (0.589)	23223 (0.595)	31209 (0.639)
$\theta_{max} = 13^\circ$	21657 (0.555)	21867 (0.561)	29682 (0.608)
$\theta_{max} = 11^\circ$	20120 (0.515)	20420 (0.523)	27893 (0.572)

Table 5.2: Number of generated $e^+e^- \rightarrow e^+e^-\sigma \rightarrow e^+e^-\pi^0\pi^0$ events and subsets defined by the request $\vartheta_{pos} < \theta_{max}$, $\vartheta_{ele} > (\pi - \theta_{max})$; reduction factors are in brackets.

any difference between distributions generated using different values for the σ meson mass and width, so a particular choice for these values does not introduce relevant systematic effects in modeling the $e^+e^- \rightarrow e^+e^-\sigma \rightarrow e^+e^-\pi^0\pi^0$ process; the following studies and plots have been done using the Monte Carlo simulation in which the σ meson is modeled according to *BES* parameters. Distributions in the final state ($2\pi^0$) invariant mass and in the quadri-momenta of the scattering photons are plotted in Fig. 5.3 for the complete generated sample and for the subsets corresponding to $\theta_{max} = 20^\circ, 15^\circ$ and 11° . As expected, confining outgoing leptons in a smaller and smaller polar angle cone translates in forcing radiated photons to be more and more real, while no request on $\theta_{ele,pos}$ let q_{max} values up to the $\rho(770)$ mass scale. Factorizing the process as

$$\frac{d\sigma_{e^+e^- \rightarrow e^+e^-X}}{dw} = \sigma_{\gamma\gamma}(w)L_{\gamma\gamma}(w), \quad (5.3)$$

and being the counting spectrum $\frac{dn}{dw} \propto \frac{d\sigma}{dw}$, one can consider the w spectrum deconvolution

$$\frac{1}{L_{\gamma\gamma}(w)} \frac{dn}{dw} \propto \sigma_{\gamma\gamma}(w), \quad (5.4)$$

where the proportionality holds up to an integrated luminosity factor \mathcal{L} . One would expect stability of $\frac{1}{L_{\gamma\gamma}} \frac{dn}{dw}$ under variation of the domain of integration on scattered leptons polar angles. Of course appropriate integration on phase space when determining flux function has to be performed in each case, according to θ_{max} value. To this aim, Budnev *et al.* parametrization for the flux function has been employed, using q_γ^{max} as cutoff in integration (see §2.1.1). In Tab. 5.3 q_γ^{max} values obtained for the different MC subsets are listed; these values have been plugged in the Budnev flux formula (2.14). The obtained differential $L_{\gamma\gamma}$ functions, integrated bin-per-bin, are shown in Fig.5.4 (top panel). The $\frac{1}{L_{\gamma\gamma}} \frac{dn}{dw}$ are plotted in Fig.5.4, bottom panel, showing a remarkable stability.

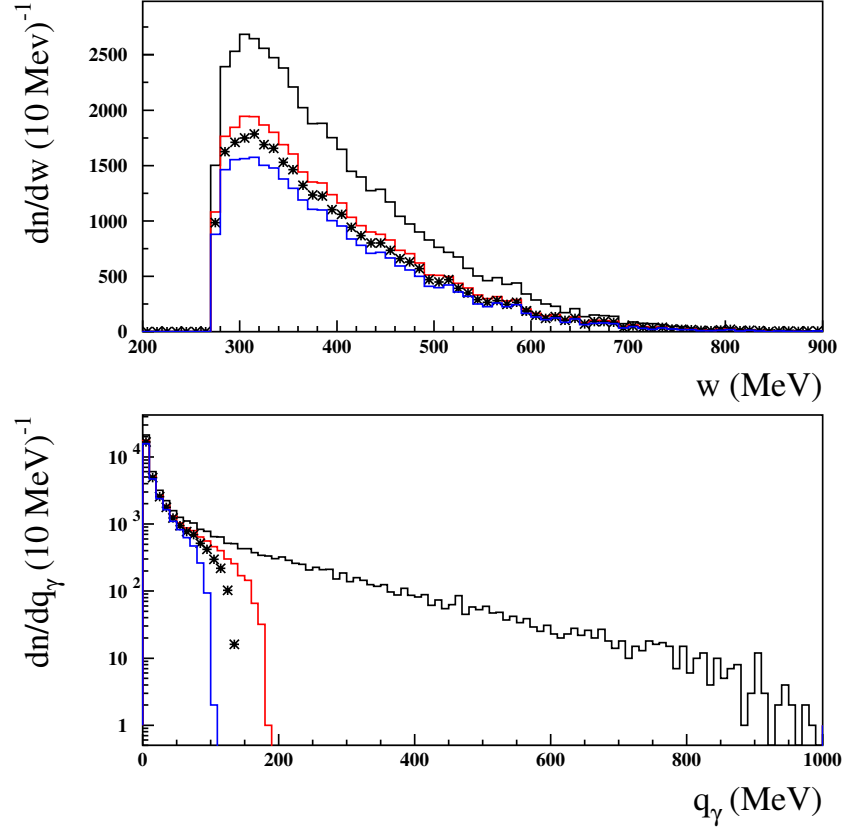


Figure 5.3: Distributions in the final state invariant mass (top) and in the quadrimomenta of the scattering photons (bottom) for the complete generated sample (black) and for the subsets corresponding to $\theta_{max} = 20^\circ$ (red), $\theta_{max} = 15^\circ$ (stars) and $\theta_{max} = 11^\circ$ (blue).

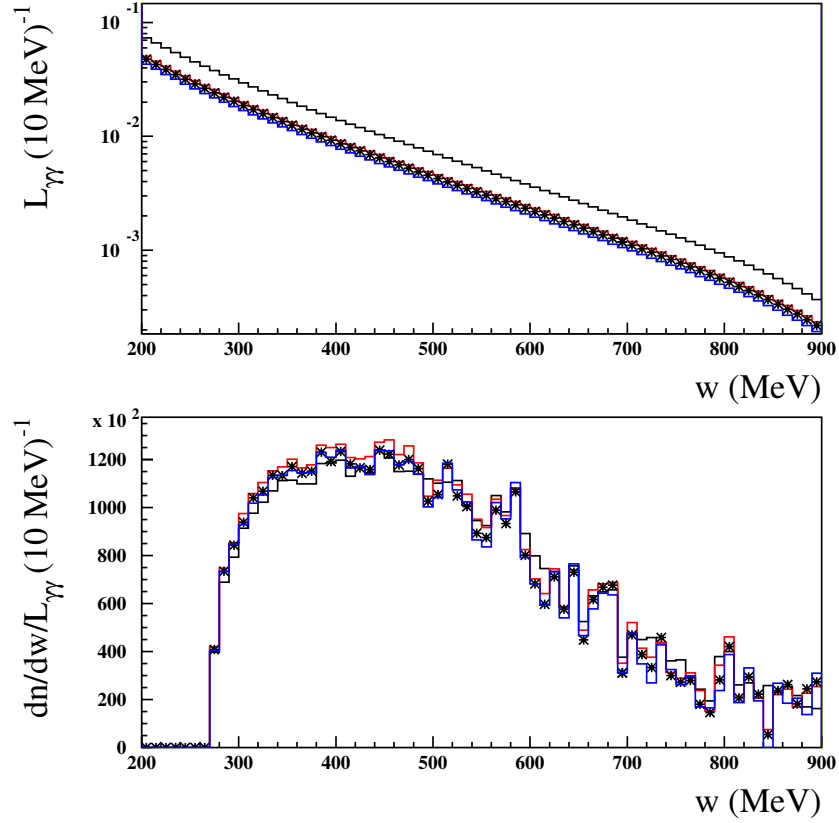


Figure 5.4: Bottom panel: $\frac{1}{L_{\gamma\gamma}} \frac{dn}{dw}$ extracted from Monte Carlo $e^+e^- \rightarrow e^+e^-\pi^0\pi^0$ events for the complete generated sample (black) and for the subsets corresponding to $\theta_{max} = 20^\circ$ (red), $\theta_{max} = 15^\circ$ (stars) and $\theta_{max} = 11^\circ$ (blue). Corresponding $\gamma\gamma$ fluxes (according to Budnev *et al.* recipe), used to divide invariant mass spectra, are shown in the top panel.

θ_{max}	q_γ^{max} (MeV)
20°	175
18°	160
15°	140
13°	120
11°	100

Table 5.3: Values of q_γ^{max} for different θ_{max} cut.

5.2 $e^+e^- \rightarrow K_S K_L$

This is the main background process for the $e^+e^- \rightarrow e^+e^-\pi^0\pi^0$ analysis, as $K_S \rightarrow \pi^0\pi^0$ decay (BR $\simeq 31\%$) produces a peak in the 4γ invariant mass spectrum at $m_{4\gamma} \simeq m_{K_S} \simeq 497$ MeV, next to the region where $\sigma \rightarrow \pi^0\pi^0$ signal is expected.

The neutral kaons are emitted back-to-back ; K_S events can be detected and rejected by tagging a K_L in the opposite direction, which is possible when the K_L releases a clear signal in the electromagnetic calorimeter (“ K_L crash”); this procedure will be referred to as “ K_S tagging ”. The $e^+e^- \rightarrow K_S K_L$ process represents an irreducible background when K_L neither decays in the drift chamber nor interacts in the electromagnetic calorimeter, escaping detection at all.

Because of its importance as background process for the $e^+e^- \rightarrow e^+e^-\pi^0\pi^0$ analysis, $K_S K_L$ events have been studied in detail, mostly in order to measure $e^+e^- \rightarrow K_S K_L$ at $\sqrt{s} = 1$ GeV. This process has also been used to check the data-MC agreement in the $m_{4\gamma}$ variable, introducing a correction to the MC energy scale.

A sample of 19571400 $K_S K_L$ generated events has been employed in the analysis.

5.2.1 MC Energy Calibration

For this task there is no interest in absolute normalization, as one just wants to compare data and MC distribution shapes. The goal is to select both in data and MC a pure sample of $K_S K_L$ events with $K_S \rightarrow \pi^0\pi^0$; the K_S tagging is therefore useful here. Events are selected asking for

1. no tracks in the drift chamber;
2. at least 4 prompt clusters;
3. at least one “ K_L crash” cluster candidate.

As in the $e^+e^- \rightarrow e^+e^-\pi^0\pi^0$ analysis, prompt clusters are defined by the space-time relation $|t - \vec{r}/c| < 5\sigma_t$, and must have energy of at least 15 MeV and be in the angular acceptance $23^\circ < \vartheta < 157^\circ$; details will be provided in §6.1. Following standard KLOE analysis procedures, “ K_L crash” cluster candidate is defined as a cluster *in the barrel* with $E > 100$ MeV and $0.092 < \beta^* < 0.105$. The 4γ from $\pi^0\pi^0$ decays invariant mass is reconstructed as follows. The χ^2 -like variable is considered

$$\chi_{\pi\pi}^2 = \frac{(m_{\pi^0} - m_{ij})^2}{\sigma_{ij}^2} + \frac{(m_{\pi^0} - m_{kl})^2}{\sigma_{kl}^2}, \quad (5.5)$$

where m_{ij} is the two-photons invariant mass,

$$m_{ij} = \sqrt{2E_i E_j (1 - \cos \theta_{ij})}, \quad (5.6)$$

and σ_{ij} is the two-photons invariant mass resolution, given by (here the uncertainty on the angle θ_{ij} between the photons can be neglected),

$$\sigma_{ij} = \frac{m_{ij}}{2} \left(\frac{\sigma_{E_i}}{E_i} \oplus \frac{\sigma_{E_j}}{E_j} \right). \quad (5.7)$$

For each event with $n \geq 4$ the variable $\chi_{\pi\pi}^2$ is evaluated for all the $3 \times \binom{n}{4}$ possible combinations of pairing n photons two-by-two; the combination corresponding to the lowest value of $\chi_{\pi\pi}^2$ is chosen as the best pairing and the invariant mass of the 4-photon system ($m_{4\gamma}$) is evaluated. In Fig. 5.6 (top panel) distributions in $m_{4\gamma}$ are shown for data and MC after selections 1-3; a shift between the distribution is observed, which is healed just applying a 8‰ correction to MC clusters energies. Data-MC comparison after applying this correction is shown in the bottom panel. From now on the 8‰ correction to MC energy scale is applied **in all simulated processes**.

The 8‰ correction has been determined considering gaussian fit to both data and $K_S K_L$ Monte Carlo distributions in the $430 \div 550$ MeV range, as shown in Fig. 5.5. The relative difference between the mean returned from fit to data (μ_{data}) and the mean returned from fit to MC (μ_{MC}) is

$$\frac{\mu_{data} - \mu_{MC}}{\mu_{MC}} = \frac{488.4 - 484.5}{484.5} = 0.008049, \quad (5.8)$$

which is exactly the 8‰ rescaling to be applied to simulated cluster energies.

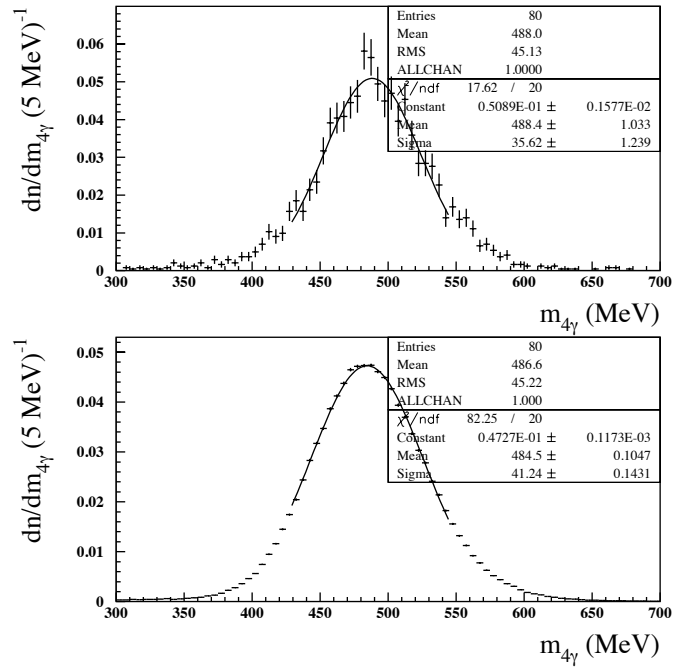


Figure 5.5: Distributions in $m_{4\gamma}$ for data (top) and $K_S K_L$ MC (bottom), both selected with cuts 1-3. In the $430 \div 550$ MeV interval a gaussian fit has been performed.

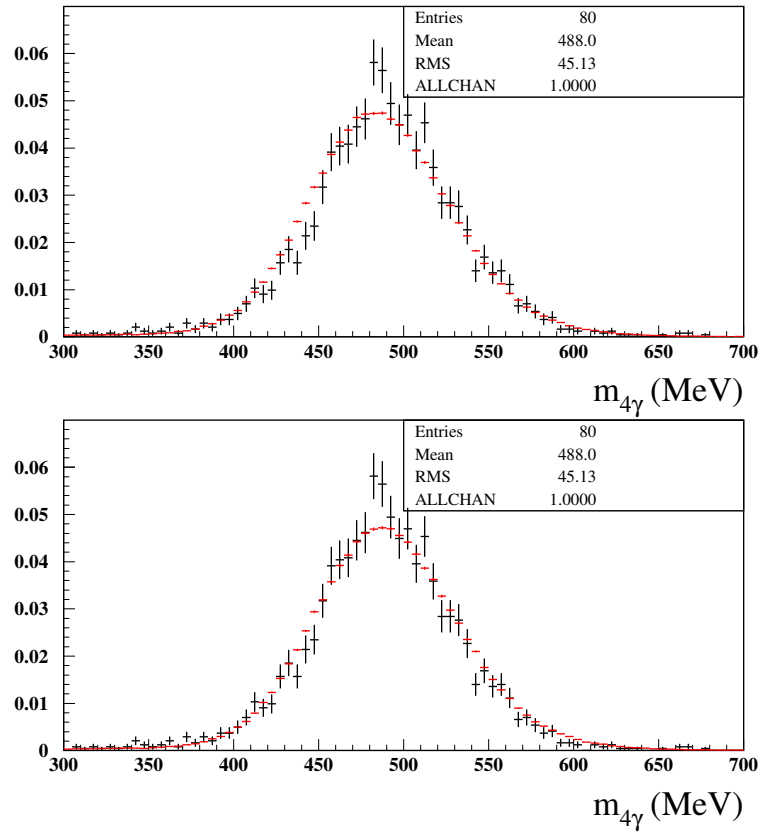


Figure 5.6: Distributions in $m_{4\gamma}$ for data (points with error bars) and $K_S K_L$ MC (solid red line), both selected with cuts 1-3; in the top panel no correction is applied to MC events, in the bottom panel a 8% energy rescaling is applied.

5.2.2 Cross Section at $\sqrt{s} = 1$ GeV

In this case one is interested in properly evaluating data yields and MC efficiency. The selection strategy is inspired by the principle of cutting on “safe ” variables, avoiding selections involving variables for which data and MC are not in good agreement which could introduce large systematic errors. This is the reason why the K_S tagging procedure has not been used here, as K_L interactions in the calorimeter could be simulated not correctly in the MC. The chosen analysis strategy is the following: a kinematic fit asking for four prompt photons to reconstruct the K_S mass and the missing mass to be equal to K_L mass is performed. The following cuts are then applied to both data and MC sample:

1. at least four prompt clusters in the electromagnetic calorimeter;
2. momentum of the 4γ from $\pi^0\pi^0$ decays has to be $20 < p < 80$ MeV;
3. a cut on the χ^2 of the kinematic fit is applied, $\chi_{kin}^2 < 3$ (distributions in χ_{kin}^2 for data and $K_S K_L$ Monte Carlo are shown in Fig. 5.7, left panel).

In order to minimize systematic errors due to erroneous detection simulation no further cuts are applied on variables such as track multiplicity, being inclusive in all K_L decays. This choice, which could affect the sample purity, is compensated by a strict cut on the χ_{kin}^2 of the kinematic fit: as shown in Fig.5.7, right panel, contribution from background processes such as $e^+e^- \rightarrow \eta\gamma$ or $e^+e^- \rightarrow \omega\pi^0$ is negligible in the $\chi_{kin}^2 < 3$ region. Data-MC comparison in χ_{kin}^2 is shown in Fig. 5.8, left; agreement holds up to $\chi^2 \simeq 3$.

Fig. 5.8 (right) shows the remarkable data-MC agreement in the variable $m_{4\gamma}$ after selections 1-4. The selected data sample consists in 16006 events, while the MC-evaluated efficiency is $\epsilon = 0.0502$.

Main uncertainties are due to background rejection, for which the cut on the χ_{kin}^2 variable is crucial. An estimation of this systematic has been done moving the cut at the values $\chi_{kin}^2 < 2$ and $\chi_{kin}^2 < 4$. Results are listed in Tab. 5.4.

	data	ϵ (from MC)	σ (pb)
$\chi_{kin}^2 < 2$	10023	0.0317	1303
$\chi_{kin}^2 < 3$	16006	0.0502	1313
$\chi_{kin}^2 < 4$	20922	0.0648	1331

Table 5.4: Data yields, MC-evaluated efficiencies and cross section estimates for different values of the cut on χ_{kin}^2 .

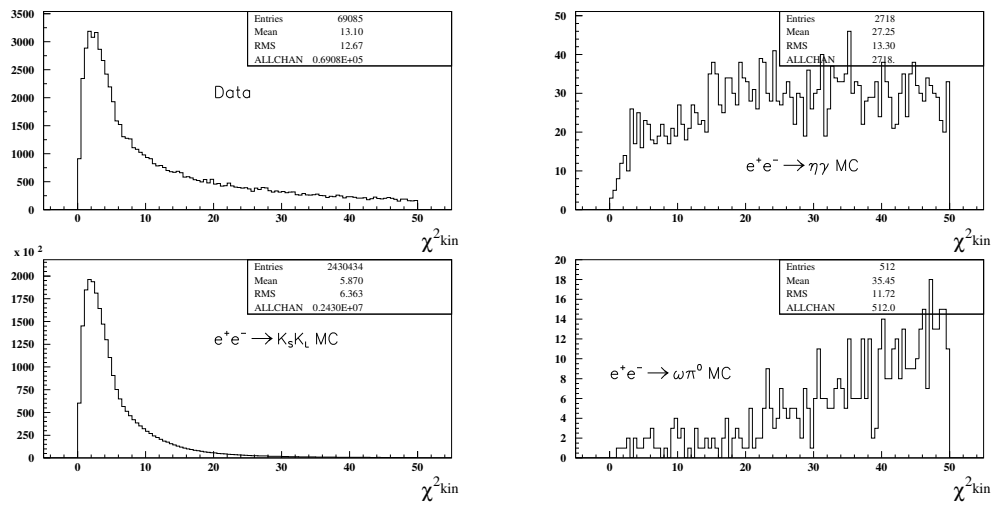


Figure 5.7: Distributions of χ^2_{kin} after cuts 1-2 for data and $e^+e^- \rightarrow K_S K_L$ MC events (left). For comparison, in the right panel χ^2_{kin} distributions are shown for other processes ($e^+e^- \rightarrow \eta\gamma$ and $e^+e^- \rightarrow \omega\pi^0$) which are responsible for the high values tail.

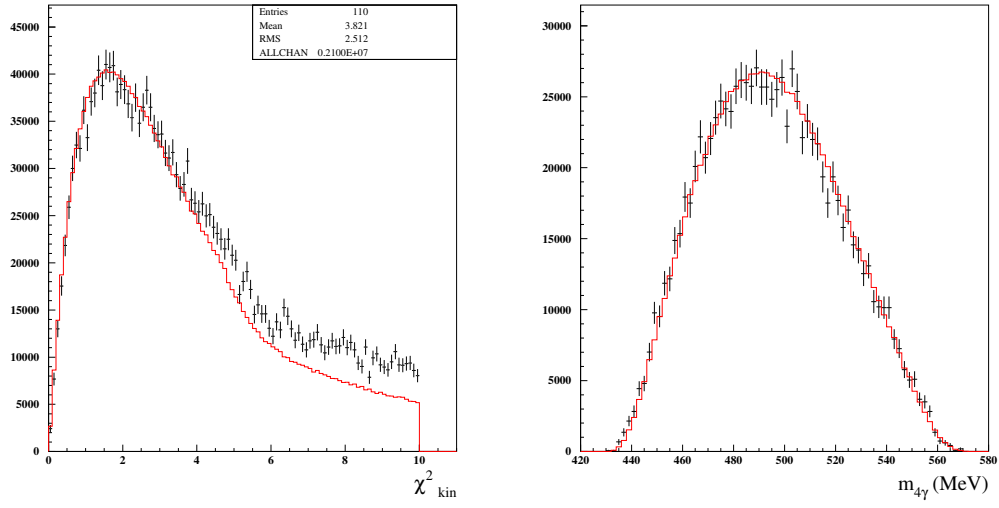


Figure 5.8: Left: Distributions of χ_{kin}^2 after cuts 1-2 for data (points with error bars) and $e^+e^- \rightarrow K_S K_L$ MC events (solid red line), normalized at the distribution peak; data-MC agreement holds up to $\chi_{kin}^2 \simeq 3$. Right, same graphics code: data-MC comparison in $m_{4\gamma}$, after applying cuts 1,2 and $\chi_{kin}^2 < 3$.

The cross section estimate results

$$\sigma_{e^+e^- \rightarrow K_S K_L}(\sqrt{s} = 1 \text{ GeV}) = \frac{n_{data}}{\epsilon} \frac{1}{\mathcal{L}} = (1313 \pm 10_{\text{stat}} \pm 18_{\text{syst}}) \text{ pb}, \quad (5.9)$$

where $\mathcal{L} = 242.5 \text{ pb}^{-1}$ is the integrated luminosity of the data sample. In (5.9) systematic error has been evaluated considering variations on the estimate when moving the cut value on χ_{kin}^2 as shown in Tab. 5.4.

5.2.3 Studies on late clusters

$e^+e^- \rightarrow K_S K_L$ is the only background for $e^+e^- \rightarrow e^+e^-\pi^0\pi^0$ in which a large amount of non prompt energy is released in the calorimeter, due to K_L decays. One can take advantage of this feature in selecting (or rejecting) this class of events. As will be shown in §6.4.4, rejection of events with delayed clusters is applied in the $e^+e^- \rightarrow e^+e^-\pi^0\pi^0$ analysis in order to reduce $K_S K_L$ background. It is therefore crucial to study data-MC agreement in the “ K_L sector”, that is check Monte Carlo simulation of the K_L interactions and releases of energy in the calorimeter.

Cluster times distributions have been studied, considering only clusters with $E > 15 \text{ MeV}$ in order not to take in account accidentals and/or machine background clusters. Comparison has been made between $K_S K_L$ sample selected from data as in §5.2.2 and Monte Carlo events; in both samples the track veto has been applied as one is interested in energy deposits not associated to tracks. As shown in Fig.5.9 (left), MC reproduces the prompt peak at $\simeq 10 \text{ ns}$ and the exponential fall with slope $-1/\tau$, $\tau \simeq 51 \text{ ns}$ (in the $10 \div 50 \text{ ns}$ interval) quite well. In the $50 \div 120 \text{ ns}$ interval, where the bump due to K_L crash is, data-MC agreement is somewhat poor. Moreover, no data is present above 120 ns , while a huge tail in MC goes on up to unphysical values around 300 ns .

According to these observations late clusters (due to both K_L decays in the drift chamber volume and K_L crashes) have been defined as clusters with

- $|t - r/c| > 5\sigma_t$, $7 < t < 120 \text{ ns}$;
- $E > 15 \text{ MeV}$;
- angular acceptance $\theta < 23^\circ$.

As data-MC discrepancy mostly happens to be in the K_L crash time window, multiplicity for crash candidates clusters has been examined first. Data-MC comparison

in n_{crash} is shown in Fig.5.9: the ratio $(n_{crash} > 0)/n_{tot}$ is 0.0758 from data sample and 0.1588 for MC sample, which leads to the correction factor

$$\frac{((n_{crash} > 0)/n_{tot})_{data}}{((n_{crash} > 0)/n_{tot})_{MC}} = 0.477. \quad (5.10)$$

Correction has been applied to late clusters counting in MC by a hit-or-miss method: according to the value $\frac{((n_{crash} > 0)/n_{tot})_{data}}{((n_{crash} > 0)/n_{tot})_{MC}} \simeq 50\%$ of K_L crash events have been removed from the late cluster multiplicity spectrum; the correspondent clusters have been removed from the cluster times distribution. Results are presented in Fig.5.10, 5.11, showing remarkable data-MC agreement, in particular in the cluster times spectrum.

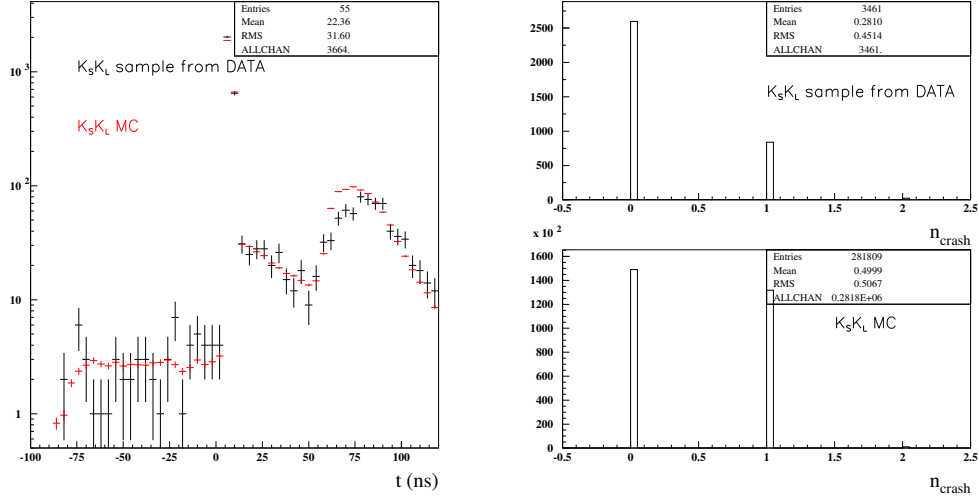


Figure 5.9: Left: cluster times distribution for $K_S K_L$ sample selected from data as described in §5.2.2 and MC sample, with track veto applied; only clusters with $E > 15$ MeV are considered. Right: data (top) and MC (bottom) comparison for K_L crash cluster multiplicity.

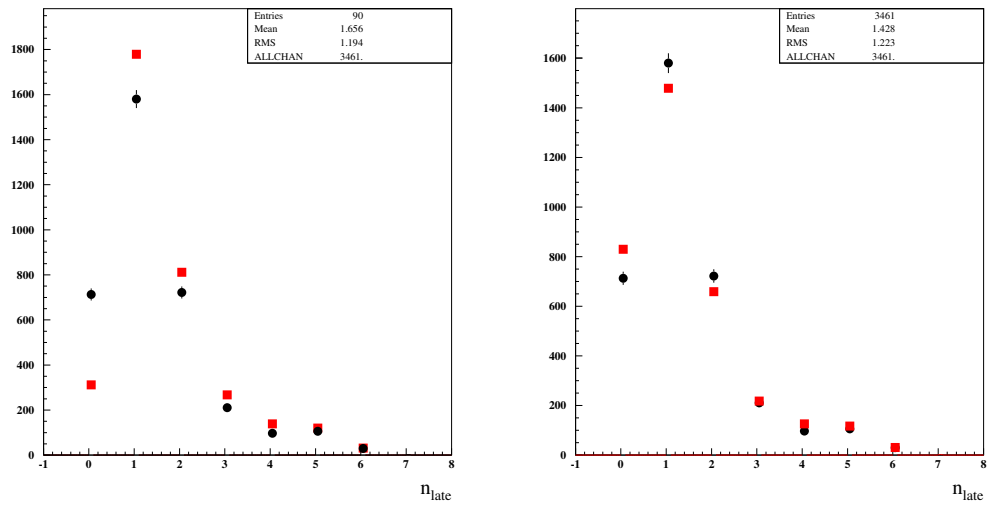


Figure 5.10: Late cluster multiplicities for $K_S K_L$ sample selected from data as described in 5.2.2 (black points) and MC sample (red squares). On the right a correction by hit-or-miss procedure is applied.

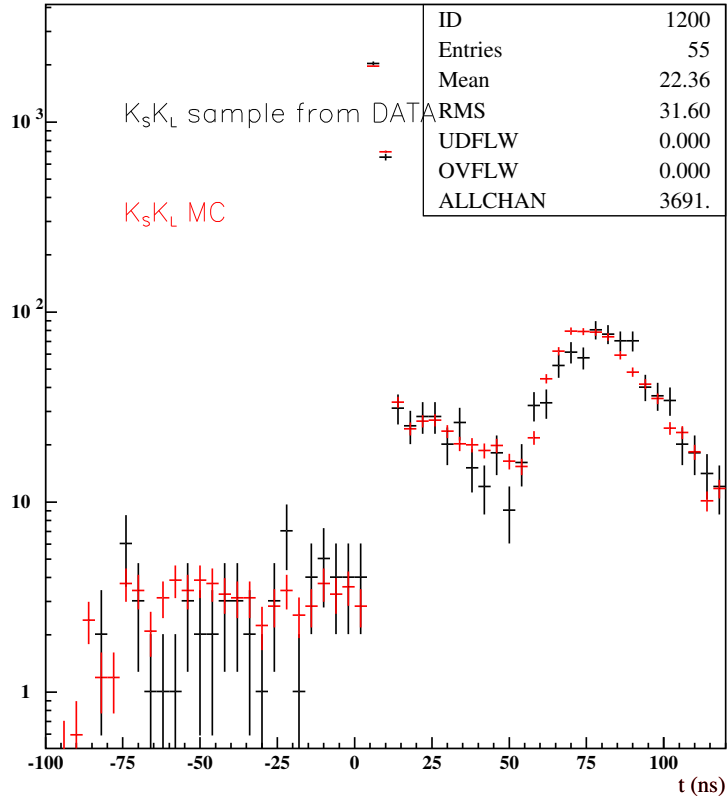


Figure 5.11: Cluster times distribution for $K_S K_L$ sample selected from data as described in 5.2.2 and MC sample, the latter being corrected in late clusters counting by a hit-or-miss procedure; only clusters with $E > 15$ MeV are considered.

5.3 $e^+e^- \rightarrow \eta\gamma$

This process is a background for $e^+e^- \rightarrow e^+e^-\pi^0\pi^0$ when the η meson decays in 3 neutral pions (BR \simeq 32.5%) if 3 photons are not detected. The cross section has been measured by KLOE [19]:

$$\sigma_{e^+e^- \rightarrow \eta\gamma}(\sqrt{s} = 1 \text{ GeV}) = (856 \pm 8_{\text{stat}} \pm 16_{\text{syst}}). \quad (5.11)$$

Cross section (5.11), rescaled by $\text{BR}(\eta \rightarrow \pi^0\pi^0\pi^0)$, is used to normalize the $\eta\gamma$ MC simulation in the $e^+e^- \rightarrow e^+e^-\pi^0\pi^0$ analysis. A sample of 6293520 events has been employed.

$e^+e^- \rightarrow \eta\gamma$ events are used here to check the data-MC agreement in the low $m_{4\gamma}$ range and in the m_{π^0} ($m_{\gamma\gamma}$) spectrum: $m_{4\gamma}$ is the invariant mass of 4 out of the 6 prompt photons in the produced in the process which reconstruct $2\pi^0$ mass, selected as described in §5.2.1; $m_{\gamma\gamma}$ is the invariant mass of the photons coming from one of the pions. Selection has been done applying the following cuts:

1. six prompt clusters in the calorimeter;
2. no late clusters;
3. no tracks in the drift chamber;
4. $m_{4\gamma} > 240$ MeV.

Distributions in $m_{4\gamma}$ and in $m_{\gamma\gamma}$ for data and $\eta\gamma$ MC are shown in Fig. 5.12. Quite good agreement is observed.

5.3.1 Dedicated analysis for $e^+e^- \rightarrow \eta\gamma$

A further, more rigorous analysis has been carried on to study $e^+e^- \rightarrow \eta\gamma$ looking at the “natural ” variable m_η , that is the invariant mass of the six photons from the $\eta \rightarrow \pi^0\pi^0\pi^0$ decay. A kinematic fit has been performed asking for six prompt photons to reconstruct the η meson mass and to recoil against a 350 MeV monochromatic photon. The selected six photons are paired with the same criteria explained in §5.2.1. The following selections are then applied:

1. at least six prompt clusters are requested in the calorimeter;
2. no tracks in the drift chamber;

3. a cut on the pairing χ^2 is applied, $\chi_{6\gamma}^2 < 14$;
4. a cut on the kinematic fit chi-squared is applied, $\chi_{kin}^2 < 20$.

Spectra in $m_{6\gamma}$ and $m_{\gamma\gamma}$ obtained with these selections for data and $\eta\gamma$ MC are shown in Fig. 5.13.

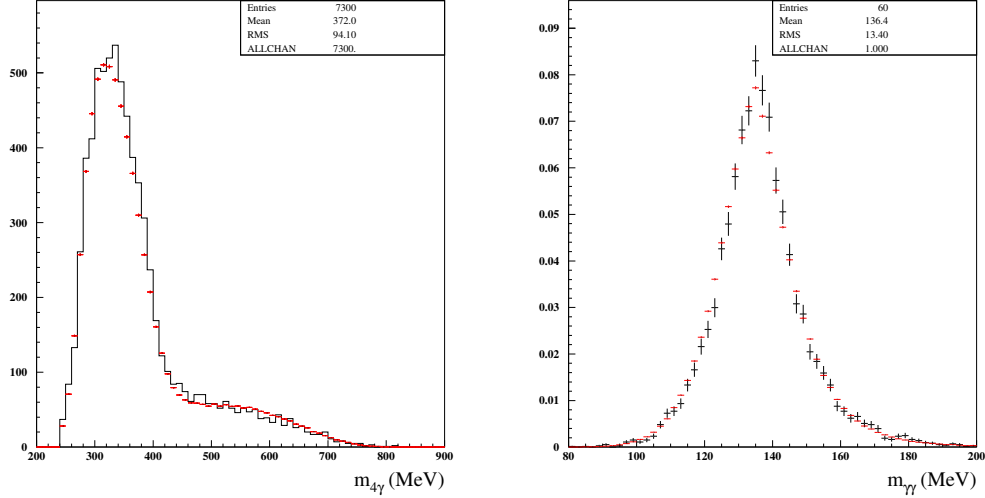


Figure 5.12: Left: invariant mass of 4 out of the 6 photons from $3\pi^0$ decays, paired in order to reconstruct $2\pi^0$ best as described in §5.2.1, for $\eta\gamma$ sample selected from data (black) and $\eta\gamma$ Monte Carlo sample (red), applying cuts 1-4 described in §5.3. Right, same samples and same color code: invariant mass of two photons from one of the $3\pi^0$.

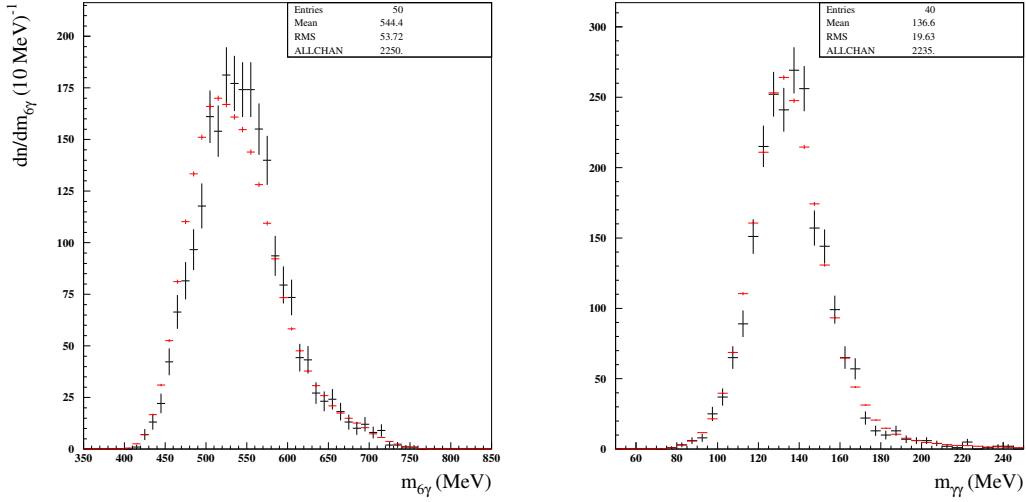


Figure 5.13: Left: invariant mass of 6 photons from η decay obtained applying cuts 1-4 in §5.3.1, for data and $\eta\gamma$ MC (black and red points, respectively). Right, same samples and colour code: invariant mass of 2 photons from π^0 decay, for data and $\eta\gamma$ MC.

5.4 $e^+e^- \rightarrow \omega\pi^0, \omega \rightarrow \pi^0\gamma$

In this process at $\sqrt{s} = 1$ GeV ω ($m_\omega = 78265$ MeV) and π^0 are produced back-to-back with momentum $p = 152$ MeV each. The photon from ω decay, which is monochromatic with $E_\gamma = 379$ MeV in the ω rest frame, gets a range of values $312 \div 459$ MeV whether the photon is collinear or anti-collinear with the ω line of flight. In any case, this photon is by no means the most energetic photon in the event and could be used as a tag. Cross section for $e^+e^- \rightarrow \pi^0\pi^0\gamma$ at $\sqrt{s} = 1$ GeV has been measured by SND [20] and KLOE [21]; KLOE has studied $e^+e^- \rightarrow \omega\pi^0$ specifically, quoting the cross section $\sigma(e^+e^- \rightarrow \omega\pi^0, \sqrt{s} = 1 \text{ GeV}) = 0.55$ nb, with a 1% accuracy.

The sample used in the analysis consists in 914472 generated events.

Selection to study this process is performed finding a prompt cluster with $312 < E < 459$ MeV and two more clusters with $m_{\gamma\gamma} \simeq m_{\pi^0}$; this is done performing a

pairing as in the K_S and η case, considering a χ^2 like variable

$$\chi_{\gamma\gamma}^2 = \frac{(m_{\pi^0} - m_{ij})^2}{\sigma_{ij}^2}, \quad (5.12)$$

rejecting events with $\chi_{\gamma\gamma}^2 > 4$. The three selected photons are constrained to reconstruct the ω mass (782.65 MeV), and to recoil against a π^0 with momentum $p = 152$ MeV performing a kinematic fit; a cut on the resulting χ^2 is applied, $\chi_{kin}^2 < 5$. Invariant mass of the two paired photons is asked to be $115 < m_{\gamma\gamma} < 155$ MeV; events with tracks in the drift chamber and late clusters in the calorimeter are rejected. Data-MC comparison in the $m_{3\gamma}$, that is the invariant mass of the three photons from ω decay, is shown in Fig.5.14.

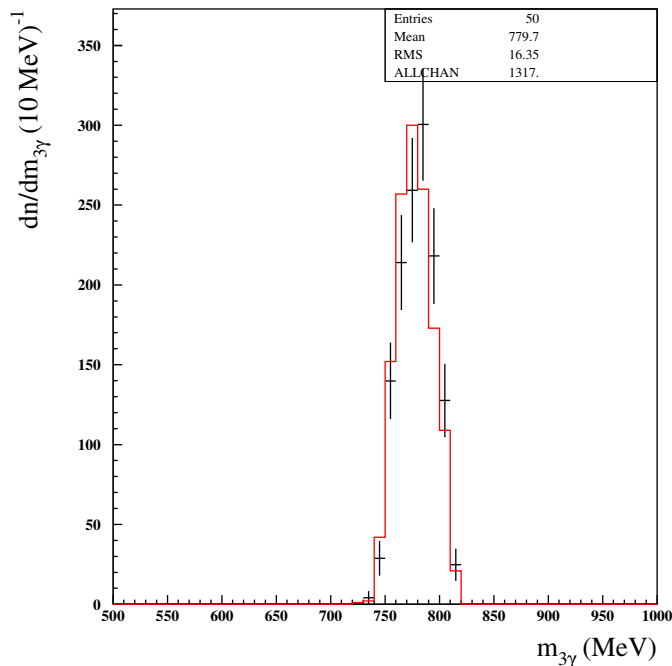


Figure 5.14: Invariant mass of 3 photons from $\omega \rightarrow \pi^0\gamma$ for data (points with error bars) and $e^+e^- \rightarrow \omega\pi^0$ Monte Carlo (red solid line).

5.5 Minor processes

In this section processes are described whose contributions in the $e^+e^- \rightarrow e^+e^-\pi^0\pi^0$ analysis are considered negligible because of the smallness of their cross sections or because they are highly suppressed by analysis cuts.

5.5.1 $e^+e^- \rightarrow \phi \rightarrow f_0\gamma, f_0a_0\gamma$

Scalar mesons $f_0(980)$ and $a_0(980)$ have the following decay modes which represent background to $\pi^0\pi^0$ signal:

- $f_0 \rightarrow 2\pi^0$, BR \simeq 33%;
- $a_0 \rightarrow \eta\pi^0$, BR \simeq 100%.

Cross sections are not well known at $\sqrt{s} = 1$ GeV; $e^+e^- \rightarrow f_0\gamma$ cross section can be estimated from $e^+e^- \rightarrow \pi^0\pi^0\gamma$ measurement (SND, CLEO) by subtracting the known $\omega\pi^0$ production contribution. Cross section is assumed of the order of 20 pb.

Considering the ϕ radiative decays branching ratios

$$\text{BR}(\phi \rightarrow f_0\gamma) = 3.22 \times 10^{-4},$$

$$\text{BR}(\phi \rightarrow a_0\gamma) = 7.6 \times 10^{-5},$$

one gets $\text{BR}(\phi \rightarrow a_0\gamma)/\text{BR}(\phi \rightarrow f_0\gamma) \simeq 0.23$ and can assume the cross section for the $e^+e^- \rightarrow a_0\gamma$ process of the order of 5 pb.

Monte Carlo productions employed in the analysis consists in 129115 $f_0\gamma$ events and 97205 $a_0\gamma$ events.

5.5.2 $e^+e^- \rightarrow \gamma\gamma$

This process, with two photons only in the final state, can contribute as background to the 4γ spectrum when *cluster splitting* occurs (§3.3.1). Even if splitting probability was small, $e^+e^- \rightarrow \gamma\gamma$ would sensibly contribute to the background because of its large cross section, evaluated by QED calculation of the order 10^2 nb. Monte Carlo production used in the analysis consists in $\simeq 1.92 \cdot 10^8$ events.

Chapter 6

Analysis

Signature for $e^+e^- \rightarrow e^+e^-\pi^0\pi^0$, with untagged leptons in the final state, consists in 4 clusters in the electromagnetic calorimeter, coming from the interaction point and satisfying photons space-time relations. The natural variable to look at for searching a signal for this process is the $\pi^0\pi^0$ invariant mass, that is the invariant mass of the 4 photons from $2\pi^0$ decays. Selecting events with 4 clusters in the calorimeter makes cluster counting crucial and a dedicated study has been performed in order to handle it properly (§6.1).

The analysis is divided into two main steps: in the first one, a traditional cut-based approach is followed in order to reject physical background processes and isolate the signal. As after applying analysis cuts the data sample is still contaminated by machine background, a multivariate technique is used as a second step to disentangle it from e^+e^- annihilation and $\gamma\gamma$ processes. A special effort has been requested to characterize the pathological background, selecting it directly from data and then using it in the training for the multivariate analysis (MVA) as a “data driven” simulation.

Monte Carlo simulation for the $e^+e^- \rightarrow e^+e^-\pi^0\pi^0$ process has been described in §5.1. The subset defined by $\vartheta_{pos} < 15^\circ$, $\vartheta_{ele} > 165^\circ$ has been chosen, being $\theta \simeq 15^\circ$ the maximum polar angle for electron and positron to escape detection in KLOE detector, realizing the “tagging by absence” condition (see §2.2).

6.1 Cluster counting and recover splitting

A photon releases energy in the electromagnetic calorimeter firing one or more cells. Starting from cells time and position information are used to reconstruct a *cluster* according to the clustering algorithm described in §3.3. In this analysis, *prompt*

clusters features are the following:

- space-time relation: $|t - r/c| < 5 \sigma_t$, σ_t defined as in Eq.(3.3);
- energy: $E > 15$ MeV;
- angular acceptance: $23^\circ < \vartheta < 157^\circ$.

Cluster splitting occurs when a single photon energy deposit is reconstructed as more than one cluster, and is responsible for an erroneous cluster multiplicity evaluation. A *recover splitting* procedure is applied in order to heal this pathology.

An overall procedure, according to KLOE standard clustering algorithm, is applied to all clusters; two clusters are merged one with the other if the following conditions are satisfied:

- the least energetic cluster of the pair has $E < 100$ MeV;
- the distance between the two clusters is

$$\Delta R = \sqrt{(x_1 - x_2)^2 + (y_1 - y_2)^2 + (z_1 - z_2)^2} < \frac{6 \text{ cm}}{\sqrt{E(\text{GeV})}},$$

- the time distance is $\Delta t = t_1 - t_2 < 3.5$ ns;
- if the two clusters are both on the barrel or on the same endcap, both the transverse and the longitudinal (with respect to the fiber direction) separations have to be $\Delta_L, \Delta_T < \frac{6 \text{ cm}}{\sqrt{E(\text{GeV})}}$.

Energy of the resulting cluster is obtained as the sum of the energies of the original clusters, while position and time coordinates are obtained as energy-weighted sums.

A further recover splitting procedure is applied to *prompt* clusters at a second stage, as described in the following section.

6.1.1 Cluster counting

The process $e^+e^- \rightarrow K_S K_L$, $K_S \rightarrow \pi^0 \pi^0$ has the same photon multiplicity of the signal; it has been therefore chosen as a check process to verify data-MC agreement. A $e^+e^- \rightarrow K_S K_L$, $K_S \rightarrow \pi^0 \pi^0$ control sample has been selected applying the following selections:

- no tracks are asked to be in the drift chamber;

- at least one “ K_L crash” cluster candidate in the electromagnetic calorimeter, where the “ K_L crash” cluster candidate is defined as a cluster *in the barrel* with $E > 100$ MeV and $0.092 < \beta^* < 0.105$.

The control sample has been used to study the effect of the recover splitting procedure on prompt clusters and to check data-MC agreement for photon multiplicity. In Fig. 6.1 scatter plots in the variables ΔR_{min} and E_{min} are shown for $K_S K_L$ events with 5 prompt clusters (simulated events in the top panel, selected from data in the bottom panel). The 5th prompt photon in $K_S K_L$, $K_S \rightarrow \pi^0 \pi^0$ events can arise as an accidental cluster (low energy, flat ΔR_{min} distribution) or as a splitted cluster (low energy and small ΔR_{min} values). The recover splitting procedure in the $\Delta R_{min} < 70$ cm, $E_{min} < 50$ MeV region is aimed to heal this pathology.

Prompt clusters multiplicity for the control data sample and for $K_S K_L$ MC simulation is shown in Fig. 6.2, before and after the recover splitting procedure on prompt clusters. A slightly better data-MC agreement and a decrease of events with 5 photons is observed.

This recover splitting procedure, tested on $e^+ e^- \rightarrow K_S K_L$ events, has been applied to all background processes and to data sample.

6.2 Preselections

Trigger, Background rejection filter and $\gamma\gamma$ filter have been described in §4.1-4.3. 1345214 data events, out of a radiative stream of $\simeq 3.76 \times 10^8$ events, pass these preselections. Numbers of generated and selected events, with correspondent reduction factors, are listed in Tables 6.1, 6.2 for background processes Monte Carlo samples.

$e^+ e^- \rightarrow$	$K_S K_L$	$\eta\gamma$	$\omega\pi^0$
Generated	19571400	6293520	914472
Preselections (ϵ)	3479996 (0.1778)	1747458 (0.2776)	153716 (0.1681)

Table 6.1: Number of generated events and number of events selected by trigger, background rejection filter and $\gamma\gamma$ filter, for $K_S K_L$, $\eta\gamma$ and $\omega\pi^0$ Monte Carlo samples. Preselections efficiencies are quoted in brackets.

Preselection efficiency on $e^+ e^- \rightarrow e^+ e^- \pi^0 \pi^0$ events has been studied as a function of the $\pi^0 \pi^0$ invariant mass, taking in account resolution effects on reconstructing $m_{2\pi^0}$ in order to parametrize $\epsilon(m_{2\pi^0})$ near and below $\pi^0 \pi^0$ production threshold: the procedure is described in the following sections.

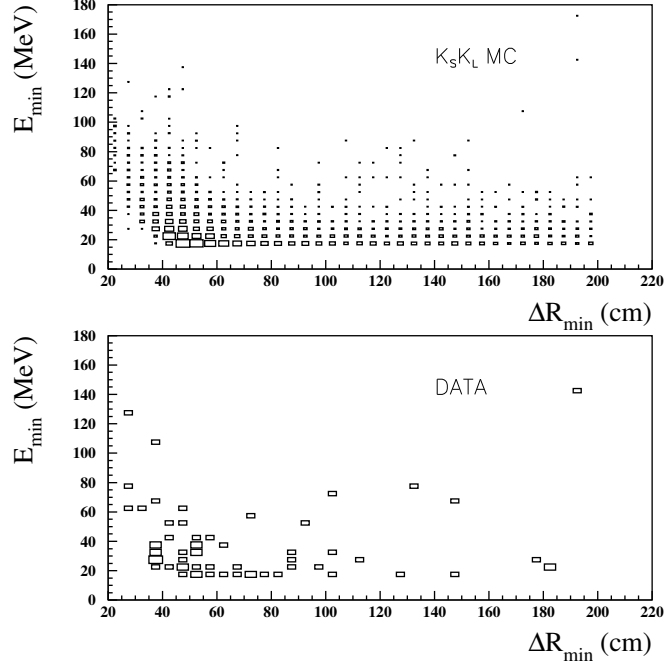


Figure 6.1: Scatter plots in the variables ΔR_{min} and E_{min} for $K_S K_L$ events with 5 prompt photons: simulated MC events (top) and selected from data (bottom).

$e^+e^- \rightarrow$	$f_0\gamma$	$a_0\gamma$	$\gamma\gamma$
Generated	129115	97205	$1.92 \cdot 10^8$
Preselections (ϵ)	21086 (0.1633)	23590 (2427)	91296 ($4.75 \cdot 10^{-4}$)

Table 6.2: Number of generated events and number of events selected by trigger, background rejection filter and $\gamma\gamma$ filter, for $f_0\gamma$, $a_0\gamma$ and $\gamma\gamma$ Monte Carlo samples. Preselections efficiencies are quoted in brackets.

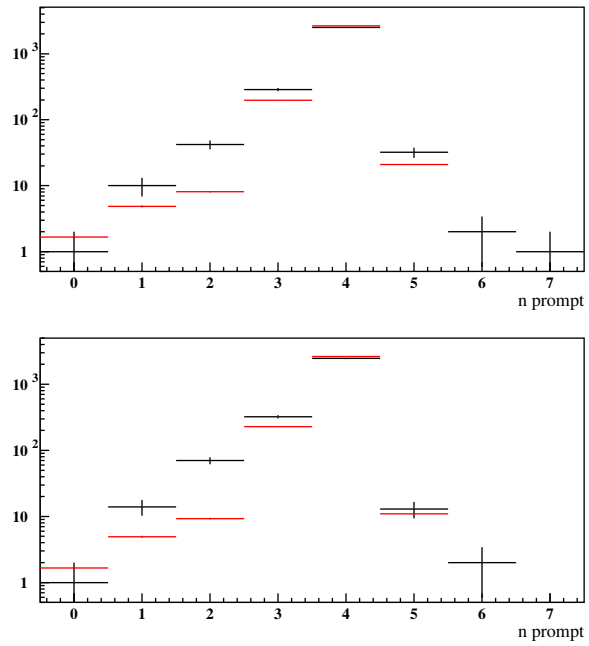


Figure 6.2: Prompt clusters multiplicity for $K_S K_L$ events before (top) and after (bottom) recover splitting procedure. Black points are data, red points are $K_S K_L$ MC (distributions normalized to the same data number of events).

6.3 Two π^0 signature, $m_{4\gamma}$ reconstruction

For events which pass preselection filters and with at least 4 prompt clusters the invariant mass of 4 photons from $2\pi^0$ decays is reconstructed performing a pairing as described for the $K_S K_L$, $K_S \rightarrow \pi^0 \pi^0$ process in §5.2.1. Connection between the reconstructed variable $m_{4\gamma}$ and the generated one $m_{2\pi^0}$ has been studied in order to parametrize the detection resolution function and evaluate preselection filters efficiencies on signal $e^+e^- \rightarrow e^+e^-\pi^0\pi^0$ events.

6.3.1 Resolution function

Four photons invariant mass resolution is defined as

$$Res(m_{2\pi^0}) = \frac{\sqrt{E[(m_{4\gamma} - m_{2\pi^0})^2]}}{m_{2\pi^0}}, \quad (6.1)$$

where $E(x)$ stands for expected value of x . After pairing and reconstruction, $e^+e^- \rightarrow e^+e^-\pi^0\pi^0$ MC events have been used to obtain 6.1, considering the scatter plot $(m_{4\gamma} - m_{2\pi^0})$ vs $m_{2\pi^0}$ (Fig. 6.3). Eighty 10-MeV-slices in $m_{2\pi^0}$ have been considered, and for each bin in abscissa the $m_{4\gamma} - m_{2\pi^0}$ has been fitted with a gaussian curve, verifying that $RMS \simeq \sigma$. Resolution function values have been therefore obtained as

$$Res_i = \frac{RMS_i}{m_{2\pi_i^0}}, \quad (6.2)$$

where i is the abscissa bin index; assuming gaussian fluctuations, errors have been evaluated for each bin as $\frac{Res_i}{\sqrt{2n_i}}$, n_i being the number of events in the i -th bin. Values have been plotted as functions of $m_{2\pi^0}$ and fitted with the function

$$f(x) = \frac{A}{\sqrt{x}} \oplus \frac{B}{x} \oplus C, \quad (6.3)$$

that is the sum of a sampling, a noise and a signal uniformity error. Fit returns $A = 0.05473, B = 0.01033, C = 0.001019$, with $\chi^2/n_{dof} = 31.90/30$ (Fig. 6.4).

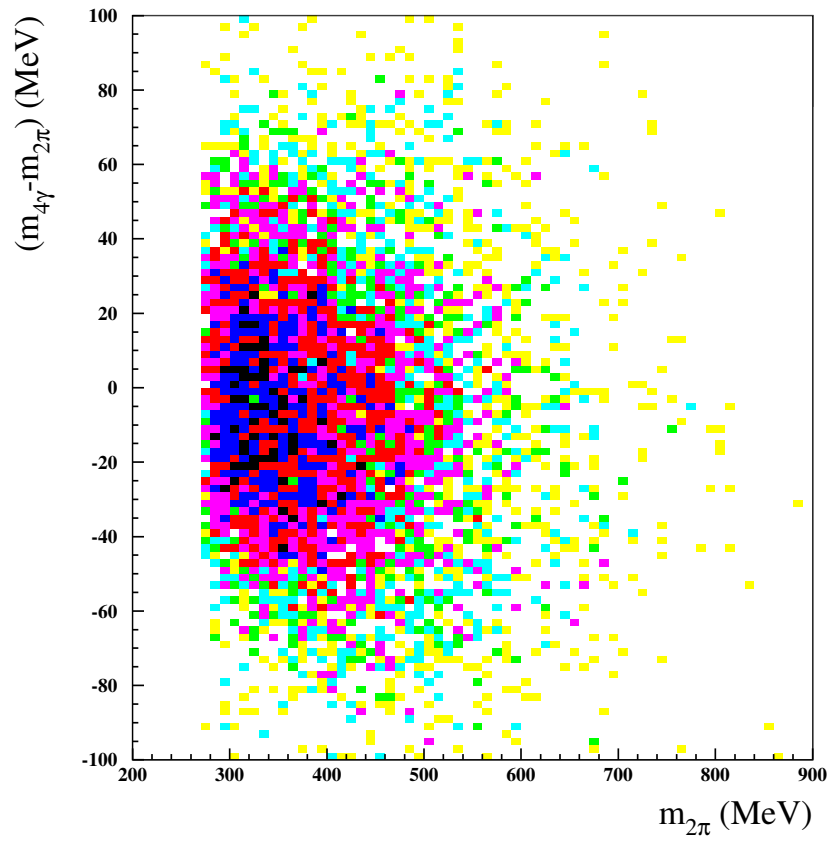


Figure 6.3: 2D histogram in the variables $m_{2\pi^0}$ (abscissa) and $m_{4\gamma} - m_{2\pi^0}$ (ordinates) after 4 photons reconstruction.

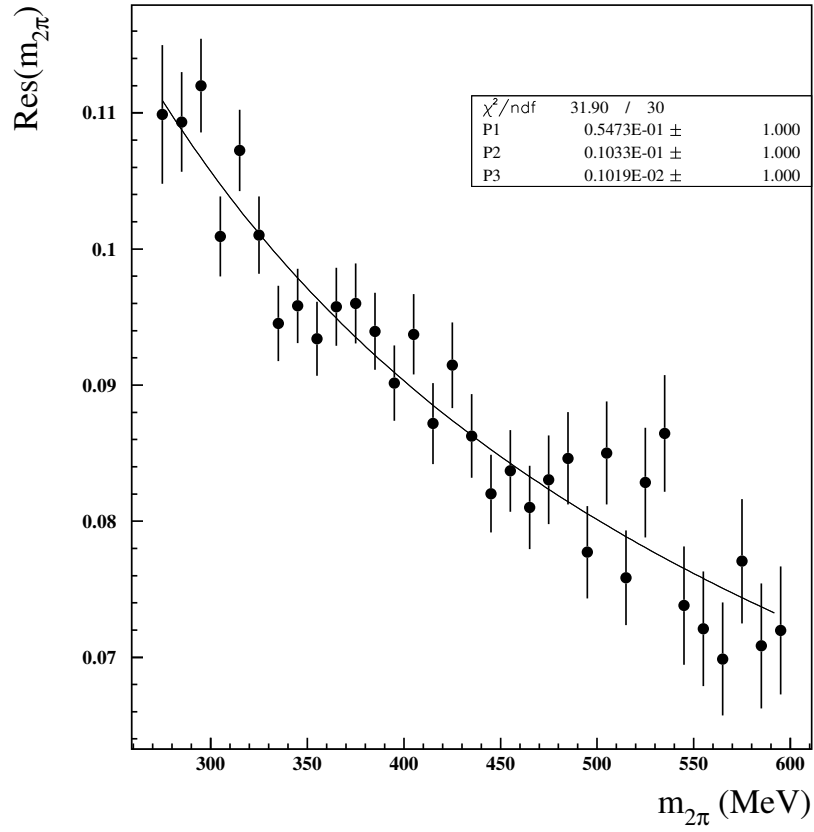


Figure 6.4: Resolution function $Res = Res(m_{2\pi})$.

Gaussian smearing

To relate the $m_{4\gamma}$ distribution to the $m_{2\pi^0}$ distribution a convolution problem has to be faced. Let's set for simplicity of notation $m_{4\gamma} = y$ and $m_{2\pi^0} = x$. If $f(x)$ is the distribution function for the x variable and $g(y)$ describes how y values fluctuate around x one is interested in the convolution product

$$(f \otimes g)(y) = \int dx f(x)g(y - x); \quad (6.4)$$

in Eq.(6.4) $g(y-x)$ plays the role of a resolution function; $(f \otimes g)(y)$ is the distribution function for y given the distribution for x and the resolution. In the limit of infinite resolution, $g(y - x) \rightarrow \delta(y - x)$ and one obtains

$$(f \otimes g)(y) = \int dx f(x)\delta(y - x) = f(y), \quad (6.5)$$

and the distribution in the variable y is identical to the distribution in x .

Practically, a gaussian smearing is performed acting on the event x variable giving to it a shift by an amount δ randomly extracted according to a normal distribution of variance σ . In the specific case, $\sigma = \sigma(x) = Res(x)$, with $Res(x)$ defined as in (6.1) and parametrized as in (6.3).

$$y = x(1 + \delta \times \sigma(x)). \quad (6.6)$$

Smearing matrix

Another way of relating $m_{4\gamma}$ and $m_{2\pi^0}$ spectra consists in acting on the distribution rather than on the event, applying to the counts spectrum a matrix which describes events migration from a bin of the starting distribution to a bin of the final distribution (folding procedure). Let n_i^x , $i = 1, \dots, N$ be a vector of events distributed in the variable $m_{2\pi^0}$; the i -th element in this vector is the number of events in the bin i -th of the correspondent N bin histogram. The smearing matrix is defined as the matrix S_{ij} that

$$n_i^y = \sum_{j=1}^N S_{ij}n_j^x, \quad (6.7)$$

where n_i^y is the vector of the same events distributed in $m_{4\gamma}$. S_{ij} can be built considering the MC events scatter plot $m_{4\gamma}$ vs $m_{2\pi^0}$, just after 4 photons invariant mass reconstruction; this scatter plot for $e^+e^- \rightarrow e^+e^-\pi^0\pi^0$ MC events is shown in Fig.6.5, with a 70×70 binning on the $200 \div 900$ MeV invariant mass interval for both

variables. In the 2d-histogram, for each (i, j) cell M_{ij} is number of events which, in the $x \rightarrow y$ transition, migrate from bin j of the x distribution to bin i of the y distribution; fixing the row index i the sum over all columns gives the number of events in the i -th bin of the y distribution:

$$n_i^y = \sum_{j=1}^N M_{ij}; \quad (6.8)$$

comparison between Eq.(6.7) and Eq.(6.8) gives

$$S_{ij} = \frac{M_{ij}}{n_j^x}. \quad (6.9)$$

The interpretation of Eq.(6.9) is straightforward: smearing matrix elements S_{ij} represent the migration probability from the j -th bin of x distribution to the i -th bin of y distribution, normalized to the number of events in the j -th bin of x distribution.

Fig. 6.6 shows signal MC events distributed in the generated $m_{2\pi^0}$ variable (black) and in the variable $m_{2\pi^0}^{sm}$ obtained applying a gaussian smearing to $m_{2\pi^0}$, as described above. The spectrum obtained by folding the $m_{2\pi^0}$ distribution through application of the smearing matrix is also shown.

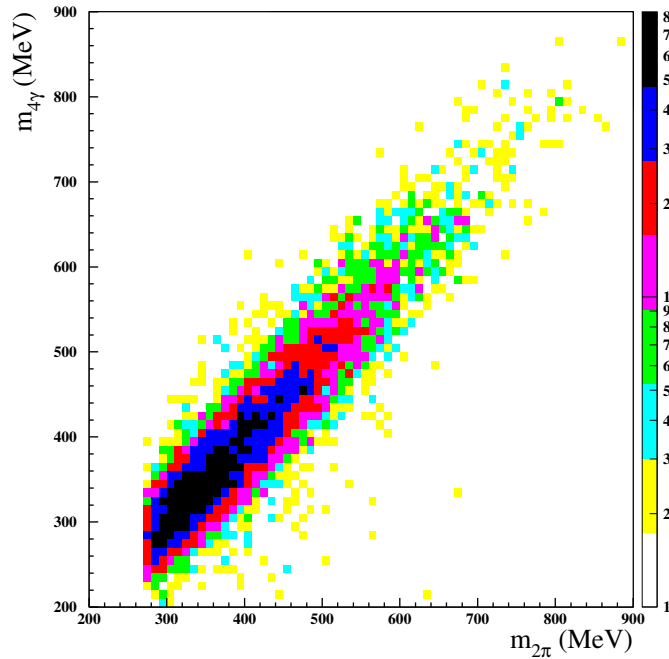


Figure 6.5: Scatter plot in $m_{2\pi^0}$ and $m_{4\gamma}$ of $e^+e^- \rightarrow e^+e^-\pi^0\pi^0$ MC events after preselection and reconstruction. Note the $m_{4\gamma}$ distribution with non empty bins below $\pi^0\pi^0$ production threshold, due to resolution effects, while the distribution in generated $\pi^0\pi^0$ invariant mass correctly starts from $m_{2\pi^0} = 2m_\pi \simeq 270$ MeV.

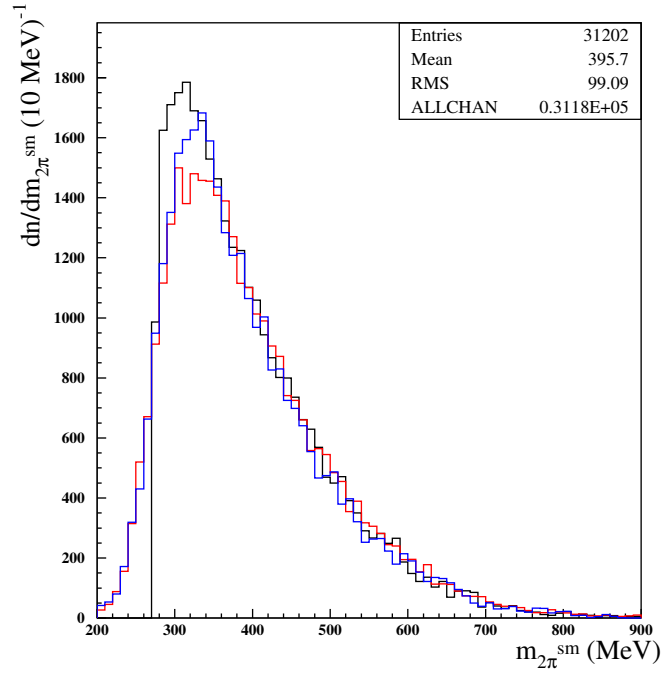


Figure 6.6: Generated $e^+e^- \rightarrow e^+e^-\pi^0\pi^0$ events distributed in the generated variable $m_{2\pi^0}$ (black) and in the variable obtained by applying gaussian smearing (red); the blue distribution is obtained applying the smearing matrix to the $m_{2\pi^0}$ spectrum. Both folded spectra are no empty below $\pi^0\pi^0$ production threshold.

Preselections and reconstruction efficiencies as functions of $m_{2\pi^0}$

As reconstruction follows preselection, the variable $m_{4\gamma}$ is not available to study efficiencies of trigger, background rejection filter and $\gamma\gamma$ filter as functions of the final state invariant mass. The variable $m_{2\pi^0}^{sm}$ obtained applying gaussian smearing to the generated $2\pi^0$ invariant mass has been used to this scope. Each selection efficiency as a function of $m_{2\pi^0}^{sm}$ has been evaluated as

$$\epsilon_i^{sel} = \frac{N_i^{sel}}{D_i} = \frac{n^o \text{ of selected events in the bin } i}{n^o \text{ of generated events in the bin } i}, \quad (6.10)$$

employing 10-MeV binning. Trigger and background rejection filter efficiency curves are shown in Fig. 6.7; in Fig. 6.8 $\gamma\gamma$ filter and all preselections efficiencies are shown. Here and in all efficiency evaluation statistical errors have been evaluated bin-per-bin according to binomial statistics,

$$\delta\epsilon_i = \sqrt{\frac{\epsilon_i(1 - \epsilon_i)}{D_i}}.$$

Reconstruction procedure introduces the request of having at least 4 photons in the event. Because of the angular distribution of photons produced in the reaction $e^+e^- \rightarrow e^+e^-\pi^0\pi^0$, a non negligible fraction of signal events has one or more photons out of the acceptance, resulting in a $\simeq 48\%$ inefficiency. The efficiency of this request factorize with previous filters efficiencies: total preselections + reconstruction efficiency is shown in Fig. 6.9, top panel. As at this stage $m_{4\gamma}$ variable has been built, one can evaluate ϵ using both $m_{2\pi^0}^{sm}$ and $m_{4\gamma}$ distributions. In Fig. 6.9, bottom panel, efficiency curve obtained $m_{2\pi^0}^{sm}$ distributions is shown together with that obtained using $m_{4\gamma}$ distribution for N_i , while D_i is given by applying the smearing matrix to the “bare” $m_{2\pi^0}$ spectrum.

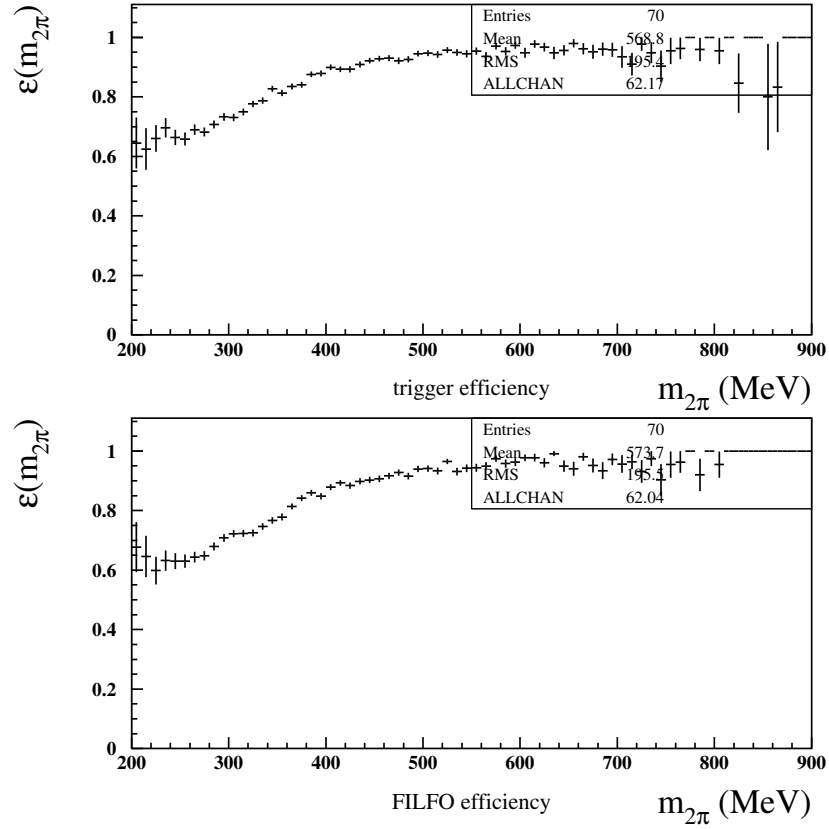


Figure 6.7: Trigger (top) and background rejection filter (bottom) efficiency on $e^+e^- \rightarrow e^+e^-\pi^0\pi^0$ Monte Carlo events, as a function of the variable $m_{2\pi^0}$. Gaussian smearing has been applied in order to take in account detection resolution effects.

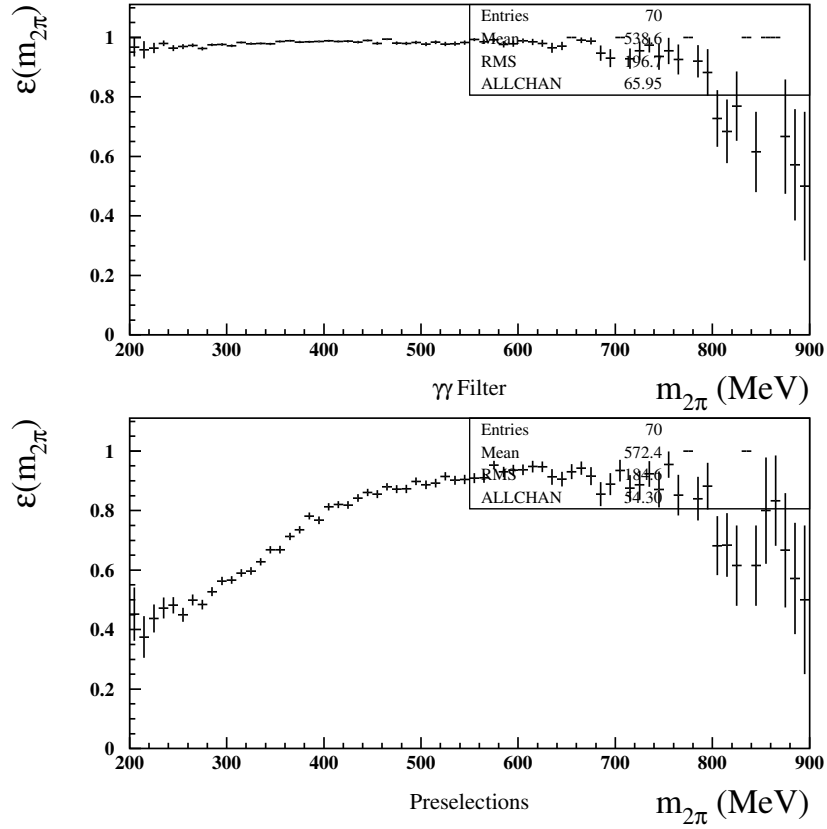


Figure 6.8: $\gamma\gamma$ filter (top) and total preselection (bottom) efficiency on $e^+e^- \rightarrow e^+e^-\pi^0\pi^0$ Monte Carlo events, as a function of the variable $m_{2\pi^0}$. Gaussian smearing has been applied in order to take in account detection resolution effects.

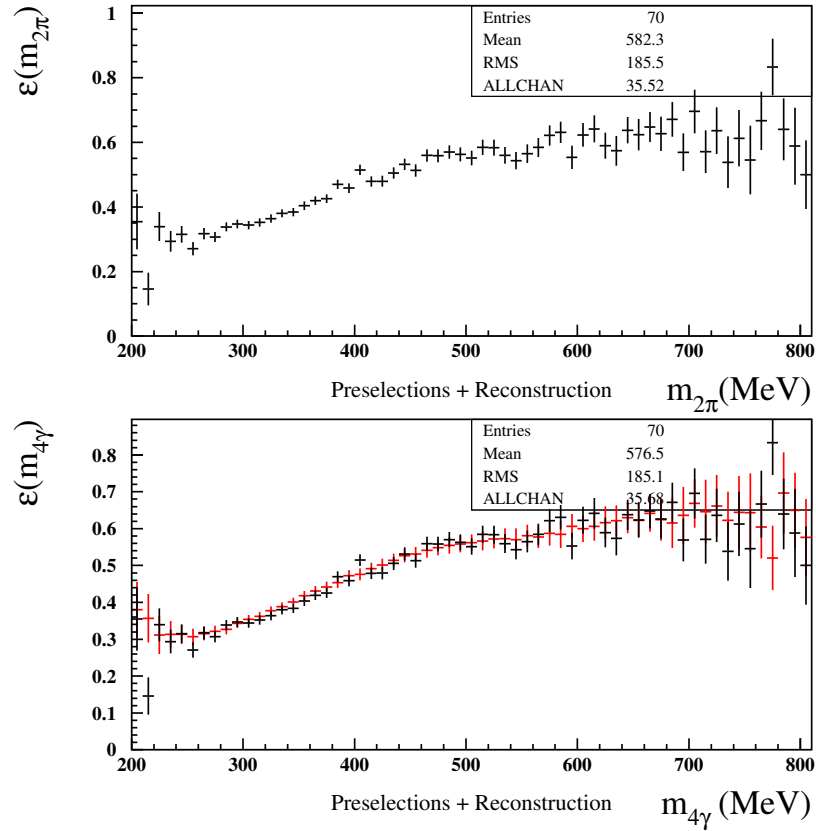


Figure 6.9: Top: efficiencies of all preselection filters and reconstruction procedure as function of the variable $m_{2\pi^0}$. Gaussian smearing has been applied in order to take in account detection resolution effects. Bottom: black curve is the same as the one in the top panel; the red curve is obtained using reconstructed $m_{4\gamma}$ distribution for numerator and distribution obtained applying the smearing matrix to the $m_{2\pi^0}$ spectrum for denominator.

6.4 Cut-based analysis

Selections applied in order to reject e^+e^- annihilation processes are presented in §6.4.2-6.4.5. Selections efficiencies on the signal have been studied as functions of the products invariant mass, as shown in §6.4.6.

6.4.1 Track veto

Events with tracks in the drift chamber are rejected. This selection not only rejects important background processes such as $e^+e^- \rightarrow K_S K_L$, $K_L \rightarrow \pi^+\pi^-\pi^0$, but also works as “antitagging” condition selecting $e^+e^- \rightarrow e^+e^-\pi^0\pi^0$ events with quasi real scattering photons.

It is crucial to study efficiency of this selection on $e^+e^- \rightarrow K_S K_L$: for this process, as $\chi_{\pi\pi}^2 < 4$ request selects $K_S \rightarrow \pi^0\pi^0$ events (see following paragraph, §6.4.2), tracks are mainly due to charged (both semileptonic and hadronic) K_L decays. Presence of tracks in the drift chamber is therefore closely related to K_L interactions in the calorimeter, and wrongly simulated detector response in the Monte Carlo could strongly affect efficiency estimate. As shown in §5.2.3, a data-MC comparison shows an excess of K_L crash events in the Monte Carlo; one would think this excess to be associated to an excess of events with no tracks¹. This expectation is confirmed by Fig. 6.10, where $e^+e^- \rightarrow K_S K_L$ sample selected from data and $K_S K_L$ MC are compared looking at tracks multiplicity. A clear excess of events with no tracks is seen in MC with respect to data.

As track veto and rejection of events with late clusters happen to be intimately correlated in reducing $K_S K_L$ population, their combined effect is studied in §6.4.4 and a correction factor to their efficiency on $K_S K_L$ is introduced.

¹In §5.2.3 a correction procedure has been described to heal the K_L crash events excess; this procedure does not have effects on tracks multiplicity.

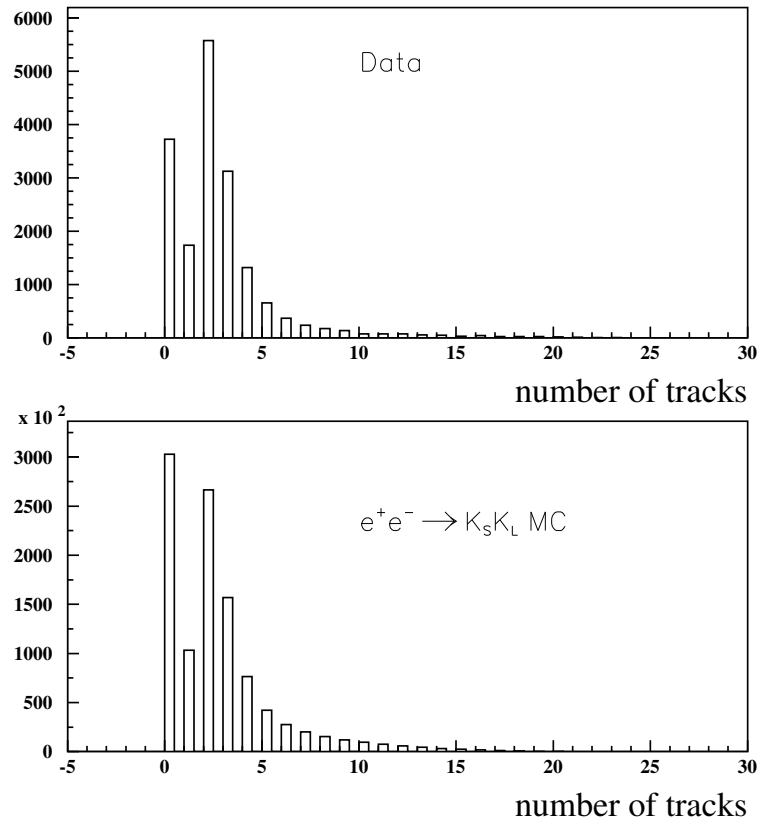


Figure 6.10: Tracks multiplicity for $e^+e^- \rightarrow K_S K_L$ events selected from data (selections as in §5.2.2) and $K_S K_L$ Monte Carlo events. An excess of events with no tracks is observed in the MC.

6.4.2 Cut on $\chi^2_{\pi\pi}$

Distributions in the variable $\chi^2_{\pi\pi}$ are shown in Fig.6.11 for signal MC, data and main background processes; a high-values tail in the data distribution is apparent, due to not genuine $2\pi^0$ events, which are rejected asking $\chi^2_{\pi\pi} < 4$. In Fig. 6.12 the effect of applying this cut on data events is shown: looking at the invariant masses of the two pairs of photons chosen in the pairing procedure, one sees that cutting $\chi^2 < 4$ selects events with both $m_{\gamma\gamma}$ which reconstruct the pion mass well. Cutting on $\chi^2_{\pi\pi}$ also rejects events with low photon multiplicities $n_\gamma < 4$, for which the variable $\chi^2_{\pi\pi}$ is not even defined.

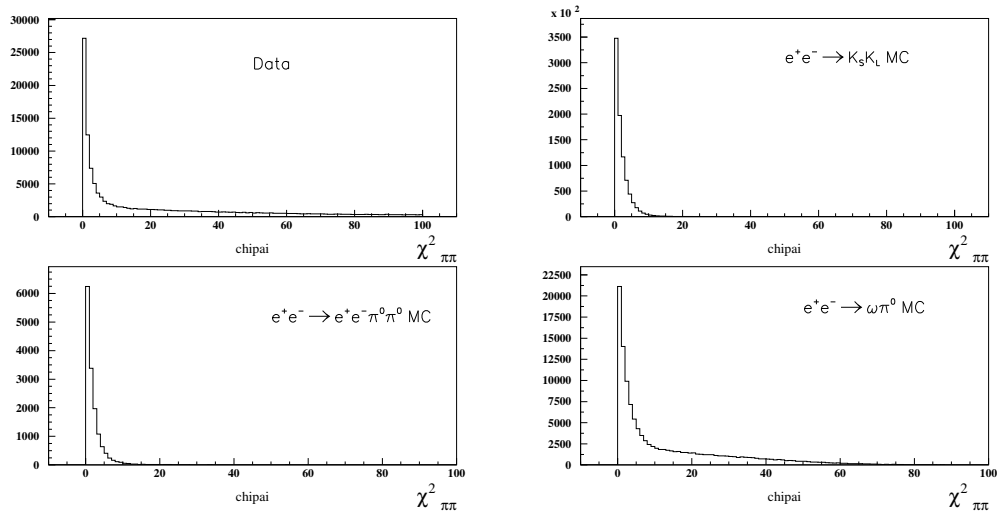


Figure 6.11: Distributions in the variable $\chi^2_{\pi\pi}$ for data, Signal MC and main background processes. Track veto is applied.

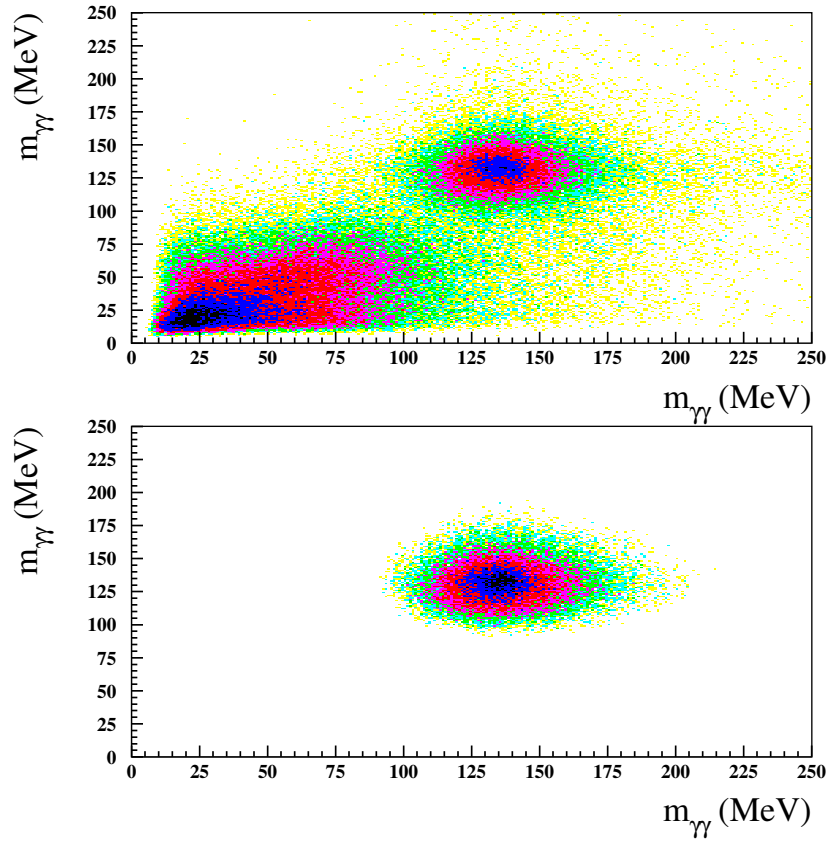


Figure 6.12: Scatter plot in the two photons pairs invariant masses for data, before (top) and after (bottom) applying the cut $\chi^2_{\pi\pi} < 4$. Track veto is applied.

6.4.3 4 γ only

Events with 4 photons (i.e. 4 prompt clusters) are selected. High multiplicity events such as $e^+e^- \rightarrow \eta\gamma$ (7 photons) or $e^+e^- \rightarrow \omega\pi^0$ (5 photons) are hugely reduced by this cut (events with low photon multiplicity $n_\gamma < 4$ have already been rejected by the cut on $\chi_{\pi\pi}^2$).

6.4.4 Rejection of events with late clusters

The main background for the analysis is the process $e^+e^- \rightarrow K_S K_L$, with $K_S \rightarrow \pi^0\pi^0$. Charged K_L decays are rejected thanks to the track veto; neutral K_L decays are rejected asking for no late clusters in the electromagnetic calorimeter, either these clusters are due to $K_L \rightarrow \pi^0\pi^0\pi^0$ or to the so called “ K_L crash”. Late cluster definition has been given in §5.2.3, where a procedure to improve data-MC agreement in late cluster multiplicity has been presented, too. As explained in §6.4.1, rejection of events with late clusters and rejection of events with tracks are closely correlated and it’s worth performing a study of these combined cuts on $K_S K_L$ events. In Tab. 6.3 efficiencies of single track veto, of rejection of late clusters and of combination of these selections are listed: efficiencies are evaluated on samples of $e^+e^- \rightarrow K_S K_L$ events selected as in §5.2.2.

	$K_S K_L$ from data	$K_S K_L$ MC
	16006	983487
no late	1882 (0.1176)	130102 (0.1323)
no tracks	3461 (0.2162)	281809 (0.2865)
no late & no tracks	713 (0.0445)	67557 (0.0687)

Table 6.3: Number of events which pass track veto, no late clusters request and combination of these cuts; correspondent efficiencies are quoted in brackets. Used samples consist in $K_S K_L$ events selected from data and MC as explained in §5.2.2.

From values in Tab. 6.3 it is apparent that for these cuts considered both separately and in cascade efficiency evaluated from MC is overrated. One can get a correction factor for MC evaluated efficiency of (track veto) + (no late clusters) selections,

$$\frac{\epsilon_{data}}{\epsilon_{MC}} = \frac{0.0445}{0.687} = 0.648, \quad (6.11)$$

which has to be taken in account when factorizing $\epsilon^{no\ tracks} \times \epsilon^{no\ late}$ with other cuts efficiencies. Tabs. 6.4 and 6.5 are “efficiencies matrices” in which efficiencies of

cutting on one of the two variables are evaluated respect to the subset obtained cutting on the other variable, for data and MC.

Data	no tracks	no late
no tracks	1	0.3788
no late	0.2060	1

Table 6.4: Efficiencies matrix for cuts “no tracks”, “no late” on data. Table has to be read as follows: first row, second column: efficiency of track veto evaluated on the sample previously selected requiring no late clusters; second row, first column, efficiency of rejecting events with late clusters evaluated on the sample previously selected applying track veto. Diagonal entries are trivial (efficiency of one cut on the sample defined by the cut itself).

MC	no tracks	no late
no tracks	1	0.5192
no late	0.2397	1

Table 6.5: Efficiencies matrix for cuts “no tracks”, “no late” on MC. Table has to be read as follows: first row, second column: efficiency of track veto evaluated on the sample previously selected requiring no late clusters; second row, first column, efficiency of rejecting events with late clusters evaluated on the sample previously selected applying track veto. Diagonal entries are trivial (efficiency of one cut on the sample defined by the cut itself).

It is apparent that main contribution to the ratio $\frac{\epsilon_{data}}{\epsilon_{MC}}$ comes from track veto efficiency:

$$\left(\frac{\epsilon_{data}^{no\ tracks}}{\epsilon_{MC}^{no\ tracks}}\right)_{no\ late} = \frac{0.3788}{0.5192} = 0.7295, \quad \left(\frac{\epsilon_{data}^{no\ late}}{\epsilon_{MC}^{no\ late}}\right)_{no\ tracks} = \frac{0.2060}{0.2397} = 0.8594.$$

where $(\epsilon^x)_y$ is the efficiency of cutting on x on a sample on which cut on y has been already applied.

6.4.5 Cut on photons energy spread

From prompt photons energies the following variables are defined:

$$\langle E \rangle = \frac{1}{N_{prompt}} \sum_i^{N_{prompt}} E_i, \quad E_{RMS} = \sqrt{\langle E^2 \rangle - \langle E \rangle^2}. \quad (6.12)$$

For the process $e^+e^- \rightarrow e^+e^-\pi^0\pi^0$, with both pions decaying in two photons, a little spread in photons energies is expected, as for $K_S \rightarrow \pi^0\pi^0$ decay processes. This is not the case for processes with more involved dynamics, such as $e^+e^- \rightarrow \eta\gamma$ or $e^+e^- \rightarrow \omega\pi^0$; a cut $E_{RMS} < 140$ MeV is applied to reject such processes, as shown in Fig. 6.13.

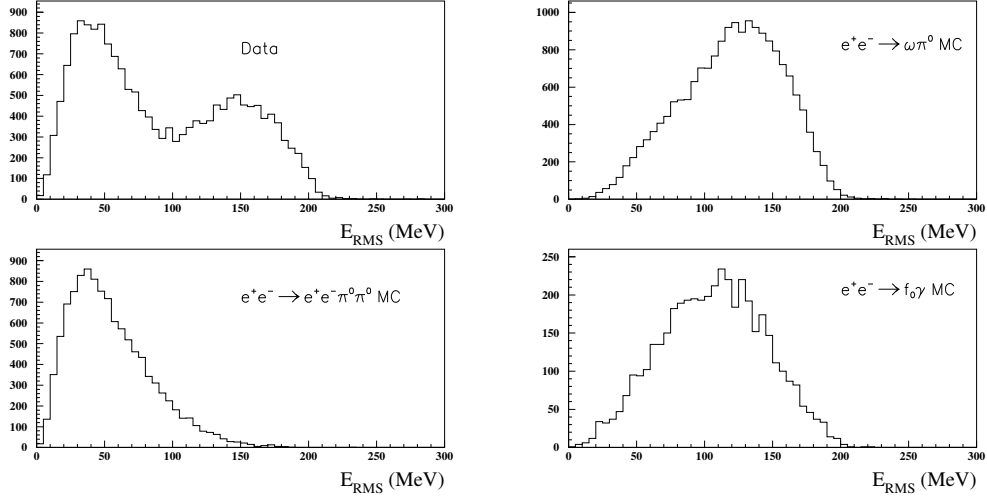


Figure 6.13: Distributions in the variable E_{RMS} for data, Signal MC and main background processes. All previous cuts are applied.

6.4.6 Cuts efficiency on signal as function of $m_{4\gamma}$

As for preselections, efficiencies for analysis cuts on $e^+e^- \rightarrow e^+e^-\pi^0\pi^0$ events cuts have been studied as functions of the final state invariant mass ($m_{4\gamma}$). Efficiencies are referred to reconstruction level, that is distribution in $m_{4\gamma}$ after preselections and reconstruction has been used as denominator distribution.

Efficiencies curves are shown in Figs. 6.14, 6.15.

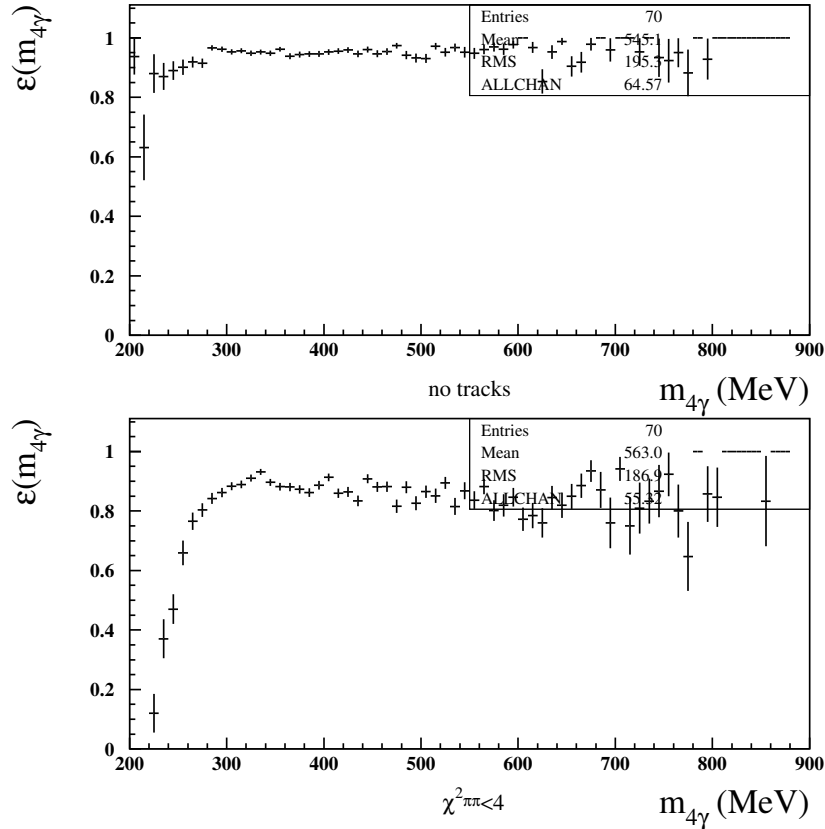


Figure 6.14: Efficiency of track veto (top) and of $\chi^2_{\pi\pi} < 4$ cut as functions of the variable $m_{4\gamma}$.

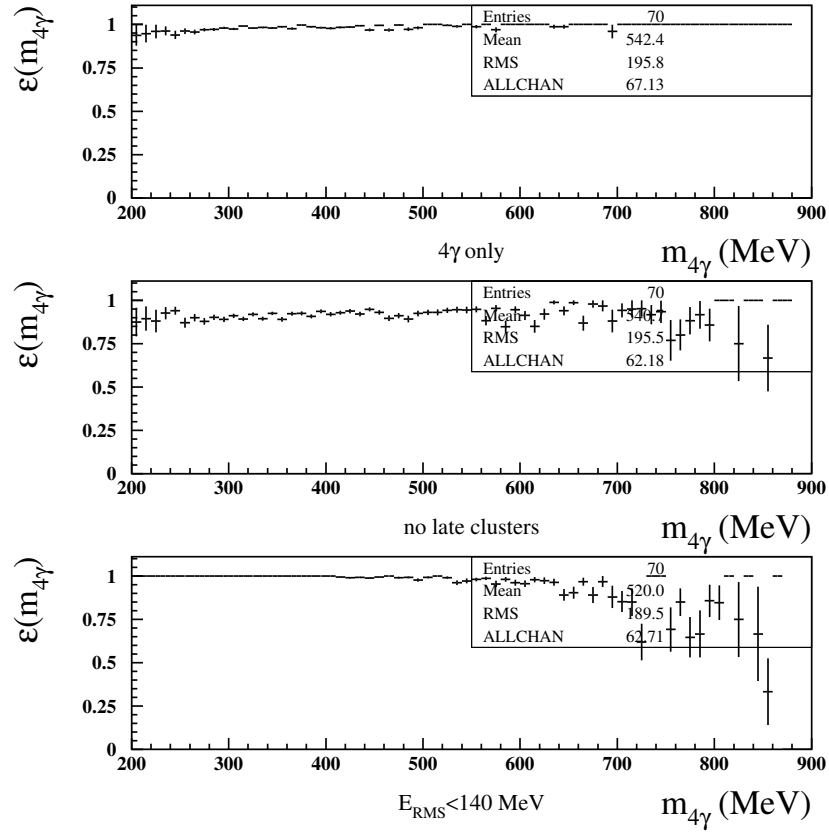


Figure 6.15: Efficiency of $n_\gamma = 4$ (top), $n_{late} = 0$ and of $E_{RMS} < 140$ cut as functions of the variable $m_{4\gamma}$.

6.4.7 Summary of cut-based analysis

In table 6.6 number of data and signal MC events are listed which pass the analysis cuts; in table 6.7 global efficiencies (preselection plus cuts) for physical background processes are reported; absolute numbers of events for these processes are evaluated as the product $\mathcal{L} \times \sigma \times \epsilon$, where $\mathcal{L} = 242.5 \text{ pb}^{-1}$ is the integrated luminosity, σ is the process cross section and ϵ is the efficiency. For $K_S K_L$ a multiplicative correction factor $\epsilon_{data}/\epsilon_{MC} = 0.6477$ has been taken in account.

	data	Signal MC
Radiative stream	3.767×10^8	
Generated ($\vartheta_{pos} < 15^\circ, \vartheta_{ele} > 165^\circ$)		31202
Preselection and Reconstruction	1345214	13862 (0.444)
no tracks	223886	13162 (0.422)
$\chi^2_{\pi\pi} < 4$	52094	11397 (0.365)
4 γ only	32216	11216 (0.359)
no late clusters	18146	10286 (0.329)
$E_{RMS} < 140 \text{ MeV}$	13559	10178 (0.326)

Table 6.6: Number of data and signal MC events after analysis cuts. For signal MC efficiencies are indicated in brackets.

	MC events	$\epsilon (\times 10^3)$	σ (nb)	$n = \mathcal{L}\sigma\epsilon$
$K_S K_L$	168317	5.570	1.313	1773
$\eta\gamma$	38694	6.148	0.284	423
$\omega\pi^0$	12390	13.549	0.55	1807
$f_0\gamma$	3516	27.231	0.017	112
$\gamma\gamma$	748	3.89×10^{-3}	360	340
$a_0\gamma$	636	6.543	0.011	17

Table 6.7: Cuts efficiencies for physical background processes. A 0.648 correction factor has been applied to efficiency for $K_S K_L$ events. In the last column absolute numbers of events are listed.

Fig. 6.16 shows invariant mass distribution for data and background processes (normalized according to efficiencies and cross sections as in table 6.7) after selections; on the right, the subtracted spectrum obtained from data is compared to the signal MC distribution. Analogous distributions are shown in Figures 6.17 and 6.18 for the variables transverse and longitudinal momentum, respectively.

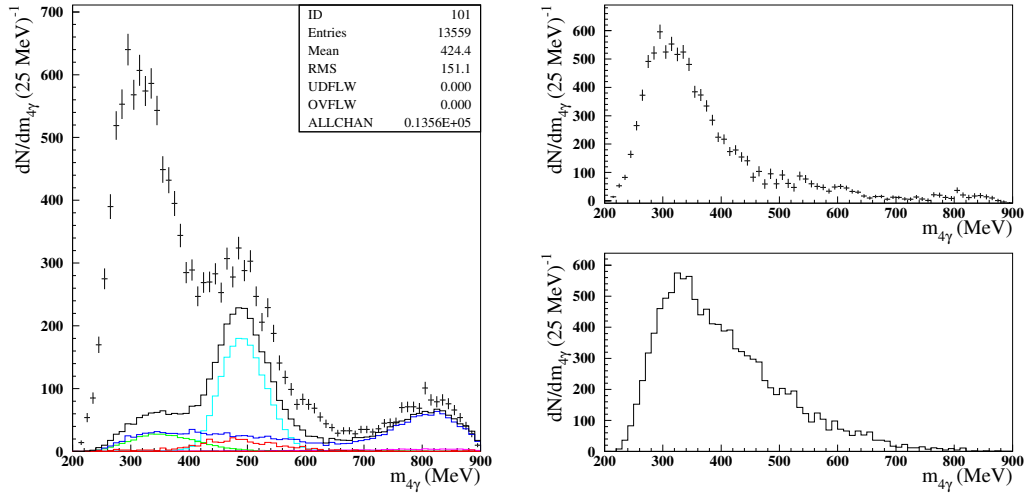


Figure 6.16: Left: spectra in the $m_{4\gamma}$ variable for data (points with statistical error bars) and physical background processes, normalized according to MC-evaluated efficiencies and cross sections as shown in Tab. 6.7. Color code is: light blue = $K_S K_L$, green = $\eta\gamma$, dark blue = $\omega\pi^0$, violet = $f_0\gamma$; the black solid line is the sum of all background contribution. Right: $m_{4\gamma}$ distribution for data after background subtraction (top) and for $e^+e^- \rightarrow e^+e^-\pi^0\pi^0$ MC (bottom).

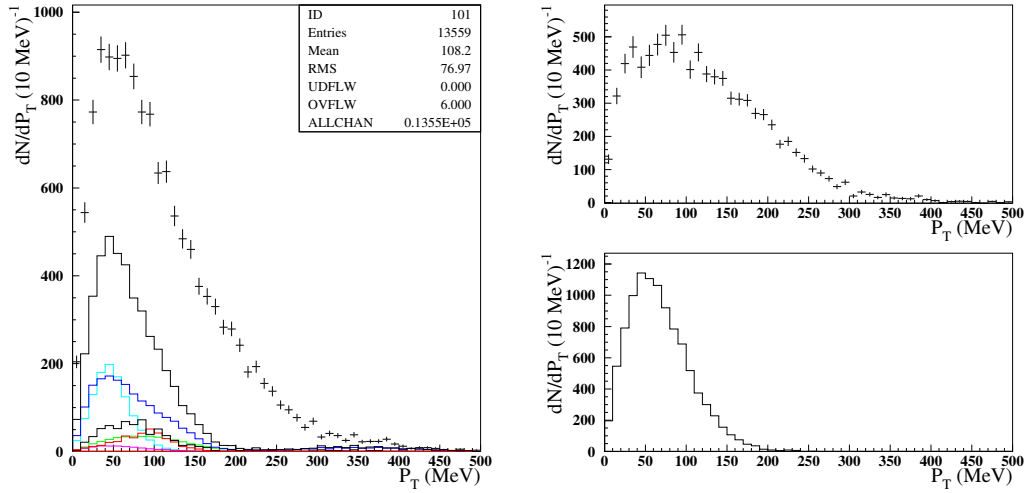


Figure 6.17: Left: spectra in the p_T variable for data (points with statistical error bars) and physical background processes, normalized according to MC-evaluated efficiencies and cross sections as shown in Tab. 6.7. Color code is: light blue = $K_S K_L$, green = $\eta\gamma$, dark blue = $\omega\pi^0$, violet = $f_0\gamma$; the black solid line is the sum of all background contribution. Right: p_T distribution for data after background subtraction (top) and for $e^+e^- \rightarrow e^+e^-\pi^0\pi^0$ MC (bottom).

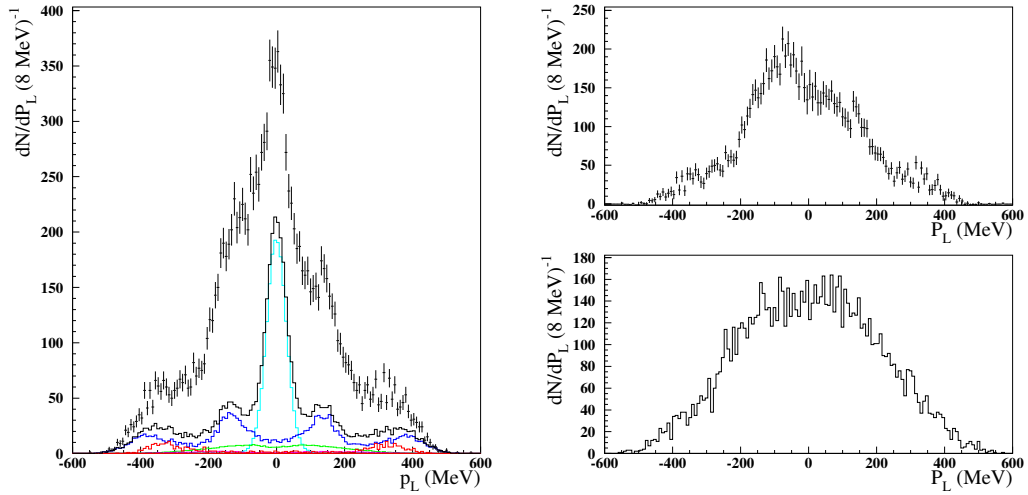


Figure 6.18: Left: spectra in the p_L variable for data (points with statistical error bars) and physical background processes, normalized according to MC-evaluated efficiencies and cross sections as shown in Tab. 6.7. Color code is: light blue = $K_S K_L$, green = $\eta\gamma$, dark blue = $\omega\pi^0$, violet = $f_0\gamma$; the black solid line is the sum of all background contribution. Right: p_L distribution for data after background subtraction (top) and for $e^+e^- \rightarrow e^+e^-\pi^0\pi^0$ MC (bottom).

A further data-MC comparison is performed considering the following variable:

$$\chi_t^2 = \frac{1}{4} \sum_i^4 \left(\frac{t_i - r_i/c}{\sigma_{t,i}} \right)^2, \quad (6.13)$$

which takes in account the overall event promptness. Distributions in χ_t^2 for data, background MC (always normalized as in Tab. 6.7), data after background subtraction and signal MC are shown in Fig. 6.19.

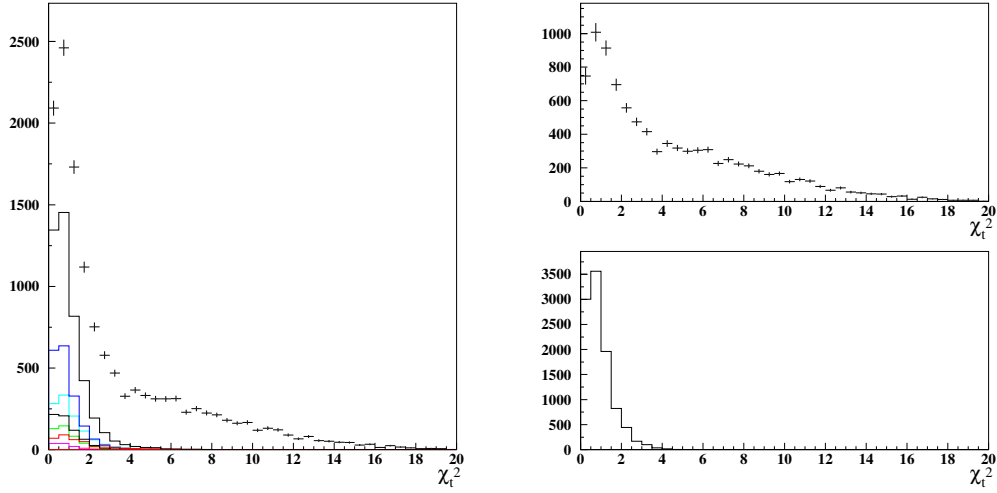


Figure 6.19: Left: spectra in the χ_t^2 variable for data (points with statistical error bars) and physical background processes, normalized according to MC-evaluated efficiencies and cross sections as shown in Tab. 6.7. Color code is: light blue = $K_S K_L$, green = $\eta\gamma$, dark blue = $\omega\pi^0$, violet = $f_0\gamma$; the black solid line is the sum of all background contribution. Right: χ_t^2 distribution for data after background subtraction (top) and for $e^+e^- \rightarrow e^+e^-\pi^0\pi^0$ MC (bottom).

The apparent excess of data in the low invariant mass region seems to be not compatible with the $\gamma\gamma \rightarrow \pi^0\pi^0$ MC prevision. More precisely, data exhibit a huge low invariant mass, high transverse momentum population associated with an unbalanced longitudinal momentum distribution; moreover, these seem to be poorly prompt events as they are associated to the high-values tail in the χ_t^2 distribution. These features, first of all the p_L unbalance and the poor promptness, are hints for

these events to be machine background, namely electro-production of pion(s) from residual gas in the beam pipe. In case of single π^0 electro-production, superposition of such a process and a $\gamma\gamma \rightarrow \pi^0$ reaction could provide the fake $\gamma\gamma \rightarrow \pi^0\pi^0$ event. This kind of background just above $2\pi^0$ threshold has been observed by the Crystal Ball experiment, too.

6.5 Multivariate Analysis

In this section the procedure followed to disentangle the pathologic machine background introduced in the previous section from physical processes is described. Instead of a traditional cut-based approach, a multivariate technique is used. The package which has been employed is the Toolkit for Multivariate Data Analysis (TMVA), integrated into the analysis framework ROOT.

Multivariate classification methods based on machine learning techniques have become a fundamental ingredient to most analyses, being essential to extract a maximum of the available information from the data. They provide a powerful tool to discriminate signal from background considering not single variables but combining several event features, provided as input by the user, and building a classifier output response which describes a decision boundary.

Events in the data sample to be analyzed are classified according to a classification algorithm previously developed using *training* events for which the desired output is known (for example, MC events). In the training phase, the method “learn” how to build the classifier variable as a (linear or non-linear) function of the input variables chosen by the user. Training events are also used to evaluate the classification performance (two orthogonal training events subsets are typically used for the training and the evaluation procedures). Once the method has been trained, it is *applied* on the data set: for each data event a classifier output value is returned, which can be used as a discriminating variable to classify the event as signal or background.

In the following, all physical processes involved in the analysis (both $\gamma\gamma$ and annihilation processes) will be referred to as *signal*; the expression *background* will be reserved for the machine background. Training events are provided by (properly weighted) MC simulations for the signal, while a sample selected directly from data is necessary for the background, as a simulation for electro-production of pions from nuclei is not available. Next section is devoted to describe the background selection from data.

6.5.1 Identification of the machine background

Two variables have been considered to identify background events:

- $|d| = \sqrt{d_1^2 + d_2^2}$, where $d_{1,2}$ are the parameters returned by the minimization of the following χ^2 -like variable:

$$\chi_{d_1, d_2}^2 = \sum_i^2 \left(\frac{r'_i(d_1)/c - t_i}{\sigma_{t,i}} \right)^2 + \sum_j^2 \left(\frac{r'_j(d_2)/c - t_j}{\sigma_{t,j}} \right)^2, \quad (6.14)$$

In Eq. (6.14) i and j are the indices of the photons coming from the pions, paired according to the procedure described in §6.4.2; $r'_i(d_1)$ ($r'_j(d_2)$) are the photons paths to the calorimeter if they are originated from a point along the beam pipe (z axis) shifted by d_1 (d_2) from the interaction point. The distances $r'_{i,j}(d_{1,2})$ can be expressed in terms of the clusters coordinates as

$$r'_{i,j}(d_{1,2}) = \sqrt{r_{i,j}^2 + d_{1,2}^2 + 2d_{1,2}z_{i,j}}, \quad (6.15)$$

where $r_{i,j} = \sqrt{x_{i,j}^2 + y_{i,j}^2 + z_{i,j}^2}$. Obviously, if $d_{1,2} \rightarrow 0$ in Eq.(6.15), then $r'_{i,j} \rightarrow r_{i,j}$ and photons are prompt and come directly from the interaction point.

- $|t - r/c|_{t_0}$, that is the space-time relation of the cluster which provides the t_0 for the event. The t_0 cluster is individuated as the most prompt cluster with energy of at least 50 MeV and distance from the z axis of at least 60 cm; if no cluster in the event satisfy this last condition, only the $E > 50$ MeV condition is required; if neither the $E > 50$ MeV condition is satisfied by one of the clusters, the t_0 cluster is simply defined as the most prompt cluster in the event.

Events for which the minimization of χ_{d_1, d_2}^2 returns non-zero values for d_1 , d_2 or both of them are events with one or both pions which are likely produced at a point shifted from the IP, that is good machine background events candidates. Events with poorly prompt t_0 cluster are good machine background candidates, too, as for these events the t_0 could have been provided by some reaction which is not related to the e^+e^- interaction.

In Fig. 6.20 distributions in the variables $|d|$ and $(t-r/c)_{t_0}$ are shown for data (upper plots) and, for comparison, for $e^+e^- \rightarrow \eta\gamma$ MC events, chosen as representative of prompt processes (bottom). Data exhibit deviations respect to MC simulations, with huge excess of events in the tails of the distributions. These tail populations

($|d| > 33$ cm and $|t - r/c|_{t_0} > 0.5$ ns) have been studied looking at the variables $m_{4\gamma}$, p_T and p_L ; results are shown in Fig. 6.21. Both requests $|d| > 33$ cm and $|t - r/c|_{t_0} > 0.5$ ns select events with the following features:

1. low invariant mass ($m_{4\gamma} < 500$ MeV);
2. p_T distribution up to high values ($\simeq 300$ MeV);
3. unbalanced p_L distribution.

It is again worth stressing that the p_L distribution asymmetry, with excess of events at negative p_L values, is compatible with the interpretation of these events as product of interaction of e^\pm with residual gas in the beam pipe, being the electron beam (coming from the negative z semi-axis) more intense than the positron beam.

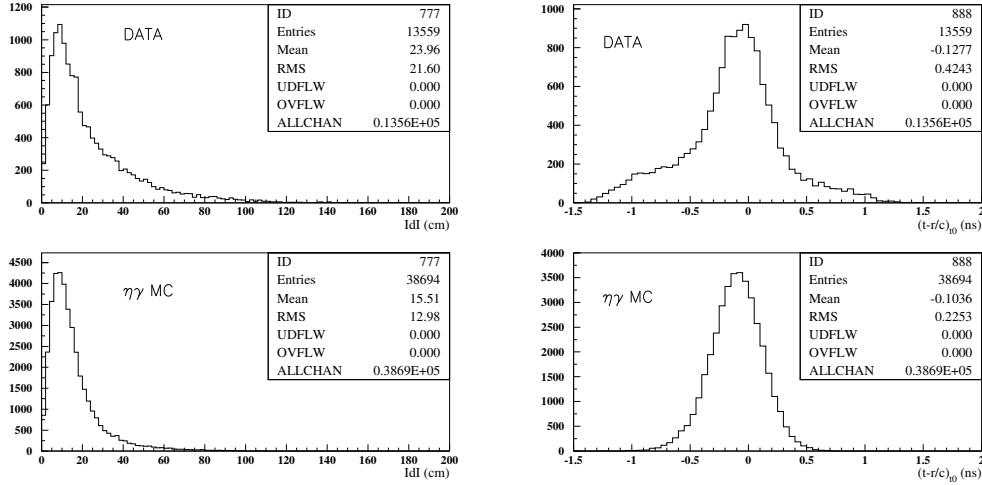


Figure 6.20: Distributions in the variable $|d| = \sqrt{d_1^2 + d_2^2}$ (left) and $(t - r/c)t_0$ (right) for data (top) and $e^+e^- \rightarrow \eta\gamma$ MC events (bottom), after selections.

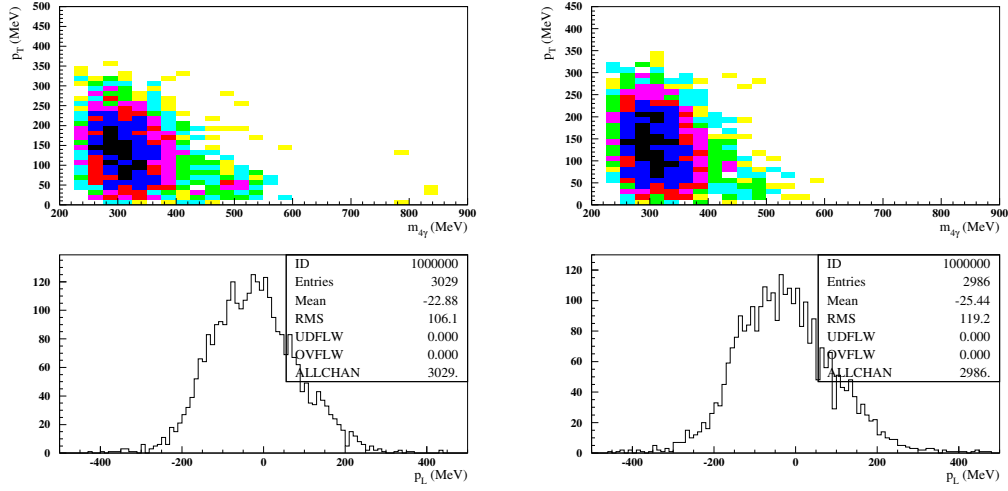


Figure 6.21: Scatter plot p_T vs $m_{4\gamma}$ (top) and p_L distribution (bottom) for events selected asking for $|d| > 33$ cm (left) or $|t - r/c|_{t_0} > 0.5$ ns (right).

Machine background events selection and normalization.

Considering the plane of the variables $|d| = \sqrt{d_1^2 + d_2^2}$ and $|t - r/c|_{t_0}$ (Fig. 6.22), one can define the four regions:

- A: $|d| > 33$ cm, $|t - r/c|_{t_0} < 0.5$ ns;
- B: $|d| > 33$ cm, $|t - r/c|_{t_0} > 0.5$ ns;
- C: $|d| < 33$ cm, $|t - r/c|_{t_0} > 0.5$ ns;
- S: $|d| < 33$ cm, $|t - r/c|_{t_0} < 0.5$ ns.

Regions A, B and C will be *background enriched*, while region S will be mainly populated by signal events.

In Tabs. 6.8, 6.9 the yields of events in the four regions defined above are listed for data and for MC simulations, normalized to efficiencies and cross sections. As a pure matter of convention, yields for data are indicated with capital letters (A = data events in the region A) while lower case is used for yields for simulated processes.

In order to estimate the yield of background events, one can use information from regions A, B and C to infer the background population in S. Assuming the

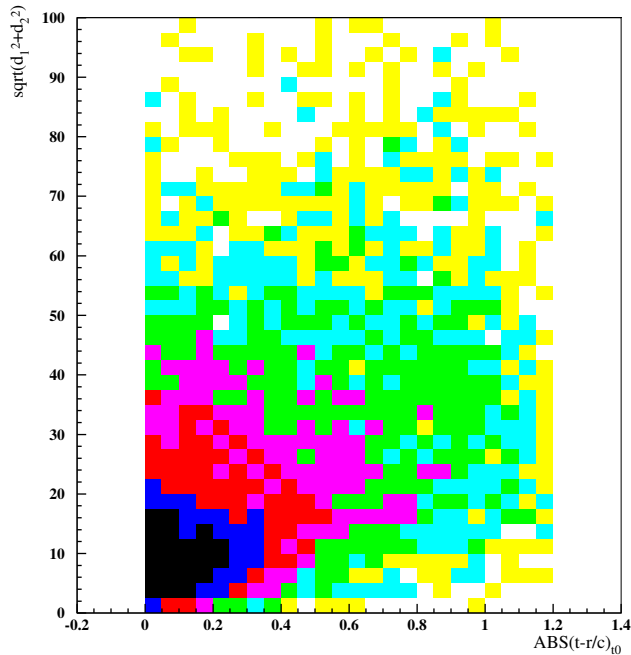


Figure 6.22: Scatter plot in the variables $|d|$ vs $|t - r/c|_{t_0}$ (data).

	A	B	C	S
Data	1577	1699	1488	8795

Table 6.8: Number of data events in the four regions A, B, C and S of the $|d|$, $|t - r/c|_{t_0}$ plane.

	a	b	c	s
$K_S K_L$	151	11	41	1569
$\eta\gamma$	32	3	17	378
$\omega\pi^0$	73	4	46	1719
$f_0\gamma$	5	-	2	106
$\gamma\gamma$	13	-	5	343
$a_0\gamma$	-	-	-	18

Table 6.9: Normalized number of MC events in the four regions A, B, C and S of the $|d|$, $|t - r/c|_{t_0}$ plane.

background to be uniformly distributed in the $|d|$, $|t - r/c|_{t_0}$ plane, the following relation holds:

$$Bkg(S) = \frac{(A - a)(C - c)}{(B - b)}, \quad (6.16)$$

$Bkg(S)$ being the yield of background events in the signal (S) region. Using the numbers in Tabs. 6.8, 6.9 one obtains

$$Bkg(S) = \frac{1303 \cdot 1392}{1683} = 1078.$$

The total yield of background events is then simply given by

$$Bkg = (A - a) + (B - b) + (C - c) + Bkg(S) = 5456. \quad (6.17)$$

Using Eq.6.17 fractions of background events have been evaluated for several values of the boundaries of regions A, B, C and S. Both $|d|$ and $|t - r/c|_{t_0}$ values have been moved away from central values by an amount of 20%. The corresponding variations in the fractions estimates are around 5 – 7%, as shown in Tab. 6.10.

	$ d < 26$ cm	$ d < 33$ cm	$ d < 40$ cm
$ t - r/c _{t_0} < 0.4$ ns		0.438	
$ t - r/c _{t_0} < 0.5$ ns	0.439	0.402	0.389
$ t - r/c _{t_0} < 0.6$ ns		0.389	

Table 6.10: Fractions of background events estimated from Eq. 6.17 using several definitions of regions A, B, C and S. Both $|d|$ and $|t - r/c|_{t_0}$ values are moved away from central values by an amount of 20%. The corresponding variations in the fractions estimates are around 5 – 7%.

In the following, central values $|d| = 33$ cm and $|t - r/c|_{t_0} = 0.5$ ns are used to define the boundaries of regions A, B, C and S.

6.5.2 Training

Training Input

Training is performed using the following samples as training events:

- **Signal:** sum of properly weighted MC distributions, all processes included (annihilation processes and $e^+e^- \rightarrow e^+e^-\pi^0\pi^0$ simulations);
- **Background:** half statistics (even events) of the A+B+C data population, properly normalized. The other half statistics (odd events) of the A+B+C data population, which is included in the sample used in the application phase, is excluded here in order to avoid to use the same set for both training and application.

Signals and background contributions are normalized according to the result of a fit to data invariant mass spectrum, from which training background events (even events of the A+B+C data population) have been removed: this spectrum consists in 11170 data events. The fit procedure is initialized providing starting values for processes normalizations, which are given by:

1. for annihilation processes: normalizations to efficiencies and cross sections;
2. for background: yield of even events of the A+B+C data population (2389) plus the estimate of background events in the signal region (1078), according to Eq. (6.16);
3. for $e^+e^- \rightarrow e^+e^-\pi^0\pi^0$ events: the complement to the total number of events in the data spectrum to be fitted.

The fit procedure returns a $\chi^2/n_{dof} = 107/62$. Fit parameters, starting values, ranges of variation and results are listed in Tab. 6.11; the result is also shown in Fig. 6.23. Note that the fraction of $K_S K_L$ events is lowered by the fit procedure; an error of $\simeq 6\%$ is given for this fraction, $f_{K_S K_L} = 0.12127 \pm 0.00743$.

$e^+e^- \rightarrow$	$n = \mathcal{L}\epsilon\sigma$	$n_{data} = 11170$			f_{fit}
		$f_{start} = n/n_{data}$	-%	+%	
$K_S K_L$	1610	0.144	30	30	0.12127 ± 0.00743
$\eta\gamma$	394	0.035	5	5	0.03325 ± 0.00322
$\omega\pi^0$	1750	0.156	20	20	0.17982 ± 0.00712
$f_0\gamma$	109	0.010	20	20	0.008 ± 0.00391
$\gamma\gamma$	330	0.029	20	20	0.0348 ± 0.00738
$a_0\gamma$	17	0.001	20	20	0.00120 ± 0.00032
	n (estimate)				
Bkg	2389+1078=3467	0.310	90	900	0.33303 ± 0.01553
	$n = 11170 - \sum_i n_i$				
$\gamma\gamma \rightarrow \pi^0\pi^0$	3493	0.313	90	900	0.28808 ± 0.01888

Table 6.11: Summary table of the preliminary fit to $m_{4\gamma}$ data spectrum. Fractions of events $f_{start} = n/n_{data}$ are used as starting values for the fit procedure. 20% variations are allowed for all background physical processes, with the exception of $K_S K_L$ process (uncertainty on both cross section and efficiency), for which a 30% variation is allowed, and $e^+e^- \rightarrow \eta\gamma$ (cross section measured with great precision by KLOE [19]), for which a stricter range of 5% has been used. Machine background and signal $e^+e^- \rightarrow e^+e^-\pi^0\pi^0$ contributions are set free. Fractions f_{fit} returned by the fit are used to normalize input distributions for the multivariate analysis.

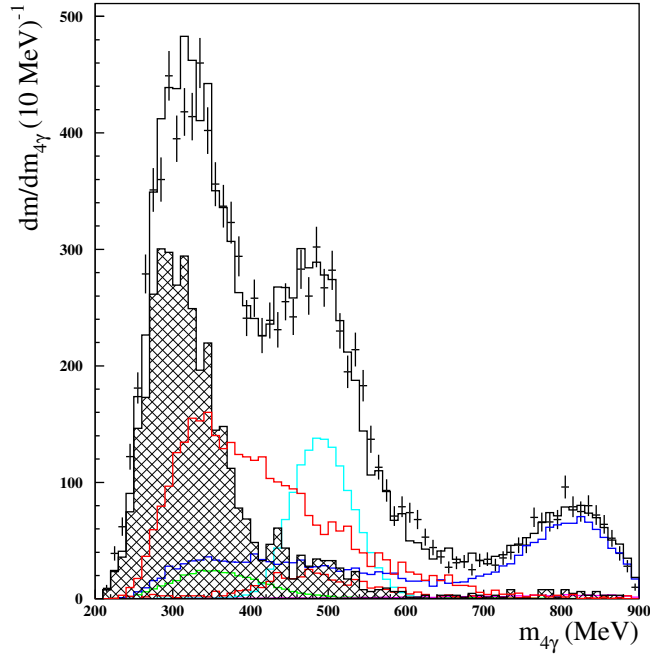


Figure 6.23: Data $m_{4\gamma}$ spectrum (points with error bars) fitted with signals and background distributions normalized according to the values provided by the preliminary fit to $m_{4\gamma}$, listed in Tab. 6.11. Color code: light blue = $K_S K_L$, green = $\eta\gamma$, dark blue = $\omega\pi^0$, violet = $f_0\gamma$, red = $e^+e^- \rightarrow e^+e^-\pi^0\pi^0$, black texture = machine background; the black solid line is the sum of all contribution.

The longitudinal and transverse momentum (p_L and p_T) and the “promptness” χ^2 (χ_t^2) have been chosen as input variables to be used for training (and application) as they are the more suitable in discriminating background from signal. Even if there is no purpose to reproduce data spectra at this stage, a $\sigma = 40$ MeV gaussian smearing has been applied to x and y momentum component for $\gamma\gamma \rightarrow \pi^0\pi^0$ MC events. p_L and χ_t^2 spectra for data, Signal(s) and background normalized according to the preliminary fit results are shown in Fig. 6.24. The variables $m_{4\gamma}$ and $|t - r/c|_{t_0}$ have been set as “spectator” variables, in the sense that they are not actively used to train the method and to build up the classifier but they are nevertheless stored as check variables to look at.

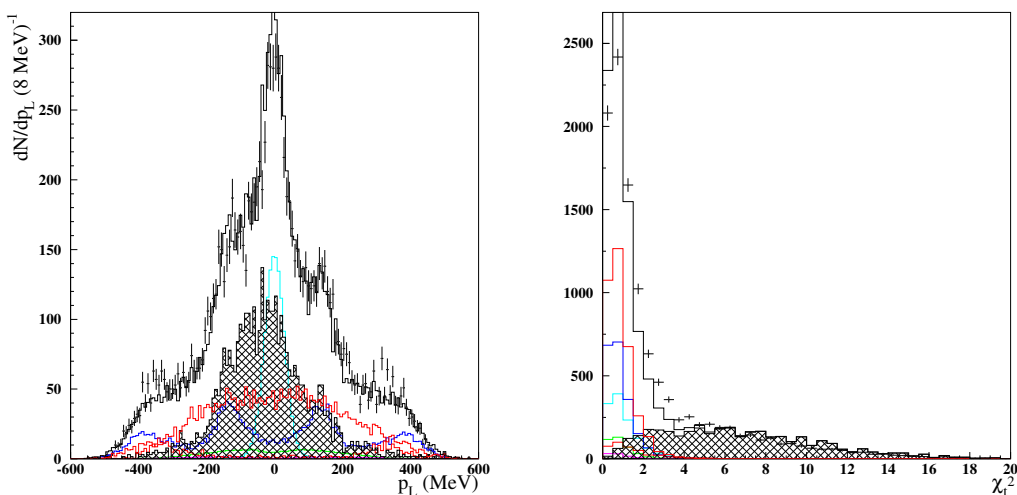


Figure 6.24: Data p_L (left) and χ_t^2 spectra (points with error bars) fitted with signals and background distributions normalized according to the values provided by the preliminary fit to $m_{4\gamma}$, listed in Tab. 6.11. Color code: light blue = $K_S K_L$, green = $\eta\gamma$, dark blue = $\omega\pi^0$, violet = $f_0\gamma$, red = $e^+e^- \rightarrow e^+e^-\pi^0\pi^0$, black texture = machine background; the black solid line is the sum of all contribution.

Input distributions for background and signal are shown in Fig. 6.25.

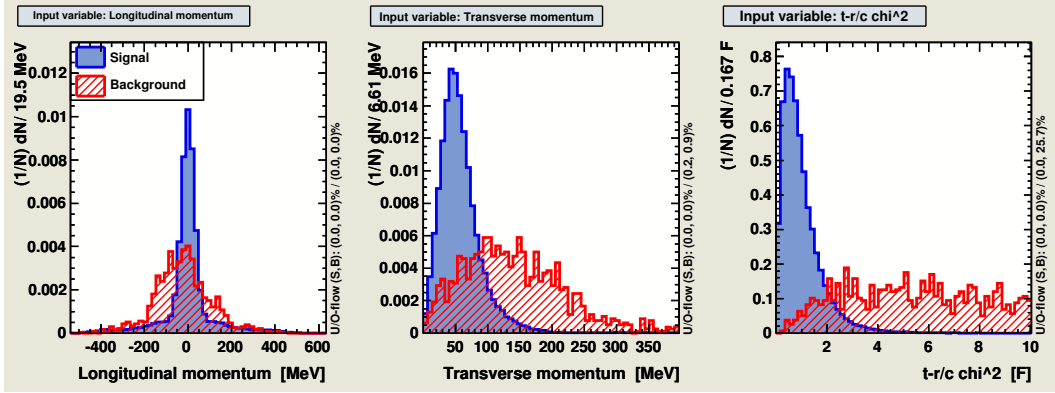


Figure 6.25: Input variables used to train the multivariate methods and to build up the output classifier. Signal shapes are obtained as the sum of all physical (annihilation and $\gamma\gamma$ fusion) processes, weighted according to the previous fit results. In these plots signal (blue) and background (red) distributions are normalized to the same number of events.

Training output

Several classifiers, corresponding to different multivariate approaches, are available within the TMVA package. A simple, linear likelihood response (in the following indicated with \mathcal{L}) has been chosen as the most efficient, and at the same time the easiest to handle, classifier method. In the *evaluation* phase, a subset of the training events which is orthogonal to the one used for training is employed to evaluate the classification performance, that is the signal/background discrimination power of the method, which is described by efficiencies functions. Likelihood response distributions for Signal(s) and Background are shown in Fig. 6.26; Signal(s) efficiency and purity, Background acceptance and Significance (defined as the ratio $\text{Signal}/\sqrt{\text{Signal} + \text{Background}}$) are plotted as functions of the Likelihood response value in Fig. 6.27.

TMVA also provides the optimal cut value, that is the response value for which the significance is maximum.

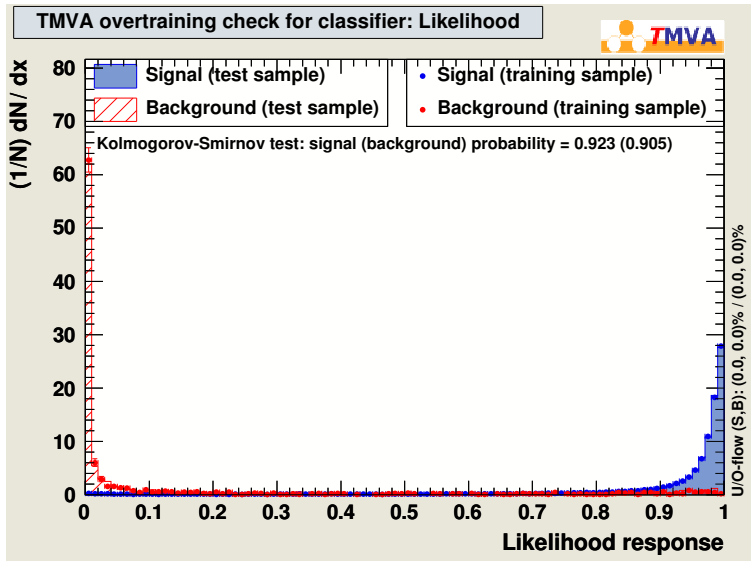


Figure 6.26: Likelihood response distributions for Signal (blue) and Background (red).

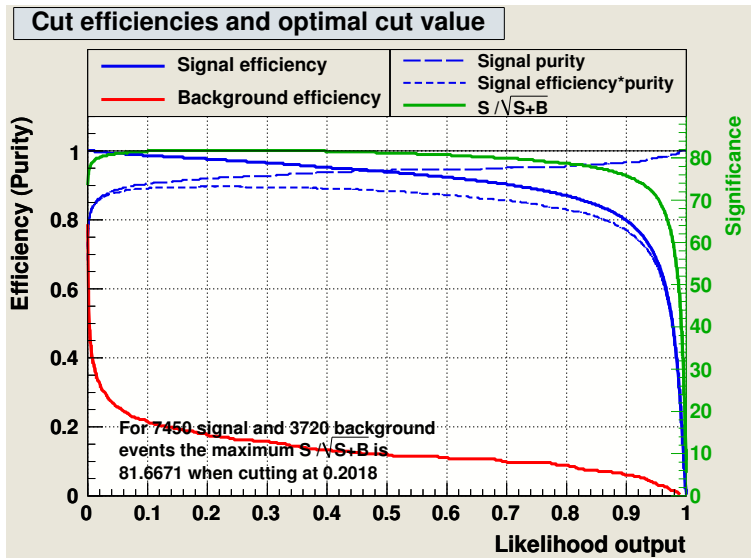


Figure 6.27: Signal efficiency, Signal purity, Background acceptance and Significance as functions of the Likelihood response \mathcal{L} . The optimal cut value on \mathcal{L} which maximizes significance is found to be $\mathcal{L} > 0.2018$.

6.5.3 Application

In the application phase, the algorithm “learned” in the training phase is passed through data events to be analyzed, for which \mathcal{L} values are computed; the resulting distribution is shown in Fig. 6.28.

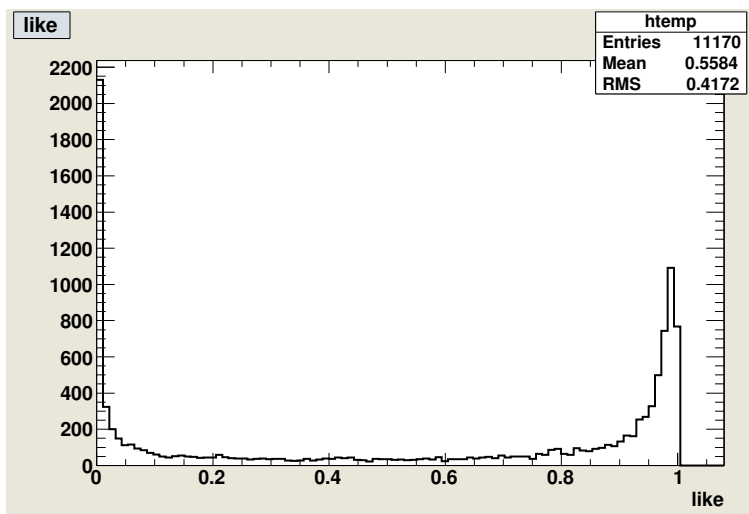


Figure 6.28: Likelihood response distribution for data events.

The evaluation algorithm has been applied to each signal MC distribution, too, in order to evaluate efficiencies for each process separately; in particular, efficiency of cutting on \mathcal{L} for the $\gamma\gamma \rightarrow \pi^0\pi^0$ process has to be parametrized as a function of $m_{4\gamma}$ and included in a overall selection efficiency with cuts efficiencies described in §6.4.6; application has been performed on the background sample, too, in order to check the acceptance estimate from evaluation phase. In Fig.6.29 \mathcal{L} distributions for signals and background normalized according to the preliminary fit result are showed superimposed to the \mathcal{L} distribution for data.

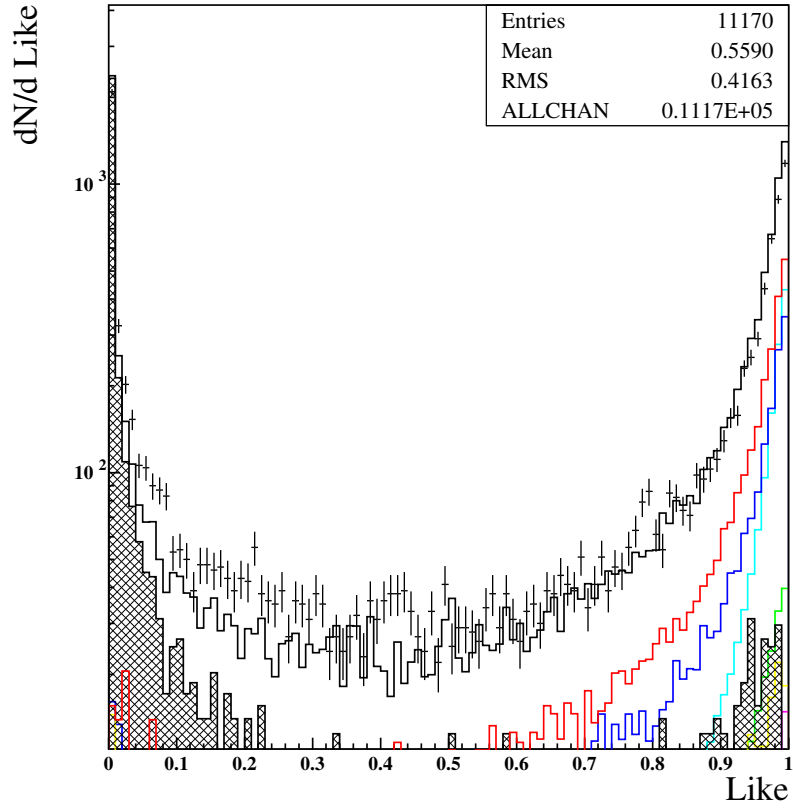


Figure 6.29: Likelihood response distribution for data events (points with error bars), background (black texture) and Signals. Color code: red = $e^+e^- \rightarrow e^+e^-\pi^0\pi^0$, light blue = $e^+e^- \rightarrow K_S K_L$, green = $e^+e^- \rightarrow \eta\gamma$, dark blue = $e^+e^- \rightarrow \omega\pi^0$, yellow = $e^+e^- \rightarrow a_0\gamma$; the black histogram is the sum of all contributions (Signals and background). Normalizations according to preliminary fit result, see Tab. 6.11.

6.5.4 Cut on the MVA response

The value $\mathcal{L} = 0.5$ has been chosen as the background/Signal(s) separator (Fig.6.29). Moving this value has been used as a criterium to evaluate related systematics. Looking at Fig.6.27, rejecting events with $\mathcal{L} < 0.5$ results in a $\approx 95\%$ efficiency for the Signal(s) with a $\approx 95\%$ purity, and a $\approx 11\%$ background acceptance.

Number of events for data, signal(s) and background samples used in the multivariate analysis are listed in Tab. 6.12 before and after applying the cut $\mathcal{L} > 0.5$. Reduction factors are also listed in the last column.

For $\gamma\gamma \rightarrow \pi^0\pi^0$ process, $\mathcal{L} > 0.5$ cut efficiency has been evaluated using both

- yields obtained by subtraction of other signals and background contributions from data spectra before and after the cut, indicated in Tab. 6.12 as “ $\gamma\gamma \rightarrow \pi^0\pi^0$ (data)”, and
- absolute MC yields, indicated in Tab. 6.12 as “ $\gamma\gamma \rightarrow \pi^0\pi^0$ (MC)”.

Acceptance for Background has been checked looking at absolute number of events in the training sample, before and after the cut $\mathcal{L} > 0.5$, indicated in Tab. 6.12 as “Bkg (training sample)”; a value of 11% has been obtained, in agreement with the estimate provided by TMVA.

In Fig.6.30 spectra in $m_{4\gamma}$ are shown after $\mathcal{L} > 0.5$ cut for data, background and all signals but $\gamma\gamma \rightarrow \pi^0\pi^0$ process, using normalizations in Tab. 6.12. In Fig.6.31 the $m_{4\gamma}$ spectrum obtained by subtracting all contributions but $\gamma\gamma \rightarrow \pi^0\pi^0$ process from data is compared with $\gamma\gamma \rightarrow \pi^0\pi^0$ MC events distribution, showing a good agreement. The 2347 events in the subtracted spectrum are candidates to $e^+e^- \rightarrow e^+e^-\pi^0\pi^0$ processes.

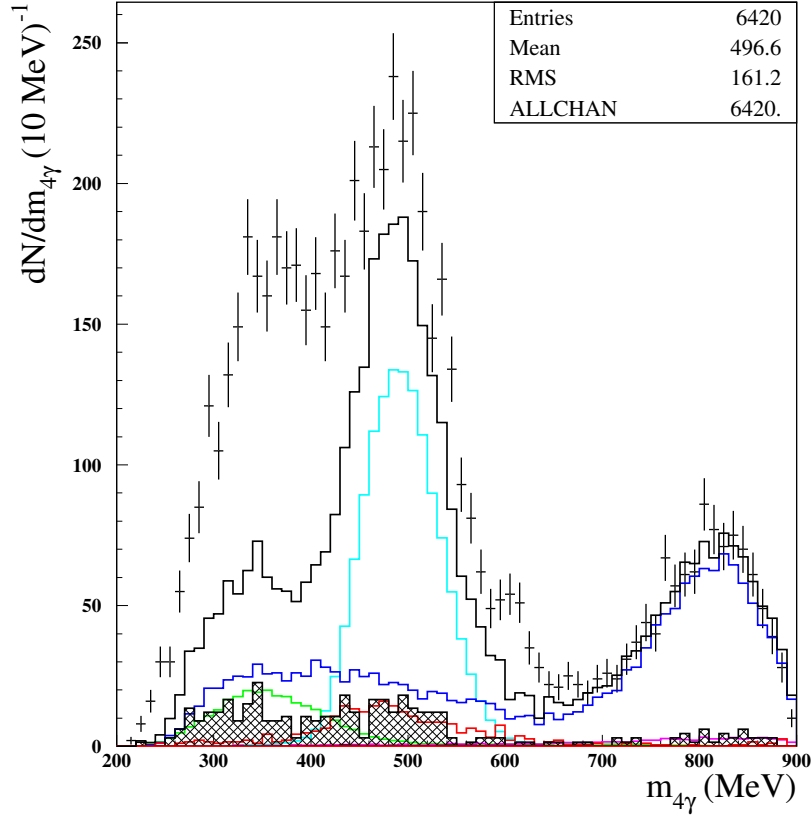


Figure 6.30: Spectra in $m_{4\gamma}$ after $\mathcal{L} > 0.5$ cut for data (points with error bars), background (black texture) and all signals but $\gamma\gamma \rightarrow \pi^0\pi^0$ process, using normalizations in Tab. 6.12 Color code: light blue = $K_S K_L$, green = $\eta\gamma$, dark blue = $\omega\pi^0$, violet = $f_0\gamma$. Black solid line is the sum of contributions.

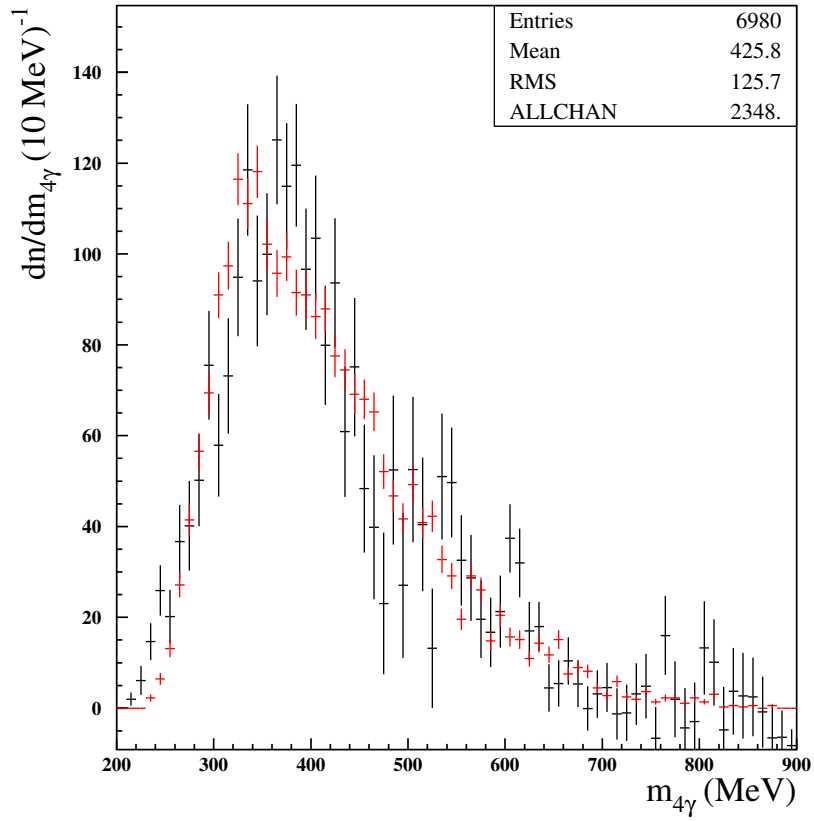


Figure 6.31: $m_{4\gamma}$ spectrum obtained by subtracting all contributions but $\gamma\gamma \rightarrow \pi^0\pi^0$ process from data (black points), compared with normalized $\gamma\gamma \rightarrow \pi^0\pi^0$ MC events distribution (red points).

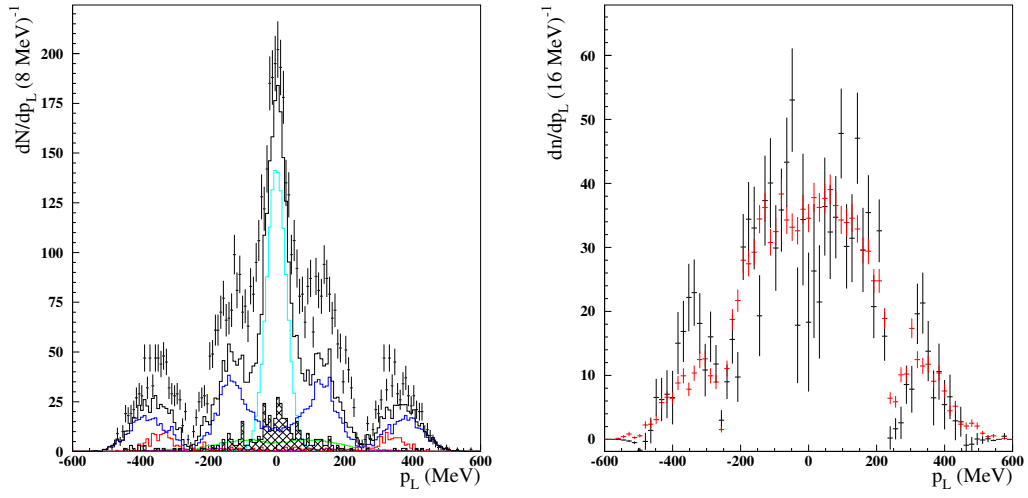


Figure 6.32: Left: spectra in p_L after $\mathcal{L} > 0.5$ cut for data (points with error bars), background (black texture) and all signals but $\gamma\gamma \rightarrow \pi^0\pi^0$ process, using normalizations in Tab. 6.12 Color code: light blue = $K_S K_L$, green = $\eta\gamma$, dark blue = $\omega\pi^0$, violet = $f_0\gamma$ Black solid line is the sum of contributions. Right: the p_L spectrum obtained by subtracting all contributions but $\gamma\gamma \rightarrow \pi^0\pi^0$ process from data (black points), compared with normalized $\gamma\gamma \rightarrow \pi^0\pi^0$ MC events distribution (red points).

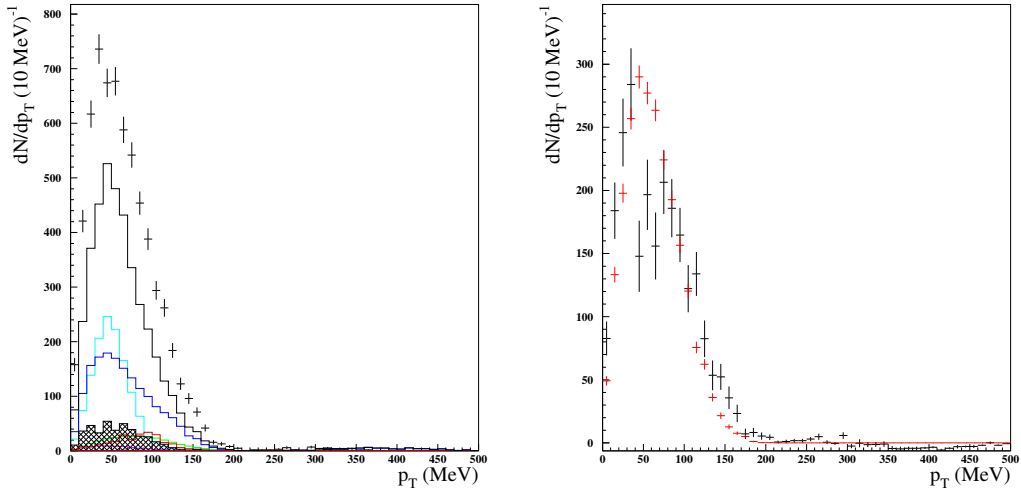


Figure 6.33: Left: spectra in p_T after $\mathcal{L} > 0.25$ cut for data (points with error bars), background (black texture) and all signals but $\gamma\gamma \rightarrow \pi^0\pi^0$ process, using normalizations in Tab. 6.12 Color code: light blue = $K_S K_L$, green = $\eta\gamma$, dark blue = $\omega\pi^0$, violet = $f_0\gamma$ Black solid line is the sum of contributions. Right: the p_T spectrum obtained by subtracting all contributions but $\gamma\gamma \rightarrow \pi^0\pi^0$ process from data (black points), compared with normalized $\gamma\gamma \rightarrow \pi^0\pi^0$ MC events distribution (red points). A $\sigma = 40$ MeV gaussian smearing has been applied to p_x and p_y in the MC events.

	n_{start}	$n_{\mathcal{L}>0.5}$	%
Data	11170	6420	57
$K_S K_L$	1354	1313	97
$\eta\gamma$	371	293	79
$\omega\pi^0$	2008	1726	86
$f_0\gamma$	89	73	82
$\gamma\gamma$	389	249	64
$a_0\gamma$	13	10	75
Bkg (TMVA)	3720	409	11
$\gamma\gamma \rightarrow \pi^0\pi^0$ (data)	3218	$2347 = 6420 - \sum_i n_i$	73
Bkg (training sample)	2389	271	11
$\gamma\gamma \rightarrow \pi^0\pi^0$ (MC)	9724	8389	86

Table 6.12: Number of events for signals and background before and after applying the $\mathcal{L} > 0.5$ cut, and correspondent efficiencies (acceptance). For $\gamma\gamma \rightarrow \pi^0\pi^0$ events both yields obtained from subtracted spectra and absolute MC simulation yields have been used to evaluate efficiency, obtaining compatible results. For background, acceptance estimate from TMVA ($\simeq 11\%$) has been checked using training background sample, yielding the same value.

6.5.5 Selection for background

As a cross-check, a sample of background has been selected applying the cut $\mathcal{L} < 0.25$. Distributions in $m_{4\gamma}$, p_T , p_L and $(t - r/c)_{t_0}$ for this sample are plotted in Figg.6.34,6.35, and show all the feature of the correspondent distributions for data selected in the background enriched regions in the $|d|, |t - r/c|_{t_0}$ plane (§6.5.1).

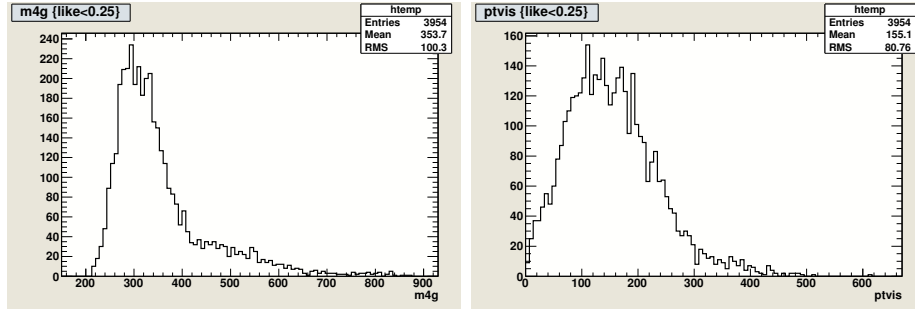


Figure 6.34: Distribution in $m_{4\gamma}$ (left) and in transverse momentum (right) for data selected asking for $\mathcal{L} < 0.25$.

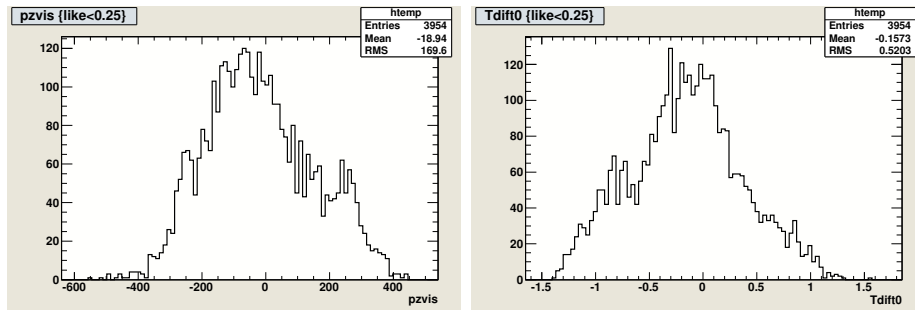


Figure 6.35: Distribution in longitudinal momentum (left) and in $(t - r/c)_{t_0}$ (right) for data selected asking for $\mathcal{L} < 0.25$.

Chapter 7

Extraction of $\gamma\gamma \rightarrow \pi^0\pi^0$ cross section

In Chapter 6 the selection criteria to obtain a $e^+e^- \rightarrow e^+e^-\pi^0\pi^0$ events sample have been illustrated. Fig. 7.1, top panel, shows candidate $e^+e^- \rightarrow e^+e^-\pi^0\pi^0$ events obtained from data spectrum at the end of the analysis (cut-based and multivariate) subtracting known process contributions, as explained above; according to resolution function (§6.3.1), a 40 MeV binning has been chosen instead of the 10 MeV binning employed so far. The distribution of $e^+e^- \rightarrow e^+e^-\pi^0\pi^0$ events in the variable $m_{4\gamma}$ can be written in terms of the differential cross section and the selection efficiency as

$$\frac{dn}{dm_{4\gamma}} = \mathcal{L}\epsilon(m_{4\gamma})\frac{d\sigma(e^+e^- \rightarrow e^+e^-\pi^0\pi^0)}{dm_{4\gamma}}, \quad (7.1)$$

where \mathcal{L} is the integrated luminosity and $\epsilon(m_{4\gamma})$ is the detection/selection efficiency parametrized as a function of the invariant mass. As discussed in §2.1, differential cross section $d\sigma/dm_{4\gamma}$ can be factorized in the product of the $\gamma\gamma \rightarrow \pi^0\pi^0$ cross section times a photons flux (luminosity) function, in such a way that Eq.(7.1) becomes

$$\frac{dn}{dm_{4\gamma}} = \mathcal{L}\epsilon(m_{4\gamma})L_{\gamma\gamma}(m_{4\gamma})\sigma_{\gamma\gamma \rightarrow \pi^0\pi^0}(m_{4\gamma}). \quad (7.2)$$

In this chapter the extraction of the $\gamma\gamma \rightarrow \pi^0\pi^0$ cross section, by inverting Eq.(7.2), is described. Parametrization as functions of $m_{4\gamma}$ are necessary for both the detection/selection efficiency and the luminosity function; this issue is described in §§7.1, 7.3.

7.1 Selections efficiency on signal

The overall selection efficiency on $e^+e^- \rightarrow e^+e^-\pi^0\pi^0$ signal is comprehensive of preselections, reconstruction, analysis cuts and cut on the likelihood response \mathcal{L} returned by TMVA. The behavior as function of $m_{4\gamma}$ is obtained dividing bin per bin the $e^+e^- \rightarrow e^+e^-\pi^0\pi^0$ MC events spectrum obtained after all selections and cutting $\mathcal{L} > 0.5$ (numerator) by the spectrum of generated events (denominator); for the latter the folding procedure of the $m_{2\pi^0}$ distribution by the smearing matrix method has been applied (§6.3.1). The efficiency curve is shown in Fig. 7.1, bottom panel.

One could think that efficiency evaluation is model dependent as a Monte Carlo simulation assuming a particular shape for the resonance (determined by the input for mass and width) has been employed. Fig. 7.2 shows that this is not the case, as for large resonances convolution with the flux function pushes the distribution towards threshold making different Breit-Wigner functions quite indistinguishable; residual differences are almost completely wiped out by resolution effects. Distributions according to three different Breit-Wigner functions, with σ meson mass and width given by Bes, CLEO and E791 experiments (see Tab. 5.1) are shown both with a fine 10-MeV binning and with a 40-MeV binning which is a realistic realization of detection and reconstruction resolution effects. No one of the three curves is even really distinguishable from a phase-space (non resonant) generated distribution, also plotted (in blue).

In extracting $\gamma\gamma \rightarrow \pi^0\pi^0$ cross section a crucial role is played by the $\gamma\gamma$ luminosity function, as widely discussed in Chapter 1. Parameterization of the $\gamma\gamma$ flux function is a purely theoretical task and, in that sense, deconvolution of the observed spectrum by the flux function is a step completely disentangled from the rest of the analysis. In other words, dividing the spectrum by a particular parametrization of the luminosity function could introduce a systematic error which has nothing to do with the experimental facts and with the analysis strategy. From an experimental point of view, one is mainly interested in verifying stability of the ratio data/efficiency: in the next section evaluation of systematic errors on counting spectrum corrected (i.e. divided) by efficiency is presented.

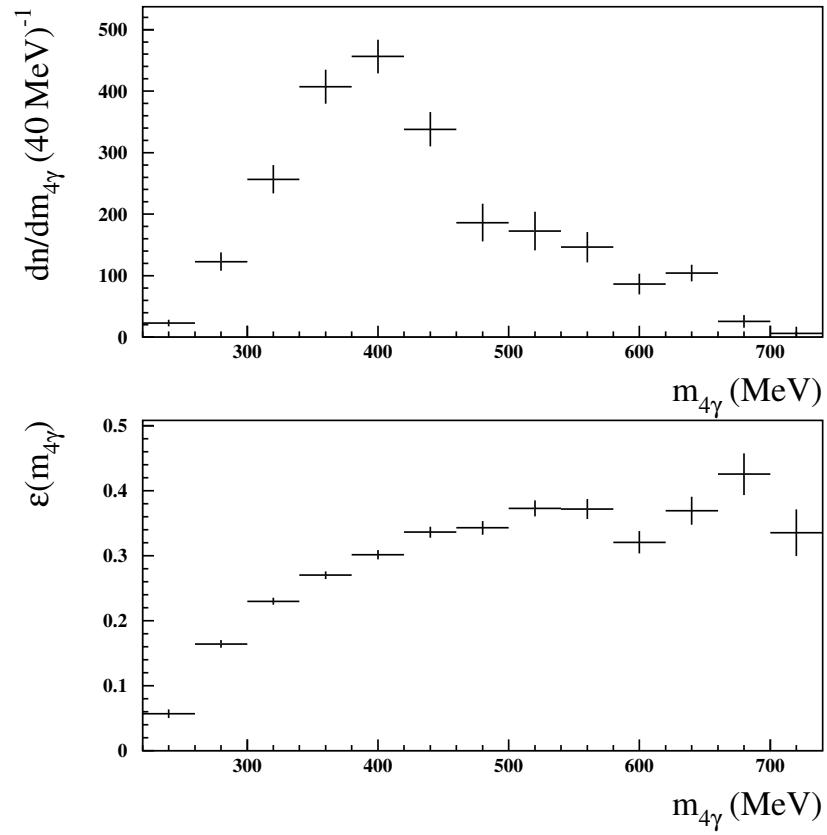


Figure 7.1: Subtracted spectrum (top) and selection efficiency (bottom) at the end of the analysis.

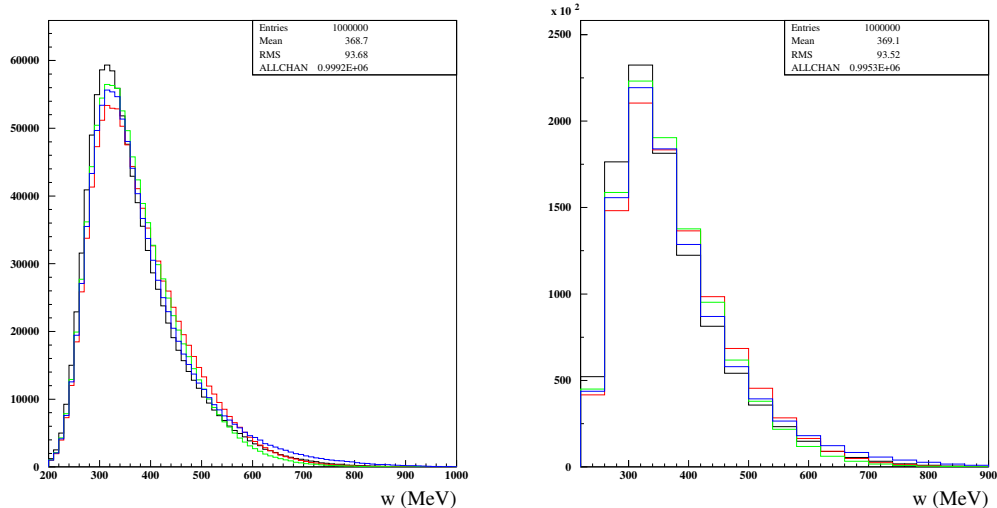


Figure 7.2: Comparison between distribution according a convolution of the $\gamma\gamma$ flux function (according to Budnev *et al.* [11]) and a relativistic Breit-Wigner function (see §2.1.2) with three different parameterizations, according to values quoted by BES, CLEO and E791 for the σ meson mass and width (black, red and green histograms respectively). The blue distribution is generated according a phase-space function, $f(w) = \frac{1}{w^2} \sqrt{1 - 4m_\pi^2/w^2}$, convoluted with the $\gamma\gamma$ flux function. In the right plot, a more realistic binning almost completely wipes out differences among these distributions.

7.2 Systematic errors

In the course of the analysis, data-Monte Carlo comparison have been constantly performed in order to individuate offsets and mismatches and to correct them. Nevertheless, the following sources of systematic uncertainties have been individuated:

1. efficiencies evaluation by Monte Carlo;
2. cross sections estimate for some background processes, mainly $e^+e^- \rightarrow K_S K_L$ (but also $e^+e^- \rightarrow f_0\gamma$, $e^+e^- \rightarrow a_0\gamma$);
3. unknown pathological background subtraction;
4. $e^+e^- \rightarrow e^+e^-\pi^0\pi^0$ Monte Carlo simulation.

Points 1-2 both contribute to the uncertainty on (known) background normalization. With respect to cross sections, errors introduced by uncertainty on $f_0\gamma$ and $a_0\gamma$ production cross section are likely negligible, as these processes are strongly suppressed by analysis cuts and poorly contribute to the final selected spectrum. As $K_S K_L$ production is massive even at $\sqrt{s} = 1$ GeV, normalization for this process is crucial and needs to be studied in detail. Both cross section measurement and efficiency evaluation are sources of systematics for the $450 \div 550$ MeV interval in the subtracted spectrum, and it is worth making an effort to quantify this uncertainty. At the moment the $\simeq 6\%$ error on $K_S K_L$ normalization provided by the preliminary fit is assumed as uncertainty on bins 5 to 9 in the 40-MeV binned subtracted spectrum, Fig. 7.1 (top panel).

Uncertainty due to pathological unknown background subtraction is difficult to quantify as one does not exactly know what he is dealing with. Effort has still to be made first of all to identify these background processes and somehow simulate them.

Systematics introduced by signal Monte Carlo are expected to be small, as simulated $e^+e^- \rightarrow e^+e^-\pi^0\pi^0$ events have mainly been used to efficiency evaluation, and not to fit to data. The only performed fit in which the signal MC has been employed is the preliminary fit to invariant mass which is used to tune processes normalizations before using distributions to train the multivariate analysis (§6.5.2); the bias introduced in this way is expected to be small, as invariant mass distribution is poorly sensitive to the exact resonance modelization, as shown in the previous section (Fig. 7.2). In any case, the only way one can quantify the systematic introduced by using a particular simulation for an unknown process such as $e^+e^- \rightarrow e^+e^-\pi^0\pi^0$ (or, at least, the only way **I can imagine**) consists in providing another or more different simulations and performing the analysis again.

The only source of systematics that has been really investigated is that due to data-MC disagreement resulting in erroneous efficiencies evaluation. Such uncertainties have been evaluated re-performing the analysis slightly moving the cut application points. Data-MC disagreement, due to erroneous simulation or to contamination by residual backgrounds reflects in instability of data/efficiency ratio, from which uncertainty can be estimated. Procedure to decide the shift from the central cut value is described for the cut on the Likelihood output; cuts on other continuous variables ($\chi_{\pi\pi}^2$, E_{RMS}) are studied in the same fashion.

7.2.1 Cut on TMVA Likelihood Response

Distribution in the \mathcal{L} variable for data and training samples (Monte Carlo simulations and data driven background) has been shown in Fig. 6.29. One can consider the integral distributions for both data and sum of training samples, normalized to the same number of events, shown in Fig. 7.3: when cutting at $\mathcal{L}_0 > 0.5$ different fractions of events are selected for the black distribution (data) and the red one (sum of simulated processes, including the data driven background). This difference, which is source of a systematic error in evaluating the efficiency for this cut, is recovered by shifting the distributions one respect to the other by two possible values $\delta\mathcal{L}^- \simeq 0.15$, $\delta\mathcal{L}^+ \simeq 0.2$; the two values $\mathcal{L}_1 = \mathcal{L}_0 - \delta\mathcal{L}^-$, $\mathcal{L}_2 = \mathcal{L}_0 + \delta\mathcal{L}^+$ have been used as new working points to apply the cut, evaluate related efficiencies and perform subtraction. Number of events in each bin of the subtracted spectrum, correspondent MC-evaluated efficiencies and ratios n/ϵ are listed for chosen \mathcal{L} cut values (central values and shifted values) in Tab. 7.1. The efficiency-corrected subtracted spectra are shown in Fig. 7.4.

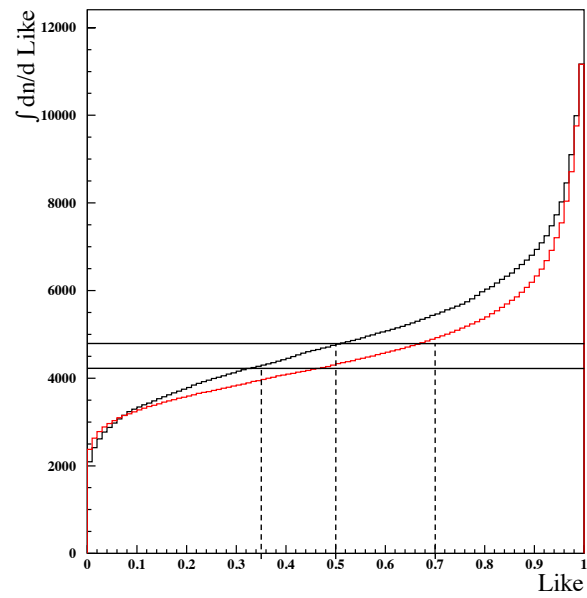


Figure 7.3: Integrated likelihood response distribution for data events (black) and Monte Carlo simulations+data driven background (red).

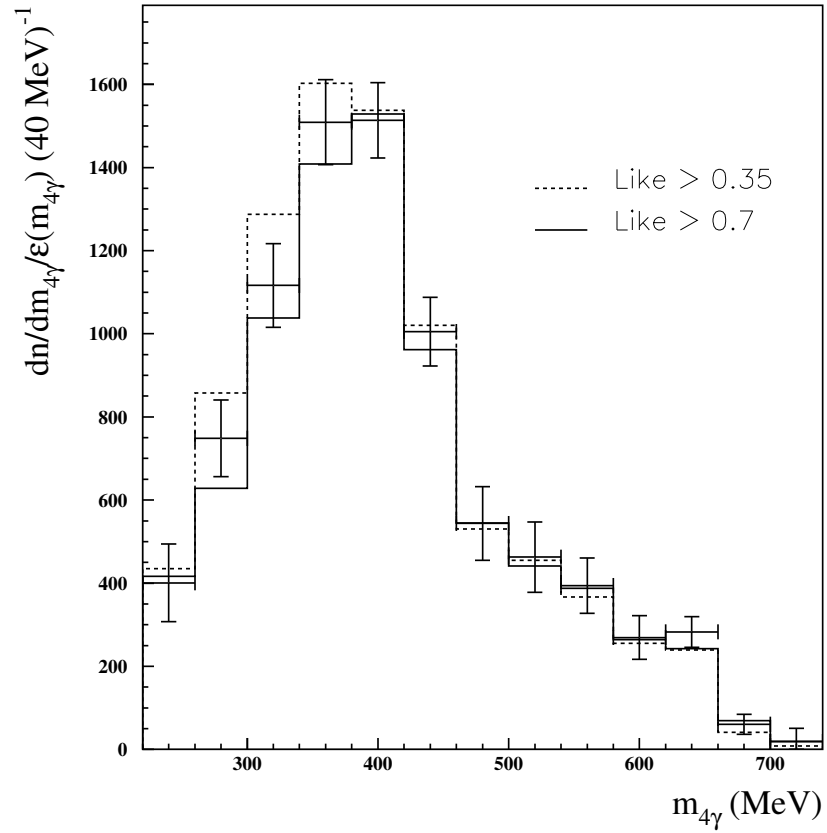


Figure 7.4: Efficiency-corrected subtracted spectra (dividing subtracted spectrum by efficiency bin-per-bin) obtained with standard value of the cut on \mathcal{L} (points with statistical error bars) and with $\mathcal{L} > 0.7$, $\mathcal{L} > 0.35$ cuts (solid and dashed lines, respectively).

$m_{4\gamma}$	$\mathcal{L} > 0.7$			$\mathcal{L} > 0.5$			$\mathcal{L} > 0.35$		
	n_{data}	ϵ	n_{data}/ϵ	n_{data}	ϵ	n_{data}/ϵ	n_{data}	ϵ	n_{data}/ϵ
240	21	0.0514	417	23	0.0568	401	25	0.0569	434
280	94	0.1499	628	123	0.1642	748	147	0.1711	857
320	218	0.2104	1038	257	0.2299	1116	308	0.2392	1287
360	348	0.2471	1409	407	0.2699	1509	448	0.2796	1602
400	420	0.2749	1529	456	0.3014	1513	489	0.3183	1537
440	295	0.3068	962	338	0.3361	1005	356	0.3487	1021
480	173	0.3179	544	186	0.3427	544	191	0.3602	530
520	148	0.3364	441	172	0.3727	463	177	0.3900	455
560	134	0.3475	387	146	0.3717	394	141	0.3840	366
600	77	0.2916	264	86	0.3205	269	89	0.3473	255
640	82	0.3374	242	104	0.3691	282	94	0.3930	239
680	25	0.3694	69	26	0.4252	60	18	0.4404	41
720	7	0.3352	20	6	0.3352	20	3	0.3481	8

Table 7.1: Number of events in the subtracted spectrum, efficiencies and ratios n_{data}/ϵ for three different values of the cut on the TMVA response \mathcal{L} .

7.2.2 $m_{4\gamma}$ reconstruction, cut on $\chi_{\pi\pi}^2$

$e^+e^- \rightarrow K_S K_L$ events with $K_S \rightarrow \pi^0 \pi^0$ selected as described in §5.2.2 have been used as a control sample to check data-MC agreement in the pairing procedure and in the 4γ invariant mass reconstruction and to evaluate related systematics.

Normalized distributions in the $\chi_{\pi\pi}^2$ variable are shown in Fig. 7.5 for data and $e^+e^- \rightarrow K_S K_L$ MC (left panel): quite good agreement is observed for $\chi_{\pi\pi}^2$ values up to $\simeq 4$. In Fig. 7.5, right panel, the integral of both distributions are shown. Proceeding as in the previous section, two working points shifted from central cut value $\chi_{\pi\pi}^2 = 4$ have been determined; analysis has been performed again for each cut value. Number of events in each bin of the subtracted spectrum, correspondent MC-evaluated efficiencies and ratios n/ϵ are listed for chosen $\chi_{\pi\pi}^2$ cut values (central values and shifted values) in Tab. 7.2. The efficiency-corrected subtracted spectra are shown in Fig. 7.6.

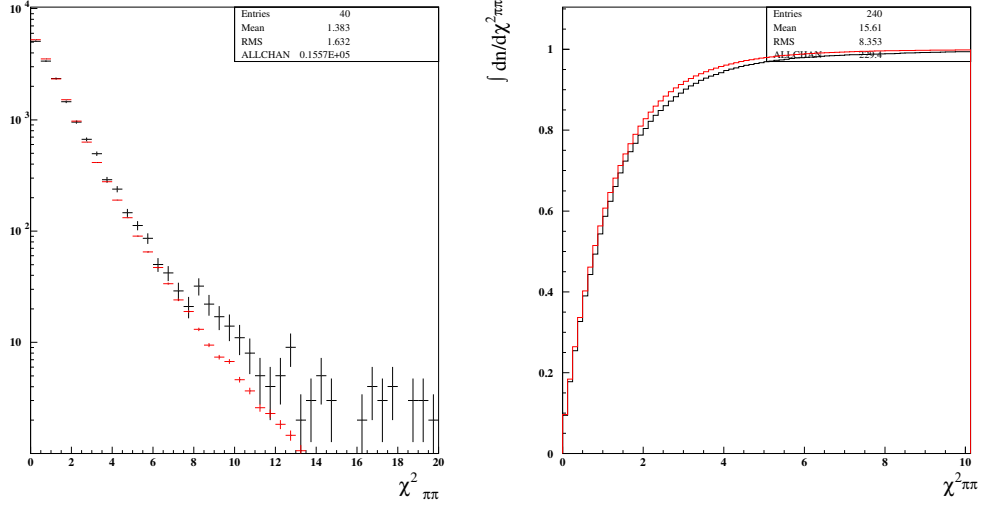


Figure 7.5: Left: normalized to unity distributions in $\chi^2_{\pi\pi}$ for data (black) and Monte Carlo (red) samples selected with dedicated analysis for $K_S K_L$, described in §5.2.2. Integrals of the distributions are shown in the right panel.

m_{4g}	$\chi^2_{\pi\pi} < 3.5$			$\chi^2_{\pi\pi} < 4$			$\chi^2_{\pi\pi} < 4.5$		
	n_{data}	ϵ	n_{data}/ϵ	n_{data}	ϵ	n_{data}/ϵ	n_{data}	ϵ	n_{data}/ϵ
240	15	0.0512	288	23	0.0568	401	27	0.06278	428
280	97	0.1586	616	123	0.1642	748	134	0.1682	798
320	224	0.2278	985	257	0.2299	1116	280	0.2401	1166
360	357	0.2661	1343	407	0.2699	1509	422	0.2861	1476
400	417	0.2997	1390	456	0.3014	1513	492	0.3249	1515
440	335	0.3289	1020	338	0.3361	1005	368	0.3535	1041
480	175	0.3323	527	186	0.3427	544	219	0.3692	594
520	152	0.3668	414	172	0.3727	463	191	0.4027	475
560	140	0.3700	378	146	0.3717	394	173	0.3976	436
600	73	0.3276	224	86	0.3205	269	105	0.3649	288
640	87	0.3678	238	104	0.3691	282	110	0.4107	267
680	19	0.4192	46	26	0.4252	60	28	0.4533	62
720	4	0.3493	12	6	0.3352	20	11	0.3497	32

Table 7.2: Number of events in the subtracted spectrum, efficiencies and ratios n_{data}/ϵ for three different values of the cut on the variable $\chi^2_{\pi\pi}$.

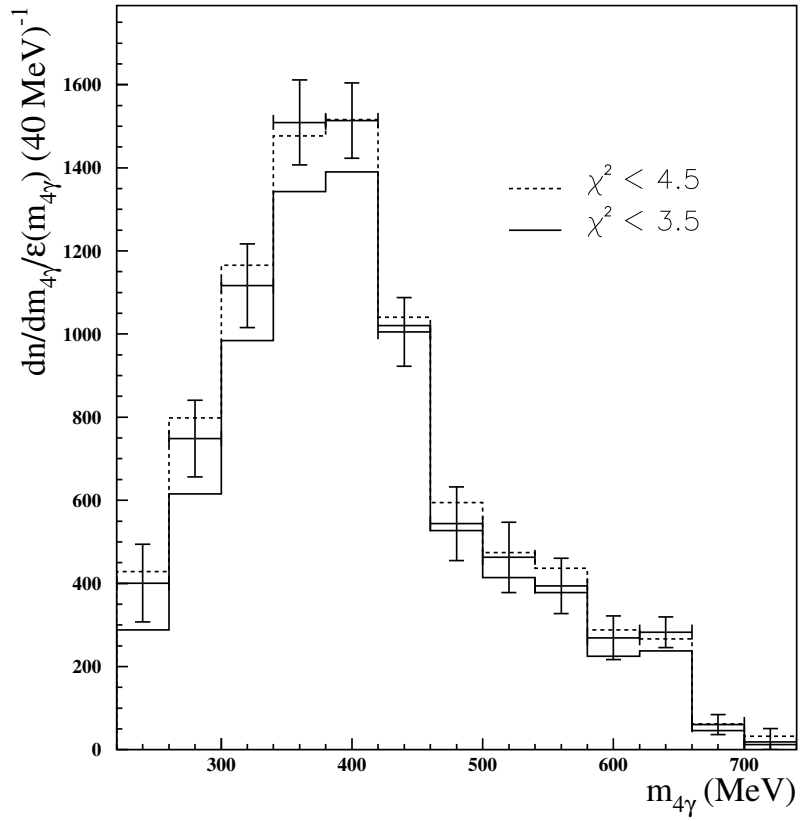


Figure 7.6: Efficiency-corrected subtracted spectra obtained with standard value of the cut on $\chi^2_{\pi\pi}$ (points with statistical error bars) and with $\chi^2_{\pi\pi} < 3.5$, $\chi^2_{\pi\pi} < 4.5$ cuts (solid and dashed lines, respectively).

7.2.3 Cut on E_{RMS}

As discussed in §6.4.5, $e^+e^- \rightarrow \omega\pi^0$ is one of the processes most sensitive to the cut on the variable E_{RMS} . This is the reason why this process has been chosen to perform data-MC checks in order to evaluate systematics connected to the cut on E_{RMS} .

Distributions in the E_{RMS} variable, normalized to the same number of events, are shown in Fig. 7.7 for data and $e^+e^- \rightarrow \omega\pi^0$ MC, selected as in §5.4 (left panel). E_{RMS} values are bounded in the interval (80, 200) MeV, with mean $\langle E_{RMS} \rangle = 140.8$ MeV. In Fig. 7.7, right panel, the integral of the two distributions are plotted. Proceeding as for \mathcal{L} and $\chi_{\pi\pi}^2$, the values $E_{RMS} = 135$ MeV and $E_{RMS} = 145$ MeV have been chosen as shifted working points; for these values analysis has been run again. Number of events in each bin of the subtracted spectrum, correspondent MC-evaluated efficiencies and ratios n/ϵ are listed in Tab. 7.3. The efficiency-corrected subtracted spectra are shown in Fig. 7.8.

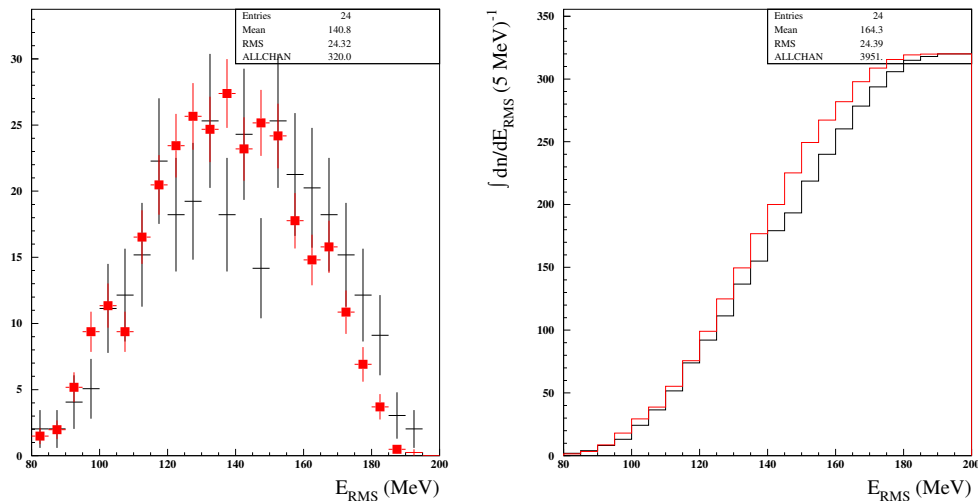


Figure 7.7: Left: normalized to unity distributions in E_{RMS} for data (black) and Monte Carlo (red) samples selected with dedicated analysis for $e^+e^- \rightarrow \omega\pi^0$, described in §5.4. Integrals of the distributions are shown in the right panel.

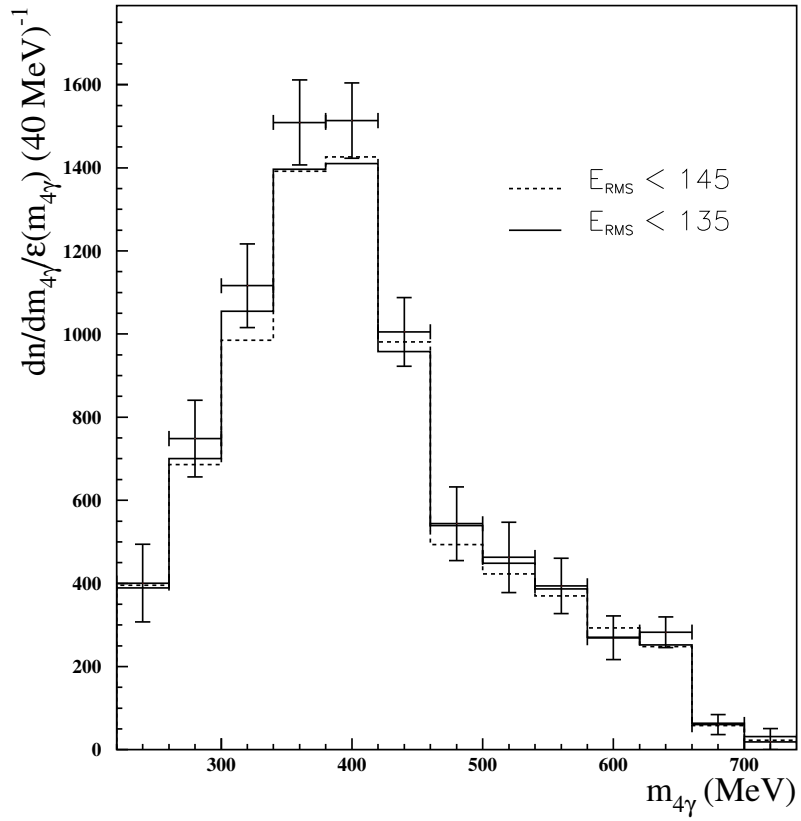


Figure 7.8: Efficiency-corrected subtracted spectra obtained with standard value of the cut on E_{RMS} (points with statistical error bars) and with $E_{RMS} < 135$, $E_{RMS} < 145$ cuts (solid and dashed lines, respectively).

$m_{4\gamma}$	$E_{RMS} < 135$ MeV			$E_{RMS} < 140$ MeV			$E_{RMS} < 145$ MeV		
	n_{data}	ϵ	n_{data}/ϵ	n_{data}	ϵ	n_{data}/ϵ	n_{data}	ϵ	n_{data}/ϵ
240	21	0.0561	389	23	0.0568	401	22	0.0549	396
280	117	0.1678	700	123	0.1642	748	112	0.1631	686
320	252	0.2392	1055	257	0.2299	1116	231	0.2346	985
360	394	0.2825	1396	407	0.2699	1509	381	0.2738	1392
400	452	0.3203	1410	456	0.3014	1513	443	0.3110	1426
440	333	0.3480	957	338	0.3361	1005	333	0.3395	981
480	191	0.3551	539	186	0.3427	544	176	0.3559	493
520	174	0.3889	449	172	0.3727	463	161	0.3823	423
560	147	0.3798	387	146	0.3717	394	141	0.3825	370
600	92	0.3432	270	86	0.3205	269	99	0.3366	293
640	95	0.3773	252	104	0.3691	282	98	0.3971	248
680	27	0.4242	63	26	0.4252	60	25	0.4318	58
720	11	0.3655	31	6	0.3352	20	8	0.3799	22

Table 7.3: Number of events in the subtracted spectrum, efficiencies and ratios n_{data}/ϵ for three different values of the cut on the variable E_{RMS} .

7.2.4 Summary on systematics

Looking at Tabs. 7.1-7.2 and at corresponding Figs. 7.4-7.6 it is apparent the different spectra behavior in the two regions below and above $m_{4\gamma} \simeq 400$ MeV. In the high mass range, a substantial stability is observed, with almost indistinguishable efficiency corrected spectra obtained with different cuts. In the low mass range, on the other hand, instability of the data/efficiency ratio under cuts variations is mainly connected to problems in background subtraction and to residual background contamination not properly described by the available MC simulations and the “data driven” background. For this reason, for each bin in the $200 \div 400$ MeV interval, variations $\delta_{\mathcal{L}}$, $\delta_{\chi\pi\pi}$ and $\delta_{E_{RMS}}$ obtained moving cuts from their central values have been regarded as strongly correlated, and no squared sums have been employed in order to evaluate the overall systematic errors; symmetric errors have been rather assumed choosing the maximum value among $\delta_{\chi\pi\pi}$ and $\delta_{E_{RMS}}$ for each bin. For the higher mass region all uncertainties have been combined, and for the bins in the $440 \div 560$ MeV interval a 6% uncertainty due to $K_S K_L$ normalization has been taken in account, too. Systematics treatment is summarized in Tab. 7.4, and systematic errors bars are plotted in the spectrum shown in Fig. 7.9.

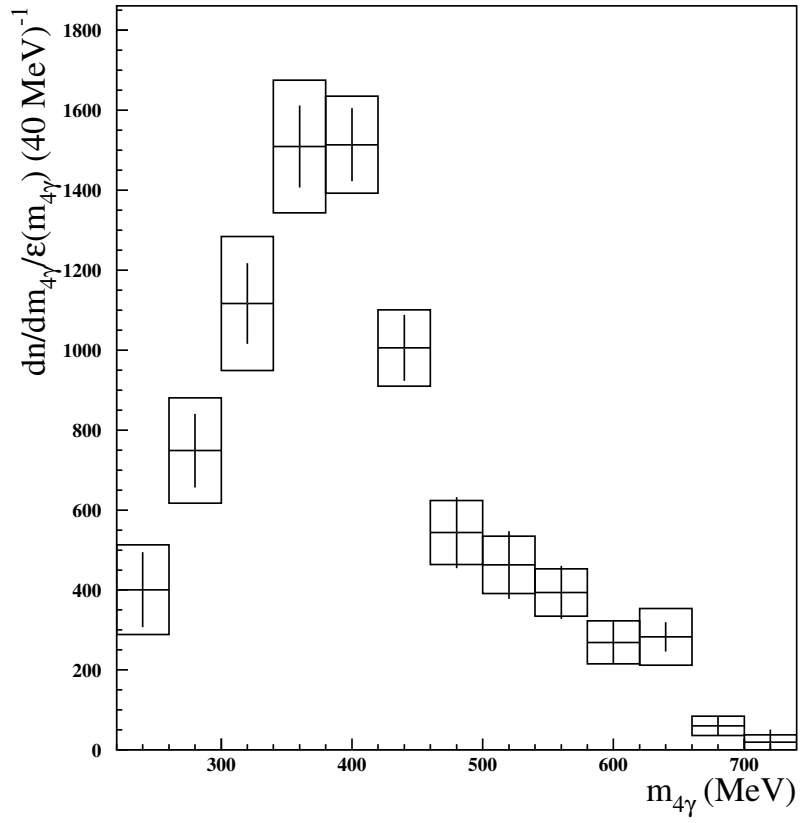


Figure 7.9: Efficiency-corrected subtracted spectrum with statistical error bars and systematic errors (boxes).

$m_{4\gamma}$ (MeV)	Criterion	$\delta n/n$ (%)
240	$\text{MAX}(\delta_{\mathcal{L}}, \delta_{\chi_{\pi\pi}^2}, \delta_{E_{RMS}})$	28
280	$\text{MAX}(\delta_{\mathcal{L}}, \delta_{\chi_{\pi\pi}^2}, \delta_{E_{RMS}})$	17.6
320	$\text{MAX}(\delta_{\mathcal{L}}, \delta_{\chi_{\pi\pi}^2}, \delta_{E_{RMS}})$	15
360	$\text{MAX}(\delta_{\mathcal{L}}, \delta_{\chi_{\pi\pi}^2}, \delta_{E_{RMS}})$	11
400	$\text{MAX}(\delta_{\mathcal{L}}, \delta_{\chi_{\pi\pi}^2}, \delta_{E_{RMS}})$	8
440	$\delta_{\mathcal{L}} \oplus \delta_{\chi_{\pi\pi}^2} \oplus \delta_{E_{RMS}} \oplus \delta_{K_S K_L}$	9.5
480	$\delta_{\mathcal{L}} \oplus \delta_{\chi_{\pi\pi}^2} \oplus \delta_{E_{RMS}} \oplus \delta_{K_S K_L}$	14.7
520	$\delta_{\mathcal{L}} \oplus \delta_{\chi_{\pi\pi}^2} \oplus \delta_{E_{RMS}} \oplus \delta_{K_S K_L}$	15.5
560	$\delta_{\mathcal{L}} \oplus \delta_{\chi_{\pi\pi}^2} \oplus \delta_{E_{RMS}} \oplus \delta_{K_S K_L}$	15
600	$\delta_{\mathcal{L}} \oplus \delta_{\chi_{\pi\pi}^2} \oplus \delta_{E_{RMS}}$	20
640	$\delta_{\mathcal{L}} \oplus \delta_{\chi_{\pi\pi}^2} \oplus \delta_{E_{RMS}}$	25
680	$\delta_{\mathcal{L}} \oplus \delta_{\chi_{\pi\pi}^2} \oplus \delta_{E_{RMS}}$	40
720	$\delta_{\mathcal{L}} \oplus \delta_{\chi_{\pi\pi}^2} \oplus \delta_{E_{RMS}}$	$\simeq 100$

Table 7.4: Summary table for systematics treatment. For each bin in the invariant mass spectrum the criterium followed to estimate the systematic error is indicated, end the error is quoted as relative uncertainty.

7.3 $\gamma\gamma \rightarrow \pi^0\pi^0$ cross section

Cross section as a function of $m_{4\gamma}$ is obtained dividing bin-per-bin the efficiency-corrected subtracted spectrum by the bin-per-bin integrated flux function. The Budnev *et al.* functional form of the flux function has been chosen, setting the dynamical cut-off at the value $q_{\gamma}^{max} = 140$ MeV (see §5.1.1). Result is shown in Fig. 7.10. A rising from threshold to $m_{4\gamma} \simeq 400$ MeV is seen, reaching the maximum value of $\simeq 45$ nb; the following fall is somehow blurred by huge fluctuations in the $550 \div 650$ MeV range. Note that these fluctuations, visible in the subtracted spectrum, too but much smaller there, are the result of the enhancement obtained when dividing by the flux function, which gets small values in this region.

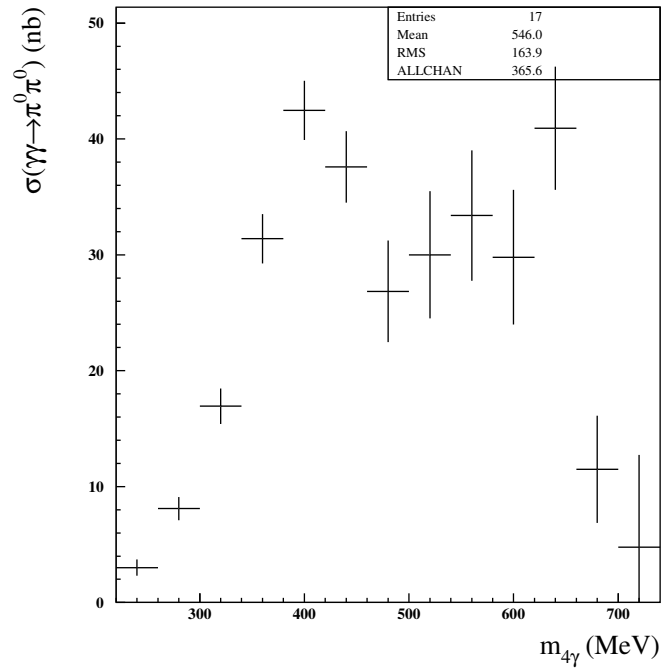


Figure 7.10: Cross section for $\gamma\gamma \rightarrow \pi^0\pi^0$ extracted from subtracted spectrum dividing it by efficiency and luminosity function. Budnev *et al* parameterization has been chosen for the luminosity function [11]. Only statistical errors are shown.

Conclusions

A study on $e^+e^- \rightarrow e^+e^-\pi^0\pi^0$ process analyzing $\sqrt{s} = 1$ GeV data collected by KLOE detector at DAΦNE has been presented. The goal of the analysis has been to study the excess of events in the low 4γ invariant mass spectrum already observed at a preliminary stage, excess which cannot be explained in terms of known annihilation processes and that is a candidate to be a $\gamma\gamma \rightarrow \pi^0\pi^0$ sample.

The analysis is challenging as one is looking for somehow unknown events for which no really reliable Monte Carlo exists. A simulation for a resonant production of a σ -like scalar meson has been used, based on last updated amplitudes calculation techniques, but the problem is that we do not even know if this $\gamma\gamma \rightarrow \sigma \rightarrow \pi^0\pi^0$ process occurs alone or associated with continuum -non resonant- production, or if it does not occur at all. For this reason, Monte Carlo simulation has been used mainly to evaluate analysis cuts efficiencies parametrized as functions of the 4γ invariant mass, and not to fit data. The followed strategy has rather been used to obtain a subtracted spectrum as much clean as possible, trying not to introduce a bias due to the signal modeling.

A cut-based analysis has been performed which manages to strongly reduce annihilation processes which represent background for the signal. The spectrum obtained by subtracting the known processes still presents a huge contamination from events that show features as high 4γ transverse momentum or unbalanced 4γ longitudinal momentum distribution which exclude any possible interpretation of these events as signal; in particular, asymmetry in the 4 photons p_L spectrum is a hint for beam gas background. Whatever this contamination is, it has been handled by performing a multivariate analysis in which the unknown background, selected from data by topological criteria, has been employed as a “data driven” simulation; the multivariate analysis returned consistent results, providing a reasonable invariant mass spectrum.

Known annihilation processes subtraction is performed with a rather good precision and works fine, as for example the $e^+e^- \rightarrow \omega\pi^0$ contribution shows in reproducing the high 4γ invariant mass spectrum region (see Fig. 6.30, shown again at the end of this chapter). Reliability on $e^+e^- \rightarrow \eta\gamma$ contribution simulation is ensured by

solid preliminary data-Monte Carlo checks and by the fact that the same data and Monte Carlo samples have been successfully employed in the $e^+e^- \rightarrow e^+e^-\eta$ analysis recently published by the KLOE Collaboration [19]. Minor processes as $e^+e^- \rightarrow f_0\gamma$, $e^+e^- \rightarrow a_0\gamma$ are handled with less accuracy as cross sections are known with great uncertainties, but their contribution is anyway negligible. The only important background process whose subtraction is source of a non negligible systematic error is $e^+e^- \rightarrow K_S K_L$, mainly due to wrong efficiency evaluation, for which a correction has been taken into account.

The obtained subtracted spectrum, corrected by Monte Carlo-evaluated efficiency, shows a rather good stability under cut values variation in the high mass range, while some instability just above production threshold is a hint for residual background contamination. Some minor problems are observed around $m_{4\gamma} \simeq 600$ MeV, too, where checks have to be done about possible contributions from other processes (e.g. $e^+e^- \rightarrow \rho\gamma$, $\rho \rightarrow \pi^0\pi^0\gamma$, for which high cross section values could compensate the small branching ratio). In any case, it is the signal region just above threshold that still needs some efforts in order to have a cleaner and stronger picture. The main task to be faced is the identification of the background rejected thanks to the multivariate analysis, which can arise from an admixture of

- beam gas background (electro-production of π^0 from residual gas in the beam pipe);
- $e^+e^- \rightarrow K_S K_L$ processes with $K_L \rightarrow \pi^0\pi^0\pi^0$ decaying almost promptly;
- high photon multiplicities processes (to explain the high 4γ p_T values, which arise if and only if the 4 photons are unbalanced) even from high mass scalar or tensor resonances produced in $\gamma\gamma$ interactions.

With respect to the last point, it is worth noting that convolution with the $\gamma\gamma$ luminosity function pushes the low invariant mass tail towards threshold even for resonance produced far away, and a deeper insight in $f_0(980)$, $a_0(980)$ and $f_2(1270)$ production by the photon-photon mechanism is mandatory.

Finally, a first attempt to extract the $\gamma\gamma \rightarrow \pi^0\pi^0$ cross section has been made. The result is not clear at all, as the shape is blurred by huge fluctuations in the $550 \div 650$ MeV range (visible in the subtracted spectrum, too, but greatly enhanced when dividing by the luminosity function). In any case, a structure is visible rising from threshold up to $\simeq 45$ nb at $m_{4\gamma} \simeq 400$ MeV, and then falling down. This is a completely different scenario with respect to result quoted by Crystal Ball experiment [15], which observed a quite flat cross section of $\simeq 10$ nb in the whole $200 \div 600$ invariant mass range.

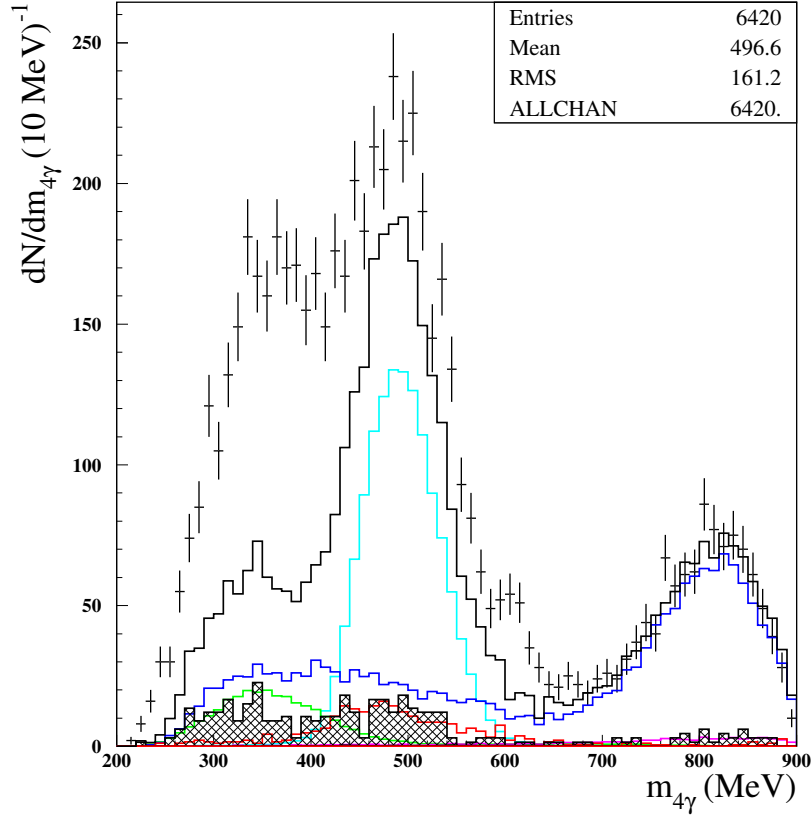


Figure 7.11: Spectra in $m_{4\gamma}$ after $\mathcal{L} > 0.5$ cut for data (points with error bars), background (black texture) and all signals but $\gamma\gamma \rightarrow \pi^0\pi^0$ process, using normalizations in Tab. 6.12 Color code: light blue = $K_S K_L$, green = $\eta\gamma$, dark blue = $\omega\pi^0$, violet = $f_0\gamma$. Black solid line is the sum of contributions.

Bibliography

- [1] Bechtel F. *et al.* *Nucl. Instrum. Meth. A*, (564):243, (2006).
- [2] Bogacz *et al.* Sapphire: a small gamma-gamma higgs factory. *arXiv:1208.2827*, 2012.
- [3] H. Grayer *et al.* High statistics study of the reaction $\pi^- p \rightarrow \pi^- \pi^+ n$: Apparatus, Method of Analysis, and General Features of Results at 17 GeV/c. *Nucl. Phys.*, B75(189), 1974.
- [4] E. M. Aitala *et al.* Experimental evidence for a light and broad scalar resonance in $D^+ \rightarrow \pi^+ \pi^+ \pi^-$ decay. *Physical Review Letters*, 86(770), 2001.
- [5] M. Aiblikim *et al.* The σ pole in $J/\psi \rightarrow \omega \pi^+ \pi^-$. *Physics Letters B*, 598(149), 2004.
- [6] H. Muramatsu *et al.* Dalitz analysis of $D_s^0 \rightarrow K_s^0 \pi^+ \pi^-$. *Physical Review Letters*, 89(251802), 2002.
- [7] C. Berger and W. Wagner. Photon photon reactions. *Physics Report*, 146, 1987.
- [8] Martin F. Bonneau G., Gourdin M. Inelastic lepton (anti-) lepton scattering and the two-photon axchange approximation. *Nuclear Physics B*, (54):573, 1973.
- [9] F. Low. Proposal for measuring the π^0 lifetime by π^- production in electron-electron or electron-positron collisions. *Phys. Rev.*, 120(582), 1960.
- [10] S. J. Brodsky, T. Kinoshita, and H. Terazawa. Two-photon mechanism of particle production by high-energy colliding beams. *Phys. Rev. D*, 4(1532), 1971.
- [11] V.M. Budnev, I.F. Ginzburg, G.V. Meledin, and V.G. Serbo. The two photon particle production mechanism. physical problems. applications. equivalent photon approximation. *Physics Reports*, 15(4):181–282, 1975.

- [12] M. Blatt and V. Weisskopf. *Theoretical Nuclear Physics*. 1952.
- [13] Pilkuhn H. *Properties and production spectra of elementary particles*. Landolt and Börnstein, 1972.
- [14] T. Oest et al. Measurement of resonance production in the reactions $\gamma\gamma \rightarrow \pi^0\pi^0$ and $\gamma\gamma \rightarrow \pi^0\eta$. *Z. Phys. C - Particles and Fields*, 47(343-351), 1990.
- [15] H. Marsiske et al. Measurement of $\pi^0\pi^0$ production in two photon collisions. *Phys. Rev.*, D41(3324), 1990.
- [16] S. Uheara et al. High-statistics measurement of neutral-pion pair production in two-photon collision. *Phys. Rev.*, D78(052004), 2008.
- [17] D. Capriotti. Ricerca di risonanze mesoniche prodotte in interazioni gamma gamma con l'esperimento KLOE. Master's thesis, Università degli Studi Roma Tre, 2008.
- [18] F. Nguyen, F. Piccinini, and A.D. Polosa. $e^+e^- \rightarrow e^+e^-\pi^0\pi^0$ at DAΦNE. *Eur. Phys. J.*, C47(65), 2006.
- [19] Babusci D. *et al.* Measurement of η meson production in $\gamma\gamma$ interactions and $\gamma(\eta \rightarrow \gamma\gamma)$ with the kloe detector. *JHEP*, (1301):119, 2013.
- [20] M.N. et al Achasov. Study of $e^+e^- \rightarrow \omega\pi^0 \rightarrow \pi^0\pi^0\gamma$ in the energy range 1.05-2.00 gev with the snd detector. *Phys. Rev. D*, 88(054013), 2013.
- [21] Ambrosino *et al.* Study of the process $e^+e^- \rightarrow \omega\pi^0$ in the ϕ -meson mass region with the kloe detector. *Phys.Lett. B*, 669:223, 2008.
- [22] N.N. Achasov and G.N. Shestakov. Phenomenological σ models. *Phys. Rev. D*, 49(11), 1994.
- [23] D. Capriotti. Study of the properties of scalar mesons with the KLOE experiment. *Nuovo Cimento*, C31(415), 2008.
- [24] F. Ceradini, F. Nguyen, and C. Taccini. Search for η meson production in $\gamma\gamma$ interactions with e^+e^- colliding beams at $\sqrt{s} = 1$ GeV. *KLOE memo*, (n.360), 21.9.2009.
- [25] J. D. Jackson. Remarks on the phenomenological analysis of resonances. *Nuovo Cimento*, 34(6), 1964.

- [26] N.N. Achasov. Light scalars in field theory. *arXiv:0810.2601v1*, 2008.
- [27] H. Czyz et al. Narrow resonances studies with the radiative return method. *arXiv:1002.0279v2*, 2010.
- [28] Particle Data Group. Review of particle physics. *Physics Letters B*, 667(1-5), 2008.
- [29] G. Rodrigo, H. Czyz, J. H. Kuhn, and M. Szopa. Radiative return at NLO and the measurement of the hadronic cross-section in electron positron annihilation. *Eur. Phys. J.*, C24(71), 2002.
- [30] G. Colangelo, M. Greco, and S. Dubnicska. Radiative corrections at DAΦNE. Technical report, LNF, 1992.
- [31] M. Gell-Mann and M. Levy. The Axial Vector Current in Beta Decay. *Il Nuovo Cimento*, 16(4), 1960.
- [32] C. Itzykson and J. B. Zuber. *Quantum Field Theory*. Dover Publications, 2006.
- [33] S. Pokorski. *Gauge Field Theory*. Cambridge University Press, 2000.
- [34] R. Brun et al. Geant3. Technical report, CERN, 1984.
- [35] R. Brun et al. Geant: Simulation for particle physics experiments. User guide and reference manual. Technical report, CERN, 1978.